
Magnetokristalline Anisotropie von Eisen-Dünnschichten mit interstitiellem Stickstoff und Bor

Magnetocrystalline anisotropy of iron thin films with interstitial nitrogen and boron
Zur Erlangung des akademischen Grades Doktor-Ingenieur (Dr.-Ing.)
genehmigte Dissertation von M.Sc. Dominik Gölden aus Viersen
Tag der Einreichung: 17.10.2017, Tag der Prüfung: 24.01.2018
Darmstadt 2018 — D 17

1. Gutachten: Prof. Dr. Lambert Alff
2. Gutachten: Prof. Dr. Oliver Gutfleisch



TECHNISCHE
UNIVERSITÄT
DARMSTADT

Fachbereich Material- und Geowis-
senschaften
Fachgebiet Dünne Schichten

Magnetokristalline Anisotropie von Eisen-Dünnschichten mit interstitiellem Stickstoff und Bor
Magnetocrystalline anisotropy of iron thin films with interstitial nitrogen and boron

Genehmigte Dissertation von M.Sc. Dominik Gölden aus Viersen

1. Gutachten: Prof. Dr. Lambert Alff
2. Gutachten: Prof. Dr. Oliver Gutfleisch
1. Prüfer: Jun. Prof. Dr. Hongbin Zhang
2. Prüfer: Prof. Dr. Barbara Albert

Tag der Einreichung: 17.10.2017

Tag der Prüfung: 24.01.2018

Darmstadt — D 17

Bitte zitieren Sie dieses Dokument als:

URN: urn:nbn:de:tuda-tuprints-72531

URL: <http://tuprints.ulb.tu-darmstadt.de/7253>

Dieses Dokument wird bereitgestellt von tuprints,

E-Publishing-Service der TU Darmstadt

<http://tuprints.ulb.tu-darmstadt.de>

tuprints@ulb.tu-darmstadt.de



Die Veröffentlichung steht unter folgender Creative Commons Lizenz:

Namensnennung – Nicht kommerziell – Keine Bearbeitungen 4.0 International (CC BY-NC-ND 4.0)

<http://creativecommons.org/licenses/by-nc-nd/4.0/deed.de>

Erklärung zur Dissertation

Hiermit versichere ich, die vorliegende Dissertation ohne Hilfe Dritter nur mit den angegebenen Quellen und Hilfsmitteln angefertigt zu haben. Alle Stellen, die aus Quellen entnommen wurden, sind als solche kenntlich gemacht. Diese Arbeit hat in gleicher oder ähnlicher Form noch keiner Prüfungsbehörde vorgelegen.

Darmstadt, den 17.10.2017

(M.Sc. Dominik Gölden)



Abstract

The permanent magnet candidate α' -Fe₈N is a metastable bct phase that has an enhanced magnetocrystalline anisotropy compared to its parent bcc phase α -Fe and a much discussed potential giant magnetic moment. In the first part of this work, the frame conditions to obtain α' -Fe₈N are established for thin films grown by molecular beam epitaxy (MBE). It is found that temperatures of approximately 373 K, in combination with MgO (100) or MgAl₂O₄ (100) substrates, are required to form the phase of interest. Either ϵ -Fe_xN or γ' -Fe₄N, depending on the substrate utilized, form at higher nitrogen concentrations. For higher temperatures of 473 and 623 K, the thermodynamic γ' -phase becomes more pronounced and occupies a broader stability window in terms of temperature and nitrogen content compared to equilibrium conditions. From these results, a low temperature thin film phase diagram is established.

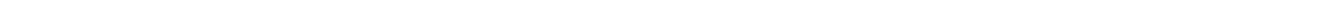
The optimization of growth parameters for MBE and sputter grown α' -Fe₈N films and the subsequent determination of their magnetic properties as a function of the degree of tetragonalization is used in order to clarify the results found in the literature. While no evidence of a giant magnetic moment beyond $2.5 \mu_B$ per iron atom could be found, the magnetocrystalline anisotropy was increased up to $1.18 \times 10^5 \text{ J/m}^3$ ($1.18 \times 10^6 \text{ erg/cm}^3$) for MBE grown and $2.05 \times 10^5 \text{ J/m}^3$ ($2.05 \times 10^6 \text{ erg/cm}^3$) for sputtered films as a function of the tetragonal distortion while the magnetic easy axis aligns parallel to the c -axis. The Curie temperature was extrapolated from M vs. T plots and is reduced to $(770 \pm 73) \text{ K}$ compared to an α -Fe sample with $T_C = (1056 \pm 85) \text{ K}$. By annealing samples in vacuum at 353 and 423 K, the decomposition temperature of the α' -phase was investigated, revealing that the onset of decomposition lies significantly lower than the previously established 453 K. An attempt to increase the decomposition temperature by introducing Co into the phase was performed for $(\text{Fe}_{100-x}\text{Co}_x)_8\text{N}$ with $x = 6.4, 8.5, 12.7, 14.8, \text{ and } 20$. However, Co is found to inhibit the incorporation of nitrogen, leading to inhomogeneous samples with a wide distribution of c -axis lattice constants most likely due to a mixture of FeCo and Fe-N phases.

Furthermore, boron instead of nitrogen interstitials are introduced into the α -Fe lattice as a potential method to increase the decomposition temperature. A deposition temperature of 573 K is required in order to obtain crystalline samples for the maximum boron content of 13 at.% in the films, determined by X-ray photoelectron spectroscopy. Qualitatively identical to the evolution observed for α' -Fe₈N, the c -axis lattice constants of the Fe-B samples increase as a function of boron content while the a -axis lattice constants shrink. Compared to the Fe-N case with a c/a ratio of 1.11, the maximum c/a observed for the Fe-B samples is 1.05. In addition, the magnetic easy axis remains in-plane while the absolute value of magnetic anisotropy increases to $-5.1 \times 10^5 \text{ J/m}^3$ ($-5.1 \times 10^6 \text{ erg/cm}^3$). Density functional theory confirms these results and shows that the local boron ordering is found to be the reason for the easy-plane configuration.

Die metastabile bct Phase α' -Fe₈N ist durch die im Vergleich zu der bcc Ursprungsphase α -Fe erhöhten magnetokristallinen Anisotropie, ebenso wie einem vieldiskutierten magnetischen Moment jenseits der $3.0\mu_B$, ein möglicher Kandidat als seltenerdfreier Permanentmagnet. Im ersten Abschnitt dieser Arbeit werden die nötigen Parameter für das Wachstum von α' -Fe₈N durch Molekularstrahlepitaxie (MBE) eingegrenzt. Es zeigt sich, dass Temperaturen von etwa 373 K, in Kombination mit MgO (100) oder MgAl₂O₄ (100) Substraten, das Wachstum der Phase begünstigen. In Abhängigkeit des genutzten Substrates bilden sich bei höheren Stickstoffkonzentrationen entweder ϵ -Fe_xN oder γ' -Fe₄N. Im Kontrast zu Gleichgewichtsbedingungen bildet sich die γ' Phase bei Temperaturen von 473 and 623 K in einem wesentlich breiteren Stöchiometriefenster aus. Zusammenfassend wird ein aus den genannten Ergebnissen erstelltes Dünnschicht-Phasendiagramm vorgestellt.

Die Optimierung der Wachstumsparameter für MBE und gesputterte α' -Fe₈N Schichten, inklusive der gefundenen magnetischen Eigenschaften als Funktion der Tetragonalisierung werden anschließend genutzt, um verschiedene abweichende Ergebnisse aus der Literatur zu erhellen. Obwohl kein Beweis für ein magnetisches Moment oberhalb von $2.5\mu_B$ pro Eisenatom gefunden werden konnte, wurde die magnetokristalline Anisotropie auf bis zu $1.18 \times 10^5 \text{ J/m}^3$ ($1.18 \times 10^6 \text{ erg/cm}^3$) für durch MBE gewachsene und $2.05 \times 10^5 \text{ J/m}^3$ ($2.05 \times 10^6 \text{ erg/cm}^3$) für gesputterte Schichten als Funktion der tetragonalen Verzerrung erhöht, während die magnetische Vorzugsrichtung sich parallel zur c -Achse ausgerichtet hat. Die Curie Temperatur wurde mit Hilfe von M vs. T Messungen auf $(770 \pm 73) \text{ K}$ extrapoliert, ein Wert der geringer ausfällt als das T_C von α -Fe mit $(1056 \pm 85) \text{ K}$. Des Weiteren wurde die Zerfallstemperatur von α' -Fe₈N durch Tempern im Vakuum bei 353 und 423 K untersucht. Hierbei zeigte sich, dass der Zerfall bereits bei wesentlich geringeren Temperaturen einsetzt als die bisher in der Literatur etablierten 453 K. Ein Versuch, den Zerfall durch den Einbau von Co in das Gitter zu verzögern wurde für $(\text{Fe}_{100-x}\text{Co}_x)_8\text{N}$ mit $x = 6.4, 8.5, 12.7, 14.8$ und 20 durchgeführt. Dies verringerte allerdings die Menge des gelösten Stickstoffes, wodurch inhomogene Schichten mit einer breiten Verteilung von c -Achsen-Gitterkonstanten entstanden. Ein möglicher Grund für dieses Verhalten ist das parallele Wachstum von FeCo und Fe-N Phasen.

Der Ansatz, die Zerfallstemperatur durch interstitielles Bor anstelle von Stickstoff zu erhöhen, wird abschließend behandelt. Es wurden Wachstumstemperaturen von 573 K benötigt, um kristalline Proben mit einem maximalen Boranteil von 13 at.%, gemessen durch Röntgenphotoelektronenspektroskopie, herzustellen. Das qualitative Verhalten ist hierbei identisch zu α' -Fe₈N, da eine Ausdehnung entlang der c -Achse ebenso wie eine Verkleinerung der a -Achsen-Gitterkonstante als Funktion des Boranteils beobachtet wurde. Es zeigt sich aber, dass das c/a Verhältnis der Fe-N Phase mit 1.11 stärker ausgeprägt ist, als das der Fe-B Phase mit 1.05. Zusätzlich dazu verbleibt die magnetische Vorzugsrichtung in der Ebene während der Betrag der magnetischen Anisotropie auf $-5.1 \times 10^5 \text{ J/m}^3$ ($-5.1 \times 10^6 \text{ erg/cm}^3$) steigt. Mit Hilfe von Dichtefunktionaltheorie werden diese Ergebnisse bestätigt und es zeigt sich, dass die lokale Anordnung des Bors der Grund für die Vorzugsrichtung in der Ebene ist.



Contents

1	Introduction	1
2	Experimental	4
2.1	Thin film growth	4
2.2	Molecular beam epitaxy	7
2.2.1	Reflection high-energy electron diffraction	10
2.2.2	Radiofrequency radical source	11
2.3	Sputtering	13
2.4	X-ray analysis techniques	16
2.5	SQUID magnetometry	20
3	Magnetism	22
3.1	Diamagnetism	22
3.2	Ferromagnetism	25
3.2.1	Weiss theory of ferromagnetism	25
3.2.2	Stoner model of ferromagnetism	26
3.3	Magnetic anisotropy	28
3.3.1	Magnetocrystalline anisotropy	28
3.3.2	Shape, surface, and strain anisotropies	31
4	Literature review on α'' -Fe ₁₆ N ₂	33
4.1	Origin of the giant magnetic moment in α'' -Fe ₁₆ N ₂	35
4.2	MAE and PMA in α'' -Fe ₁₆ N ₂	39
4.3	Thermal stability of α'' -Fe ₁₆ N ₂	40
5	Experimental investigation of the iron nitride phase diagram	43
5.1	Growth temperatures below 473 K	43
5.2	Growth temperatures of and above 473 K	46
5.3	Low temperature MBE phase diagram	49
6	Growth and characterization of α' -Fe ₈ N	50
6.1	α' -Fe ₈ N formation and properties grown by MBE	50
6.2	α' -Fe ₈ N growth via sputtering	56
6.3	Thickness study of α' -Fe ₈ N on MgO, MAO, and STO	60
6.4	Annealing of α' -Fe ₈ N	63
6.5	Substitution of Fe by Co in α' -Fe ₈ N	66
6.6	α' -Fe ₈ N as a potential permanent magnet candidate	69
7	Growth and characterization of interstitial Fe-B	70
7.1	Temperature dependence of B solubility	70
7.2	Structural and magnetic properties of interstitial Fe-B	71
7.3	DFT calculations on anisotropy in Fe-B	77
7.4	Viability of interstitial Fe-B	78
8	Conclusion	79
9	Outlook	81

10 Publications	83
References	87
Acknowledgements	101
Curriculum vitae	102
Appendix	103
A BN low-flow aperture and discharge tube designs	103
B Formation of (002) and (011) oriented α -Fe	105
C MBE and sputtering processes	107

1 Introduction

Permanent magnets are irreplaceable in many modern technologies. They can be found in smartphones, electric and hybrid cars, gearless wind turbines, and many more applications. At the present time, two main groups of permanent magnets exist and are used depending on the necessary performance in their application. The first group are the ferrite based permanent magnets. They are cheap and make up the majority of the yearly volume of the world permanent magnet production. One drawback of the ferrites is their comparably small energy product which makes them unsuitable for applications which require a high performance.

For these particular cases the rare-earth based magnets, most prominent amongst them the $\text{Nd}_2\text{Fe}_{14}\text{B}$ compound, are employed. They exhibit an extraordinary energy product above 240 kJ/m^3 (30 MGOe), allowing for a high efficiency of e.g. generators or motors in which they are used [1]. Unfortunately, these compounds have one technological and one political drawback. To begin with, if the operating temperature in a given application surmounts approximately 353 K, the $\text{Nd}_2\text{Fe}_{14}\text{B}$ phase has a significantly reduced performance due to its relatively low Curie temperature [2]. This can be resolved by alloying it with heavy rare-earth elements like dysprosium or terbium to increase the Curie temperature. Unfortunately, due to the antiferromagnetic coupling of these heavy rare-earths to the iron sublattice, the alloying leads to a reduction of the remanent magnetization and the energy product, which therefore lowers the performance of the magnet while at the same time increasing its cost [3].

In addition, the world mining yield of rare-earth containing ores has been dominated by China for approximately 20 years, with a maximum contribution of around 97% in the years 2006–2010, as shown in Fig. 1. This virtually monopolistic situation led to the so-called rare-earth crisis in the year 2010/11. During this time, China reduced the export quotas for rare-earth elements by approximately 11% which led to an escalation of the prices for all rare-earths shown in figure 2, with peak prices that were 650%, 1800%, and 450% higher than the pre-crisis price for dysprosium, and terbium, respectively. Although the export restrictions have been removed and the prices have almost returned down to their level before the crisis, the supply situation is mostly unchanged. At the same time, the demand for high performance magnets is steadily rising due to, for example, the increasing numbers of electric cars and wind turbines. Specifically in the case of the heavy rare-earths, the extrapolated future demand will exceed the available production capacities [4].

To alleviate these problems, three main technological approaches are presently being pursued. Firstly,

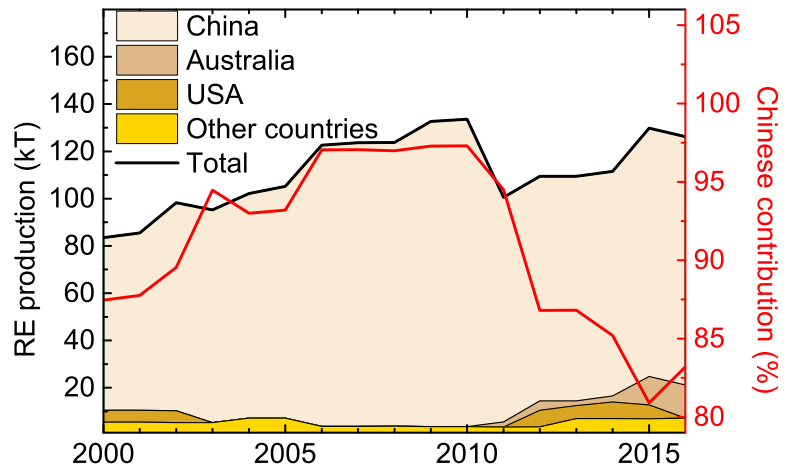


Figure 1: World rare-earth (RE) production in kT per country (left axis) and Chinese contribution to the rare-earth production (right axis). Data adapted from [4].

reducing the usage of expensive heavy rare-earth elements in $\text{Nd}_2\text{Fe}_{14}\text{B}$ for high temperature applications leads to reduced costs while simultaneously improving the energy product of the magnet. This can be achieved by the means of new, so-called grain boundary diffusion processes through which the heavy rare-earth containing $(\text{Nd,Dy})_2\text{Fe}_{14}\text{B}$ or $(\text{Nd,Tb})_2\text{Fe}_{14}\text{B}$ coats pure $\text{Nd}_2\text{Fe}_{14}\text{B}$ grains [5–8].

Secondly, rare-earth balance magnets are developed in order to make more efficient use of the so-called rare-earth basket. This term describes the fact that no rare-earth can be mined exclusively, resulting in a stockpiling of the more abundant and less used, therefore cheap, rare-earth elements like cerium and lanthanum. Amongst others, two exemplary approaches to rare-earth balance magnets are $(\text{CeNd})\text{FeB}$ [9] as well as lanthanum based magnets like La_2Co_7 [10] are under investigation.

Finally, research for rare-earth free permanent magnets is being conducted and can also be divided into various different approaches. One option is to take an already existing (super-)hard magnet with high anisotropy and improve its energy product by increasing the remanent magnetization of the magnet. This can be achieved by the combination of a high saturation magnetization but low anisotropy magnetic anisotropy material like $\text{Fe}_{65}\text{Co}_{35}$ with, for example, MnBi in order to create a spring-exchange magnet which combines the hard magnetic properties of MnBi with the high saturation of $\text{Fe}_{65}\text{Co}_{35}$ [11, 12].

Another path is the magnetic hardening of a high saturation magnetization but low magnetic anisotropy material like α -iron by the means of structural distortion. By theory as well as thin film experiment, highly distorted FeCo has been shown to exhibit a vast increase in its magnetic anisotropy up to approximately $1 \times 10^7 \text{ J/m}^3$ ($1 \times 10^8 \text{ erg/cm}^3$) [13, 14]. Since these properties were obtained by the means of a tailored epitaxial strain on the FeCo that, in this magnitude, can only be stabilized for a few atomic layers, an alternative has to be found in order to achieve these properties in bulk samples. The well known iron nitride $\alpha''\text{-Fe}_{16}\text{N}_2$ is an example for this approach. Here, the nitrogen atoms diffuse into interstitial positions on the bcc iron lattice which causes a tetragonal distortion, resulting in an increased magnetic anisotropy. This distortion could also be achieved for powder and bulk samples, therefore making this phase a potential permanent magnet candidate [15].

This thesis is divided into three principal parts to address this topic. The first part serves as a general introduction to the work and features a short survey of the most commonly used experimental techniques as well as an introduction into magnetism in chapter 2 and 3, respectively. Additionally, a review of the current state of research on $\alpha''\text{-Fe}_{16}\text{N}_2$ and $\alpha'\text{-Fe}_8\text{N}$ is given in chapter 4 in order to elucidate the many, sometimes conflicting, reports on the magnetic and structural properties. The second part deals

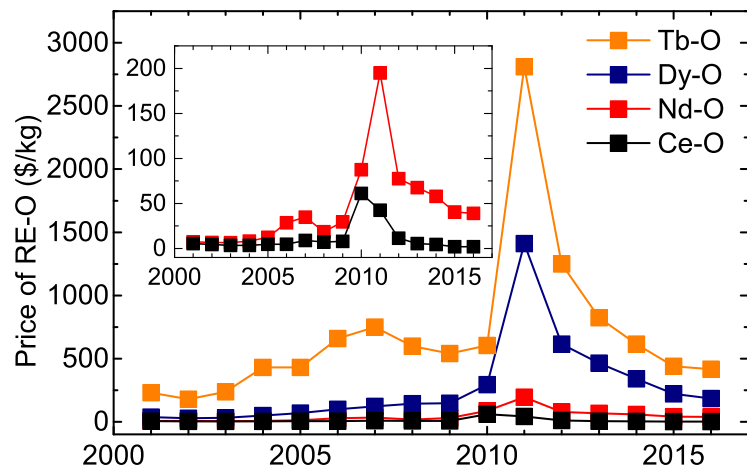


Figure 2: Year-end prices for the oxides of Ce, Nd, Dy, and Tb. The inset displays the price evolution for the oxides of Nd and Ce. Data adapted from [4].

with the experimental results obtained for iron nitride samples and is divided in two chapters. Chapter 5 contains studies on different growth temperatures, substrates, and growth rates in order to establish a low temperature thin film phase diagram as a foundation for further work on the iron nitride system in general and α' -Fe₈N in particular. It serves as a framework for chapter 6, where a detailed optimization of the growth conditions for α' -Fe₈N is performed and the resulting magnetic anisotropy, magnetization, and Curie temperature in addition to investigations concerning the decomposition temperature are given. A first attempt to improve the decomposition temperature by substituting iron with cobalt to achieve (Fe_{100-x}Co_x)₈N is also discussed. In addition, the chapter is concluded by an evaluation of α' -Fe₈N as a potential permanent magnet. The third part, covered by chapter 7, presents a second approach to achieve an enhanced anisotropy and/or decomposition temperature by utilizing boron instead of nitrogen interstitials. Finally, this work is summarized and concluded in chapter 8 and an outlook is given in chapter 9.

While finding a replacement for Nd₂Fe₁₄B would be the ultimate goal for the performance of any new (rare-earth free) permanent magnet and therefore this work, the main interest lies in closing the gap between the low cost, low performance ferrites and the high cost, high performance rare-earth based magnets.

2 Experimental

This chapter gives an overview over the general background on thin film growth, see section 2.1, in addition to the experimental techniques used to synthesize and characterize the samples. In the scope of this work, the samples were grown either by molecular beam epitaxy (MBE) or radio frequency (rf) magnetron sputtering, briefly described in section 2.2 and 2.3, respectively, with the exception of the iron boride films that were grown exclusively by MBE. Section 2.4 represents a brief introduction into X-ray diffraction (XRD), the technique used in order to investigate the crystal structure and orientation, as well as X-ray reflectometry (XRR), utilized to extract the film thickness, roughness, and density. Superconducting quantum interference device (SQUID) magnetometry, treated in section 2.5, was used to measure the magnetic properties.

2.1 Thin film growth

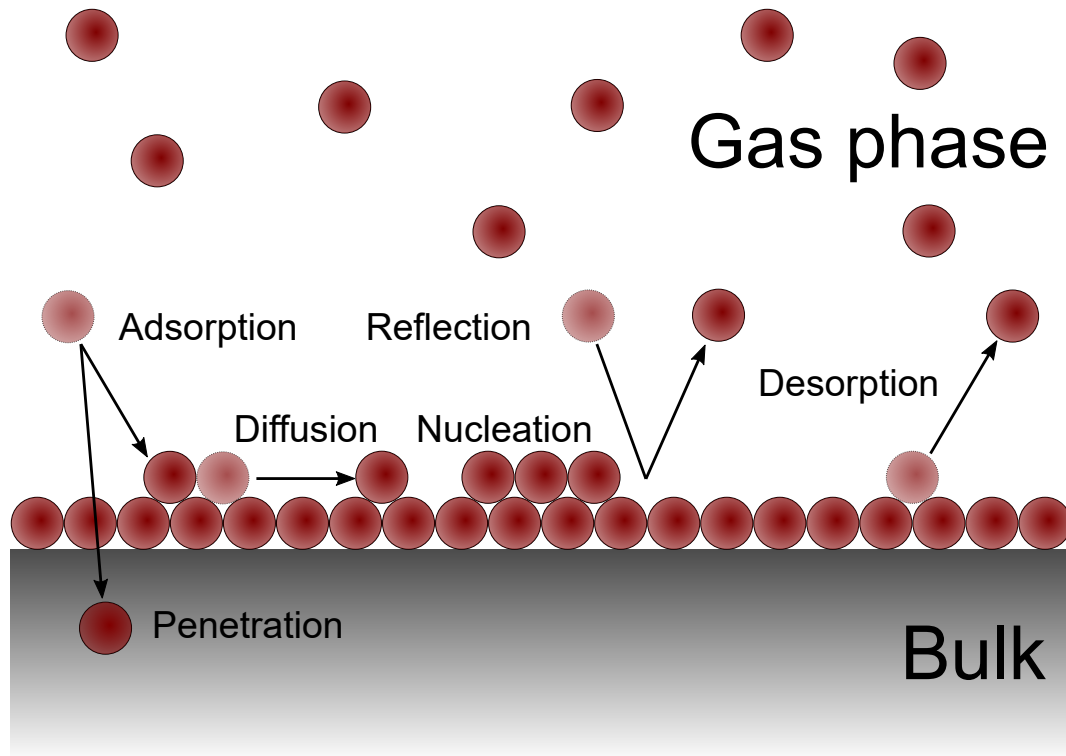


Figure 3: Processes occurring during the thin film growth from the gas phase.

For modern thin film devices like processors and sensors, a defined amount of atomic layers have to be deposited with atomic precision. By controlling the deposition rate of atoms from the gas phase as well as the kinetic and thermodynamic boundary conditions during the deposition, the non equilibrium process of thin film growth, schematically shown in figure 3, can be utilized to grow specific structures onto a (crystalline) substrate [16]. Thin film growth can be divided into five different steps: Physisorption, surface diffusion, chemisorption, nucleation, and continued growth. During the first stage, atoms can either penetrate the surface, be reflected by or adsorbed onto the surface as well as desorb from it. For the surfaces of single crystals, the process of adsorption is well described by the Langmuir isotherm. It

is assumed that the atoms in the gas A and the adsorption sites S on surface are in a constant exchange with the occupied sites AS as described by



With the surface coverage Θ as the fraction of the surface sites occupied by adsorbates, an equilibrium constant K

$$K = \frac{k_A}{k_D} = \frac{\Theta}{p(1-\Theta)}, \quad (2)$$

with k_A being the equilibrium adsorption rate, k_D the equilibrium desorption rate, and p the adsorbate gas pressure can be defined. The change of surface coverage for adsorption Θ_A and for desorption Θ_D can then be written as

$$\frac{d\Theta_A}{dt} = k_A p N_s (1 - \Theta_A), \quad \frac{d\Theta_D}{dt} = -k_D p N_s \Theta_D, \quad (3)$$

with N_s being the total number of sites on the surface. The first step of adsorption is called physisorption. Here, the adsorbed atom will be only weakly bonded to the surface by Van-der-Waals forces with a binding energy below 1 eV. Physisorbed atoms have a high diffusion length in the range of micrometers with a surface mobility that is described by the surface diffusion coefficient D with

$$D = a^2 \nu e^{-V_s/k_B T_s}, \quad (4)$$

where k_B is the Boltzmann constant, T_s is the substrate temperature, V_s is the potential energy barrier between adsorption sites, and a is the effective hopping distance between adsorption sites. The term $k_s = \nu e^{-V_s/k_B T_s}$ is the site-to-site hopping rate of an adsorbed atom. At a constant adsorption rate of atoms on an initially flat surface, D defines the distance of an adsorbed atom to an existing nucleation site or to another adsorbed atom with which another nucleation site could be formed. During the film growth, D decreases until it reaches a steady state. Generally, the density of nucleation sites, also called islands, decreases with increasing D and increases with increasing deposition rate. The two parameters that are used to tailor the growth of thin films are thus the surface diffusion that can be controlled via the substrate temperature T_s and the deposition rate [17].

As atoms bond together to form nucleation sites, chemisorption occurs, giving rise to a binding energy between 1 and 10 eV. Chemisorbed atoms have a vastly reduced diffusion length in the range of nanometres. For stable islands to be formed, the critical island size needs to be overcome. Below this size threshold, single adatoms are energetically more favourable than islands due to the surface energies of the involved interfaces. This relationship is summed up by the total Gibbs energy ΔG

$$\Delta G = A_1 \gamma_{iv} + A_2 (\gamma_{is} - \gamma_{sv}) + V \Delta G_v \quad (5)$$

with A_1 being the contact surface of island to vapour, A_2 the surface of island to substrate, γ_{iv} the surface energy between island and vapour, γ_{is} the surface energy between island and substrate, V the volume of

the island, and ΔG_v the relative Gibbs energy between the gas phase and the island [17]. Depending on the relative magnitudes of the γ_x , three different general growth modes can be distinguished. If

$$\gamma_{sv} > \gamma_{iv} + \gamma_{is} \quad (6)$$

applies, a smooth film that wets the surface of the substrate will form. This so called Frank-van der Merwe growth, see also figure 4(a), equals a two dimensional growth of consecutive (mono)layers. The case of

$$\gamma_{sv} < \gamma_{iv} + \gamma_{is} \quad (7)$$

is called Vollmer Weber or island growth, depicted in figure 4(b), that is characterized by a slow surface diffusion. Here the growing film reduces the interface area to the substrate by forming islands, leading to a three dimensional growth and subsequently to a rough film. During the third growth mode, called the Stranski-Krastanov growth, shown in Fig. 4(c), one initially observes the growth according to equation 6. After a few layers grown in a two dimensional mode, equation 7 applies and islands are formed on the first smooth layers. This mixed growth mode results from a misfit to the substrate, with relaxation of stresses occurring after a few layers [17].

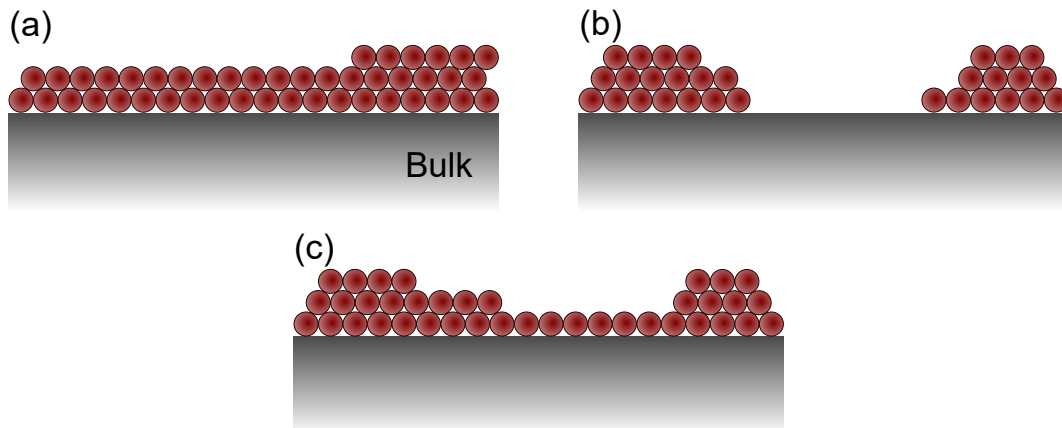


Figure 4: (a) Frank-van der Merwe growth, (b) Vollmer Weber growth, and (c) Stranski-Krastanov growth.

In addition to these three equilibrium growth modes that usually require growth temperatures above 473 K, non-equilibrium growth modes are of interest in order to grow thin films of metastable phases. When films are grown at either high growth temperatures or with a low deposition rate, adatoms are sufficiently mobile or have sufficient time to diffuse to the nearest step. This so called step-flow growth results in a high step density of the grown film, a feature that can be clearly distinguished with the help of reflection high energy electron diffraction (RHEED). For either low temperatures, high deposition rates, or low step densities, diffusion is limited and adatoms immediately nucleate. Given sufficient time, a smooth monolayer is formed upon which islands grow again, resulting in alternating high and low roughnesses of the film [17, 18].

2.2 Molecular beam epitaxy

Molecular beam epitaxy, or short MBE, is a physical vapour deposition (PVD) technique that was developed around 1968 at the Bell Telephone Laboratories by Arthur and Cho. Already around 1958, the basic idea was established by Günther for semiconductors [19,20]. It was shown that by MBE, one can grow atomically flat and ordered layers, a necessity for reproducible thin film device characteristics. During approximately five years after the first reports, MBE was quickly established as a powerful tool for semiconductor research and until today, its primary use is the growth of films for semiconductor devices [21]. Characteristically, the attainable deposition rate of MBE is low enough, from below one monolayer per second to several nanometres per second, to allow epitaxial growth. In combination with a vacuum in the range of approximately 10^{-6} to 10^{-10} Pa (10^{-8} to 10^{-12} mbar) due to which the atomic beam emitted by the source travels collision free to the substrate, high-quality films can be achieved. The achievable level of purity in the final films are strongly dependent on the vacuum of the system [22]. The number of gas atoms n that are adsorbed onto a surface of 1 cm^2 per second can be described by

$$\frac{dn}{dt} = \frac{p}{\sqrt{2\pi mk_B T}} \frac{1}{\text{cm}^2\text{s}} \quad (8)$$

with p being the gas pressure, m the atomic mass of the gas, k_B the Boltzmann constant, and T the temperature of the system. As an example, a partial oxygen pressure of 10^{-6} Pa at room temperature results in a deposition rate of $3 \times 10^{12} \text{ cm}^{-2}\text{s}^{-1}$. A solid surface equals roughly 10^{14} atoms per 1 cm^2 which means that even at 10^{-6} Pa one monolayer of oxygen would be formed within 34 s. As a direct consequence, a deposition rate of one monolayer per second of a specific material would have an oxygen impurity concentration of 3%. While this concentration is also depending on the reaction rate of the deposited material with the residual gases, it is clear that industrial level impurity rates of one part per million or less require pressures of or below 10^{-10} Pa.

Typical MBE setups are composed of several key components:

- Material evaporation source(s)
- Growth rate monitoring
- Source shutter(s)
- Substrate holder and heater
- Reflection high-energy electron diffraction (RHEED) setup
- Cooling shroud

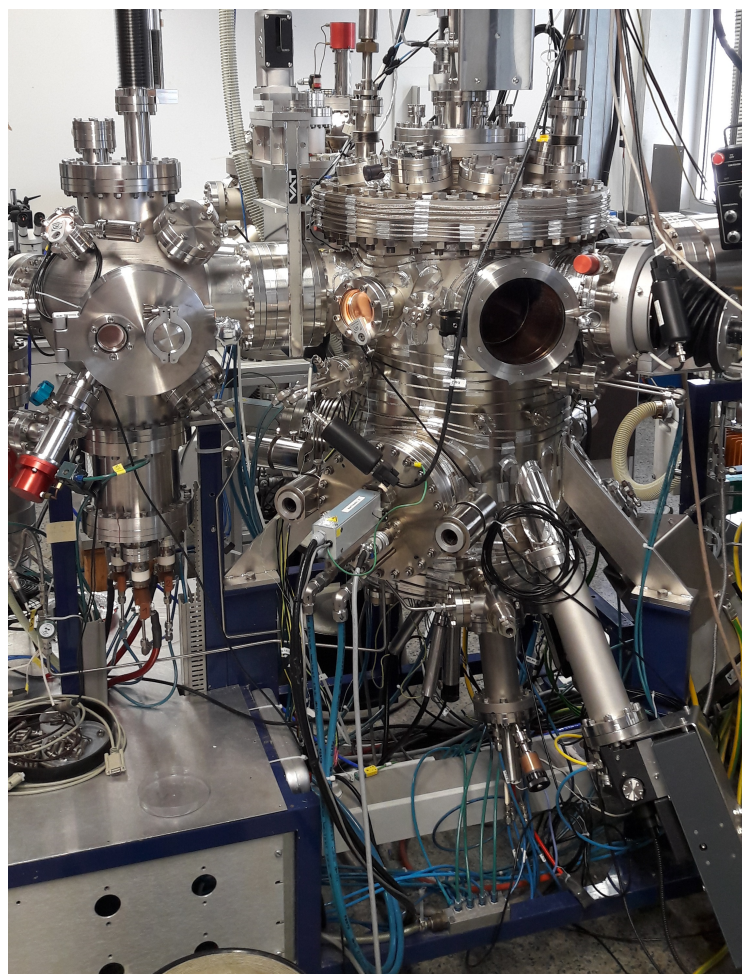
The key aspects to MBE are the low background pressure during deposition and the RHEED setup which will be discussed in section 2.2.1. Amongst others, the low pressure is achieved by a liquid nitrogen filled cooling shroud in the chamber. Its low wall temperature leads to an adsorption of residual gases, thus effectively acting as a cryogenic pump. In addition, the material flux from the sources that was not deposited on the substrate condenses on the cooling shroud, resulting in only a minor increase

of background pressure during source operation. Due to this low background pressure, RHEED can be used for in-situ growth monitoring of the films [22].

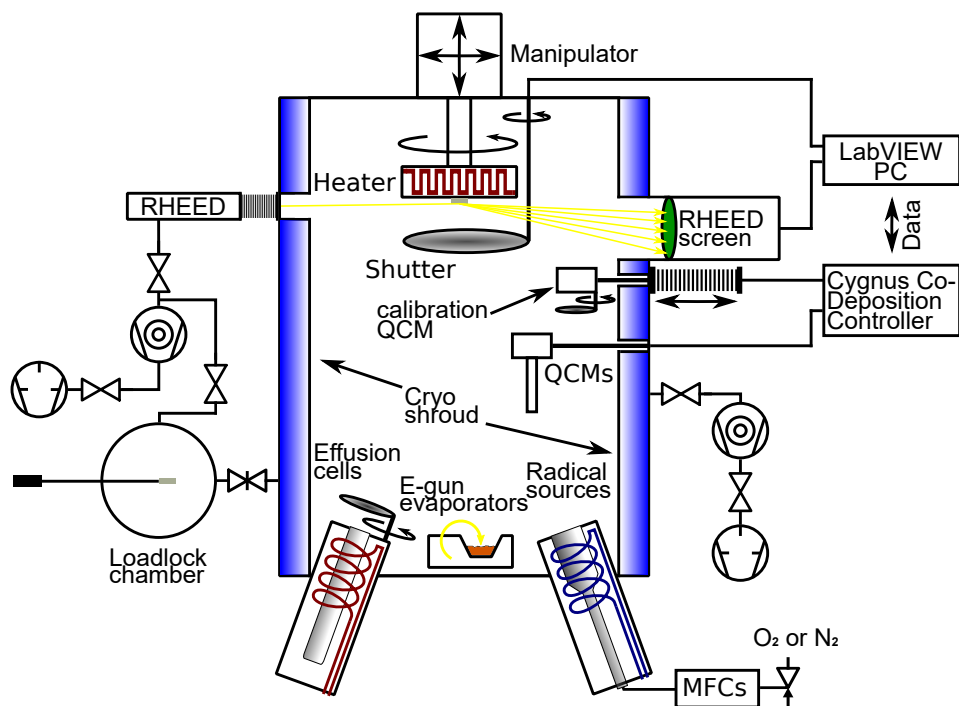
Another important point that has a strong influence on the thin films' properties is the temperature control, since many materials or material systems require a specific growth temperature in order to obtain a suitably good crystal quality and/or the desired phase. Unfortunately, it is technically difficult to achieve a good thermal contact between a (semiconductor) substrate and the heater. The first heaters used indium as a low temperature melting metal to form a liquid thermal contact. However, at temperatures above 873 K, the vapour pressure of indium becomes significant, resulting in contamination of the films. To solve this problem, radiative heaters were developed. Here, the substrate is mounted on a ring and irradiated from the back by a resistive element or an infrared laser, effectively avoiding contamination and allowing a fast change of temperature if necessary [22, 23].

Depending on the melting point as well as the desired deposition rate of the element, two techniques are most commonly used to achieve a controlled evaporation of specific elements. Effusion cells are used for most elements that have a comparably low melting point up to operating temperatures of around 1673 K at which the cell materials' vapour pressure is sufficiently low for the required purity of the sample. The evaporation takes place by heating the source material in a crucible of, for example, pyrolytic boron nitride. This leads to a beam of atoms that are thermally ejected towards the substrate, resulting in an extremely stable evaporation rate. It can be controlled by varying the temperature down to steps of 0.1 K, is monitored by a thermocouple close to the crucible bottom. However, even special high temperature effusion cells are limited to maximum operating temperatures of around 2273 K. For materials that have a high melting point like carbon, hafnium, or boron as well as applications that require high deposition rates which would exceed this temperature limit, effusion cells are of limited use. In these cases, electron beam evaporators are used. Here, an electron beam with an accelerating voltage of about 3 to 40 kV is directed onto the evaporation material. Due to the low penetration depth of electrons, their kinetic energy is converted to thermal energy at or near the material surface. This causes a local melting of the source material that leads to a material flux towards the substrate. Furthermore, this material flux has to be measured in-situ and controlled in order to obtain the correct stoichiometry one desires for the given film. Many different techniques are known for this, ranging from RHEED intensity oscillations (see section 2.2.1) that can be used for high-quality films only, ellipsometry for which the film has to be relatively transparent to the probing wavelength, mass spectroscopy where the integrated intensity of a specific spectral line is used, up to quartz crystal microbalances (QCM) which measure the shift in resonance frequency with increasing deposition mass on a crystal. To achieve compounds with a specific stoichiometry, modern semiconductor MBE systems use a shutter controlled thin film growth. Here, the sources are kept at a constant preset rate that is independent of the compound. During the deposition the shutters of each source are opened and closed consecutively for a set amount of time. As long as the temperature of the substrate is high enough to provide sufficient mobility to the impinging atoms, a stack of different monolayers is formed at first which then subsequently leads to the formation of the intended compound [22, 23].

The system used during this work is a standard UHV MBE system by Thermionics, with a base pressure of about 10^{-7} Pa (10^{-9} mbar). The unit is equipped with three e-gun evaporators as well as a



(a) Picture of the MBE unit used in this work.



(b) Schematic of the MBE unit used in this work.

Figure 5: MBE instrumentation

high-temperature effusion cell and a cooling shroud. As can be seen in the schematic in Fig. 5(b), in-situ growth monitoring is carried out via RHEED, while QCMs equipped with collimators are used for rate monitoring of individual sources. Contrary to typical semiconductor MBE systems, stoichiometry control is achieved through a feedback loop that controls the rate of each source independently. The nitridation was achieved through means of an rf radical source about which more details can be found in section 2.2.2. Details about the deposition process as well as the substrate treatment can be found in appendix C.

2.2.1 Reflection high-energy electron diffraction

Reflection high-energy electron diffraction is a versatile tool which can be used to obtain information about the surface structure and orientation, surface morphology, as well as the growth mode through the diffraction pattern. In addition, growth rates can be measured by RHEED intensity oscillations, making it a powerful tool for in-situ thin film growth monitoring. An electron gun accelerates electrons towards a sample at a low incident angle typically below 5° , resulting in diffraction of the electrons at the sample. The diffracted electrons then hit a phosphorus screen, resulting in a bright diffraction pattern which is usually recorded by a camera [24].

Only electrons that fulfil the Bragg condition

$$\vec{k}_d - \vec{k}_i = \vec{G} \quad (9)$$

with \vec{k}_d and \vec{k}_i being the diffracted and the incident wave vector of the electrons and \vec{G} being the reciprocal lattice vector are diffracted. Since RHEED is used with low incident angles θ , only the surface of the sample is probed. For this case of a quasi-two-dimensional layer, the reciprocal space evolves from a three-dimensional point grid into so called truncation rods that are parallel to the surface normal. As long as the scattering process is elastic with $|\vec{k}_d| = |\vec{k}_i| = k$, the Ewald construction can be used to determine the possible \vec{k}_d . In this case, all diffracted vectors must end on the surface of a sphere, called the Ewald sphere, with a radius of k . For this reason, all diffraction spots with the same order of diffraction form a circle, called Laue circle, on the screen [24].

By measuring the distances between the diffraction spots on the phosphorus screen, the reciprocal lattice spacing and by this the lattice constants for layers with known orientations can be calculated. For long distances between sample and screen d_s and a low order of diffraction, the truncation rod spacing g perpendicular to \vec{k}_i can be approximated by

$$g = k \frac{l}{d_s} \quad (10)$$

with l being the distance between two diffraction spots on the screen. In the next step, the lattice plane spacing d can be derived by $d = 2\pi/g$ from which the lattice constants can be calculated. A simpler method to obtain the lattice constants is to use a calibration substance, ideally a single crystalline substrate, with known lattice constants and therefore lattice spacing d_{cal} under a defined azimuth to

obtain a defined l_{cal} . From this, l_{mat} of the growing layer can be directly translated to its lattice spacing d_{mat} by

$$\frac{d_{cal}}{d_{mat}} = \frac{l_{mat}}{l_{cal}}. \quad (11)$$

This method has the advantage of cancelling out errors caused by the determination of the acceleration voltage as well as measurement uncertainties of the dimensions [24, 25].

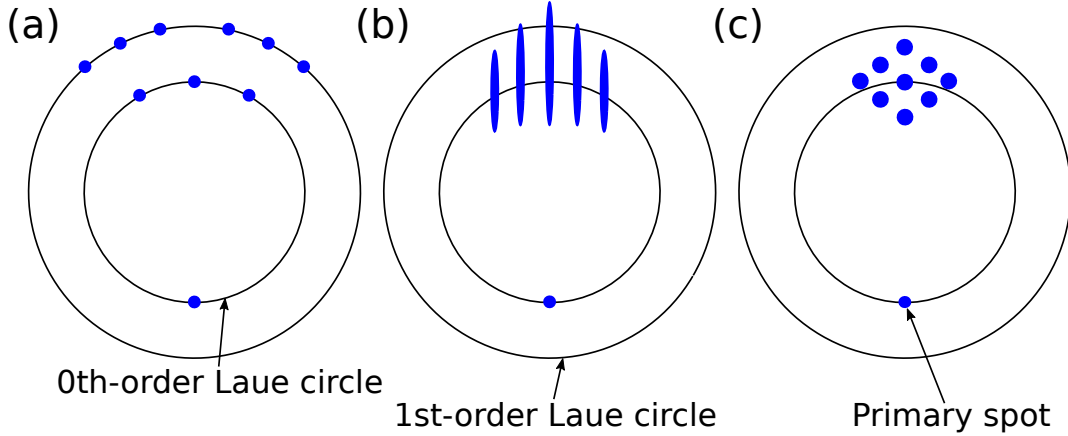


Figure 6: Schematic RHEED patterns (a) for ideally flat surfaces, (b) during step-flow growth, and (c) island growth.

In addition, the different growth modes, discussed in the previous section, can be distinguished by the changes of the pattern, displayed in Fig. 6. The ideal case for flat surfaces of two-dimensional lattices, observed for Frank-van der Merwe growth, results in the aforementioned sharp truncation rods that in turn give rise to sharp diffraction spots. For high step densities on the surface, encountered during step-flow growth, the truncation rods broaden. Additionally, the electrons that undergo diffraction have a certain range of energies due to which the Ewald sphere is not infinitely thin as would be the case for monoenergetic electrons. Both effects cause the spots to lengthen into streaks on the screen. When islands grow on the sample surface, the diffraction pattern resembles three-dimensional diffraction due to the reciprocal lattice reverting from the purely two-dimensional rods to a three-dimensional arrangement of smeared out spots [24].

2.2.2 Radiofrequency radical source

To achieve nitride or oxide thin films during some of the first thin film experiments, the background pressure of the corresponding gases was increased accordingly. However, in order to achieve a stable source operation and high-quality thin films via MBE, an as low as possible deposition pressure is required as was elaborated in section 2.2. By using a beam of atomic nitrogen or oxygen which has a higher reactivity than the respective molecular gas species, the pressure in the chamber as well as the deposition temperature can be significantly reduced while maintaining the same level of nitridation or oxidation [26]. Due to the low decomposition temperature of iron with nitrogen interstitials, these improvements are of special interest for this work [27, 28].

The origin of the atomic gas beam is a plasma discharge which is created through an inductively coupled

coil operating at 13.56 MHz. The electric field causes the electrons and atom cores to separate due to their mass difference, thus forming a plasma that is maintained by high energy electrons [29]. By the means of an aperture plate the gas flow out of the discharge tube is limited, therefore maintaining pressures sufficiently high to ignite and sustain a plasma discharge within the tube. In addition, the aperture thickness as well as its hole diameter influence the velocity distribution of the gas beam emitted by the source [30]. While the pressure required to strike a plasma depends on the ionization potential of the utilized gas, the pressure in the discharge tube can be reduced (or increased) to the desired operating point once the plasma discharge is formed. In order to adjust the nitridation and oxidation levels, two parameters are available: the pressure in the discharge tube that can be adjusted via the gas flow into the source as well as the rf power supplied. However, an increasing gas flow results in a nonlinear increase of the radical flux due to collisions mostly taking place between the gas atoms and the tube walls for low pressures, while higher pressures inside the tube promote intramolecular collisions until the plasma breaks down for even higher flows. Contrary to this behaviour, changes in the rf power translate linearly to the radical flux of the source, making it a more suitable parameter for precise stoichiometry scans with defined steps. To get an insight on the relative change in radical flux at different sets of parameters, the brightness of the plasma, measured by a photodiode, can be used [26–28].

For this work, an rf radical source (HD25, Oxford Applied Research) was used to nitride the samples during growth. To modify the parameter space for a stable plasma to the lowest possible flow and eliminate the risk of oxygen being released from a quartz discharge tube, a custom discharge tube and low flow aperture were designed and manufactured. Two aperture variants with either 41 or 65 holes of diameter of 0.2 mm, mechanically drilled by Drill Service (Horley) Ltd, ensured a stable plasma even to the lowest possible flow of 0.01 sccm that is available from the mass flow controller. The material used was HeBoSint D 100, a machinable boron nitride bought from Henze BNP AG. For all samples encompassed in this work, the aperture with 41 holes (see appendix A) was chosen and used.

2.3 Sputtering

Sputtering, another PVD technique, makes use of ion or atom bombardment in order to eject atoms and clusters out of a target onto a substrate where a thin film is formed. The components of thin film deposition sputter coaters are similar to that of MBE with a substrate holder/heater, source shutters and of course the sources themselves. Contrary to the evaporation techniques used in MBE, not only the thermodynamics of growth but also the kinetics of the clusters impinging on the substrate can be modified by changing the background gas pressure. The process of sputtering was first described approximately 160 years ago by Grove and Plücker and was occasionally used to make mirrors. Only after a publication by Crookes in 1891, research interest increased and several studies about sputtering yields of different materials as well as constant modifications and improvement to the process were performed subsequently [31]. However, it took until the 1980s for sputtering to become a commercially available process with a sputter coating machine by Leybold. Modern sputter coaters are widely used for magnetic hard disks, integrated circuits, as well as optical coatings. Many variations of the sputtering process exist, amongst others ion-beam sputtering, reactive sputtering, and ion-assisted sputtering can be found. Due to the relative similarity of these processes, only the radiofrequency magnetron sputtering that was used to synthesize the samples for this work will be described in more detail [21, 32].

When a radiofrequency of usually 13.56 MHz is applied between a capacitively coupled target and the chamber wall, the electrons and ions of the sputtering gas used are separated from each other due to their difference in mass, similar to the process within the radical source discussed in the previous section. Since no current can flow through the target because of its capacitive coupling, rf sputtering allows the use of insulating target materials. In addition, a negative potential forms on the target so that the positively charged sputter gas ions are accelerated towards it. Through gas ions colliding with the target surface, atoms and small clusters are ejected from the target [32].

The resulting erosion rate is not dependent on the temperature but only on the relative mass of the gas to the target material, the angle at which the gas ions impact on the target, as well as the ionization of the gas. The highest erosion rate is achieved when the atomic mass of the sputter gas is similar to that of the target, therefore maximizing the kinetic energy transfer from gas ions to target atoms. The amount of ejected particles per incident particles, called sputter yield Y , as a function of the ion energy is, exemplary shown for an iron target with Ar sputtering gas at an angle of 90° , 0.7 at 300 eV, 1 at 500 eV, and 1.7 at 1000 eV [33]. Interestingly, the sputtering yield is, within less than one order of magnitude, relatively similar for most materials. This lies in contrast to the vastly different vapour pressures of materials that need to be considered for film growth by MBE. The final erosion rate R can be calculated according to

$$R = 62.3 \frac{JY M_a}{\rho} \text{ \AA}/\text{min} \quad (12)$$

with J being the ion current density of the gas in mA/cm², M_a the atomic weight of the target atoms, and ρ the density of the target [33]. In addition to the rate, the mean free path of the ejected particles as well as the plasma intensity can be adjusted by the background pressure of the sputtering gas, providing a means to control the kinetic energy of the particles and the deposition rate at the substrate. Unfortunately, the necessary minimum pressure to achieve a plasma discharge severely limits the pressure

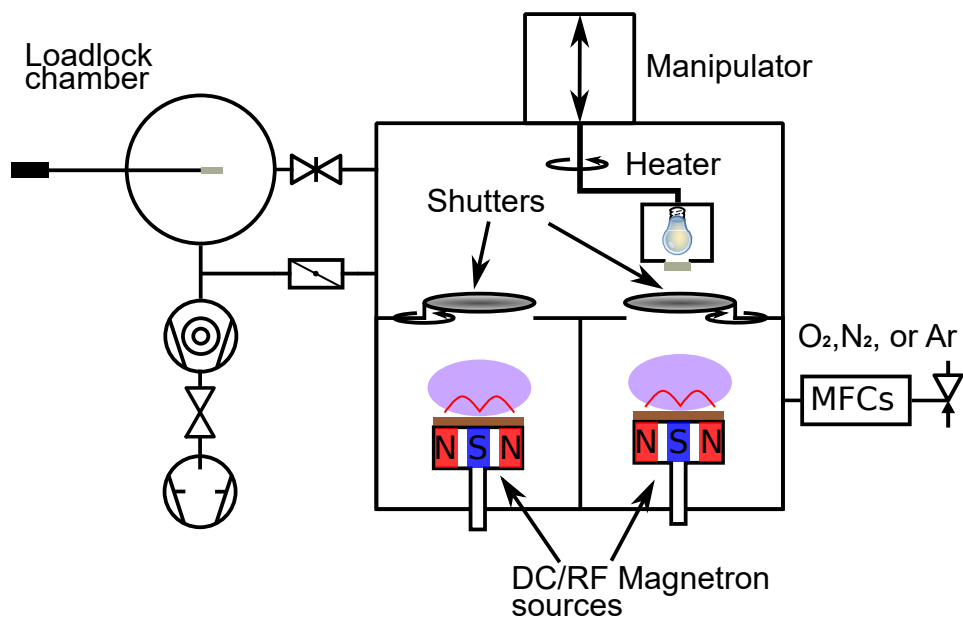
range in which one can sputter. Already in 1936, Penning discovered that a magnetic field increases the plasma intensity and thus reduces the necessary pressure to achieve a stable plasma [34]. This is caused by the Lorentz force \vec{F}_L that forces electrons with a velocity \vec{v} on cycloidal orbits in a magnetic field \vec{B} as described by the Lorentz equation

$$\vec{F}_L = q\vec{v} \times \vec{B} \quad (13)$$

in the absence of an electrical field \vec{E} . The magnetic field traps the electrons close to the target in cycloidal orbits which result in an increased collision probability between electrons and gas atoms, hence causing a higher ion density during the process. Typical planar magnetron sources, as were also used for this work, are schematically displayed in figure 7(b). The system used for this work is a standard UHV rf magnetron sputtering system, shown in figure 7(a), with a base pressure of about 10^{-6} Pa (10^{-8} mbar). It is equipped with three magnetron sources that can be operated with either dc or rf sputtering. Typically, argon is used as a sputtering gas and a butterfly valve is employed to control the pressure during the process, while additional gas inlets allow the use of up to two additional gases in order to grow, for example, nitride or oxide materials [32]. Further details on the sample growth process, especially the pre-sputtering of the target, is added in appendix C.



(a) Picture of the sputtering unit used in this work.



(b) Schematic of the sputtering unit used in this work.

Figure 7: Sputtering instrumentation

2.4 X-ray analysis techniques

The most frequently used analysis techniques used for this work are X-ray diffraction, short XRD, and X-ray reflectometry, short XRR. With these two techniques, the crystal structure with the lattice constants, crystallographic orientation of the film compared to the substrate, as well as the thicknesses and the roughnesses of the different layers can be determined amongst others, making them powerful tools towards optimizing the parameters of thin film growth. In order to keep this overview short, the generation of X-rays will be omitted from this section and only the background of XRD and XRR with respect to their application in crystallography will be explained. The device used for this work was a Rigaku SmartLab thin film diffractometer, equipped with a Cu- K_α rotary anode.

X-ray diffraction can only occur when the wavelength of the incident beam is of the same order of magnitude as the features to be observed. For this reason, typical X-ray wavelengths used for crystallography are in the range of 1 to 100 Å which corresponds to the range of distances between lattice planes in crystals and an according energy of around 0.1 to 10 keV. Back in 1913, the Bragg formulation of X-ray diffraction was developed by W.L. Bragg and W.H. Bragg after observing characteristic diffraction patterns of X-rays that were projected on crystalline samples [35]. It was concluded that a crystal is a periodical arrangement of atoms that act as the scattering centres, with parallel planes of atoms that have a fixed distance d . This periodical arrangement leads to a defined phase relation between the scattered X-rays. For a sharp peak to be observed, the incident as well as the diffracted beam have to have the same angle with respect to crystal planes. In addition, the X-rays diffracted from all planes parallel to the first plane have to contribute and interfere constructively. The well known Bragg law

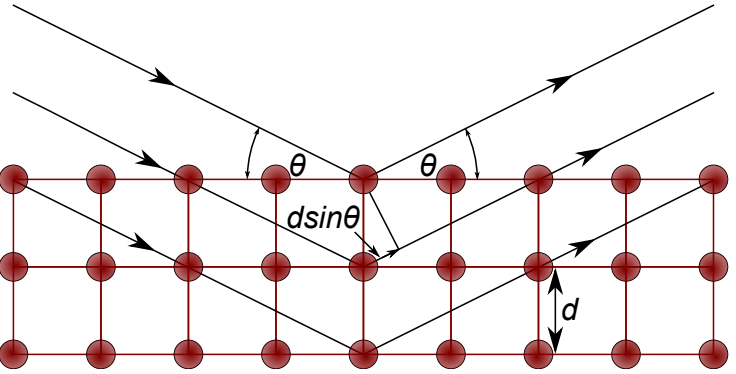


Figure 8: Geometric relationship between the incident and diffracted X-ray, the plane distance d , and the X-ray path difference $dsin\theta$.

is given by

$$m\lambda = 2dsin\theta \quad (14)$$

with m being the integer order of reflection, λ the wavelength of the X-ray, and θ the angle of incidence explains this behaviour that is displayed in figure 8. Equation 14 also explains the wavelength requirements for scattering with the lattice planes. For a maximum angle of $\theta = 180^\circ$, $sin\theta = 1$ which, inserted into the Bragg equation, gives the wavelength requirement of

$$\lambda < 2d. \quad (15)$$

It is important to note that the diffraction angles are only dependent on the unit cells geometry. X-ray diffractometers make use of this relationship by using for example Cu- K_α radiation with a fixed wavelength of 1.5406 Å. By then varying the incident X-ray angle and measuring the intensity of the diffracted beam, d -values can be experimentally measured and converted into the lattice constants a , b , and c [36].

In addition to the unit cell based diffraction direction, one also observes differences in the intensity of the diffracted beam up to a point of the disappearance of a diffraction peak predicted by the Bragg condition. This can be explained by the two origins of a scattered beam, the electrons and the atom itself. Electrons can elastically scatter X-rays by first being excited by the incident beam and then radiating coherent X-rays of the same wavelength and frequency as the incident beam, as described by the Thomson equation. A second scattering process, the Compton effect, can also occur between X-ray and electron. Here, a weakly bound electron is displaced by the X-ray, causing a deflection of the beam. This effect also reduces the energy of the photon and consequently increases the wavelength of the radiation. The scattering by an atom can be considered as the sum of Thomson scattering of each electron within the atom. However, since the electrons are placed at different positions around the nucleus, this scattering is depending on the scattering angle. To describe this, the atomic scattering factor f is introduced for a given direction:

$$f = \frac{A_a}{A_e} \quad (16)$$

with A_a the amplitude of the X-ray scattered by an atom and A_e the amplitude of an X-ray scattered by one electron. The maximum value of f equals the atomic number Z for a scattering angle of $\theta = 0$, since the scattered X-rays of all electrons are in phase and interfere constructively. For greater angles the scattered X-rays interfere more and more destructively, resulting in a reduced atomic scattering factor. However, f only considers the diffraction by one atom. To obtain the solution for the unit cell, first the amplitude and the phase of each scattered wave has to be taken into account, giving rise to the complex expression

$$Ae^{i\phi} = f e^{2\pi i(hu + kv + lw)} \quad (17)$$

with the intensity of the wave A , its phase ϕ , the miller indices h , k , and l , as well as the fractional coordinates $u = x/a$, $v = y/b$, and $w = z/c$. By then summing up the expression from equation 17 over all n individual atoms in the unit cell, the structure factor of a specific X-ray reflection F_{hkl} can be expressed through

$$F_{hkl} = \sum f_n e^{2\pi i(hu_n + kv_n + lw_n)}. \quad (18)$$

However, while F is a complex number containing both phase and amplitude information of the diffracted X-ray, only the intensity of the X-ray, corresponding to $|F|^2$, can be measured experimentally in most laboratory detectors. This so called phase problem can be solved mathematically by calculating the phase information of the wave. Another solution is the use of highly coherent X-rays, usually obtained by a synchrotron. If the coherence can be maintained from the source until diffraction, the phase information can be extracted experimentally [36, 37].

While XRD techniques make use of diffraction at an atomic level, XRR is a technique that uses reflection

to resolve the layer structure, density gradient, and interface roughness of a given system. This is accomplished by shining X-rays in a small angle, usually below 5° with respect to the surface, onto a sample. The occurring reflection can be explained by classical optics and is only dependent on the incident angle θ and the index of refraction n

$$n = 1 - \delta + i\beta, \quad (19)$$

with δ the dispersion and β the absorption, of the layers to be investigated. Since an XRR measurement probes the macroscopic scales in the system, it can also be performed on amorphous samples to resolve the geometric properties. Due to the refractive index n of X-rays for most materials being smaller than one, total reflection for θ being smaller than the critical angle of reflection θ_c occurs. The value of the critical angle can be used to calculate the density of the system by applying Snell's law at the critical angle and assuming $\beta = 0$. For small angles and only one layer, this results in

$$1 - \delta = \cos\theta_c \approx 1 - \frac{\theta_c^2}{2}. \quad (20)$$

Resolving equation 20 for θ_c , this gives

$$\theta_c = \sqrt{2\delta} = \sqrt{\frac{r_0\lambda\rho}{\pi}}, \quad (21)$$

where r_0 is the Bohr atomic radius and ρ is the density of the material. Hence, by determining θ_c , the density of a film can be calculated [36].

For angles $\theta > \theta_c$, the X-rays penetrate into the sample and are reflected at the interfaces of the film. This leads to angle dependent interference between the reflected beams, causing the characteristic fringes called Kiessig fringes to appear. Assuming $\beta = 0$ and taking Snell's law,

$$n\sin\theta = \sqrt{\theta_d^2 - 2\delta} \quad (22)$$

with θ_d being the angle between the surface and the beam within the layer. By replacing δ according to equation 21 and inserting it into $2t\sin\theta_d = m\lambda$ with t being the layer thickness, one obtains

$$2t\sqrt{\theta_d^2 - \theta_c^2} = m\lambda. \quad (23)$$

For more complex layer geometries, the recursive Parratt algorithm is used to calculate the contributions of all layers in the system by which the different thicknesses can be fitted [36, 38].

The third parameter that can be extracted from XRR measurements is the interface roughness. Non-ideal samples exhibit a non zero interface roughness at all interfaces. Small roughnesses that are distributed over several hundreds of nanometres can cause a misorientation of the surface with respect to the average

orientation. Larger local roughnesses with a lateral dimension from atomic level to a few nanometres cause a strong deviation of the surface orientation. The first type of roughness, also denominated as waviness, causes a broadening of the reflected beam which reduces the angular resolution of the measurement. The second type of roughness reduces the intensity of the reflected beam and can be quantified by the model of Névot and Croce [39]. It assumes that the expectancy value of the position of the interface, z_0 , is modulated by the Gaussian distribution

$$f(z) = \frac{1}{\sqrt{2\pi}\sigma_r} e^{-\frac{(z-z_0)^2}{2\sigma_r^2}} \quad (24)$$

where σ_r denotes the standard deviation as a measure for the roughness that is usually designated as the RMS roughness. For a system of N layers, σ can be calculated as the standard deviation of all contributing roughnesses

$$\sigma_r = \sqrt{\frac{1}{N} \sum_i (z_i - z_0)^2}. \quad (25)$$

As already been mentioned, this roughness causes a drop in the intensity of the reflected beam which can be expressed by a reduction of the ideal surface reflectivity R_0 according to the Debye-Waller exponential factor

$$R = R_0 e^{-\frac{4\pi\sigma_r^2 \sin\alpha}{\lambda}} \quad (26)$$

with α being the sliding angle [36, 39].

2.5 SQUID magnetometry

Throughout this work, the magnetic characterization was carried out in a Quantum Design Magnetic Property Measurement System (MPMS). In order to measure magnetic moments with a high sensitivity, this MPMS employs a superconducting quantum interference device (SQUID), a device whose function will be illustrated in the following. The DC SQUID was invented by R.C. Jaklevic et al. in 1964 and makes use of the DC Josephson effect which occurs between two superconductors that are connected by a thin non superconducting film [40]. As long as the thickness of this film is thinner than the coherence length of the superconducting material, Cooper pairs can tunnel through the films, maintaining the superconducting state of the whole system [41]. A SQUID consists of two Josephson junctions that are connected in a parallel circuit. Once an external magnetic field B_{ext} and a bias current I_b are applied to create a magnetic flux

$$\Phi_{ext} = B_{ext}A \quad (27)$$

to a SQUID of the area A , a circular screening current I_s is induced within the SQUID which in turn induces a magnetic field in order to cancel out the external magnetic field. The screening current is parallel to I_b and flows in the same direction within one branch of the circuit while it flows in the opposite direction in the other branch. This changes the total current to

$$I = \frac{I_b}{2} \pm I_s \quad (28)$$

in the respective branches. If the bias current is set to an operating point above the critical superconducting current I_c , an external flux will change the voltage drop across the SQUID due to one junction becoming ohmic in nature. Since the magnetic flux within the SQUID has to be quantized by the magnetic flux quantum Φ_0 , the screening current will change its direction along a change of the external magnetic flux to either increase or decrease it to integer values of Φ_0 . This in turn causes a periodic change of the voltage drop across the SQUID with a period of Φ_0 . With a shunt resistance R to eliminate the junction's hysteresis, the flux to voltage conversion can be described by

$$\Delta V = \frac{R}{L} \Delta \Phi \quad (29)$$

with L being the inductance of the SQUID [41, 42].

To reduce the noise caused by external interferences, specific pickup coil geometries can be used. They make use of the fact that an external field $B_{dipole} \propto 1/z^3$, with its origin at a distance z from the pickup coil is uniform in direction and magnitude at the position of the coil. Based on this effect, two pickup coils that are separated by a small distance d and are wound in the opposite sense cancel the effect of uniform fields and are therefore called first order derivative pickup coils. Even higher order derivative pickup coils can be used to further reduce the influence of external fields on the measurement. In addition, the indirect measurement by superconducting coils, as used in the MPMS, allows the placement of the SQUID in a magnetically shielded and separately cooled environment to further reduce external

influences. With the resulting high signal-to-noise ratio and the high sensitivity granted by the SQUID as well as the wide temperature range, these instruments are suitable for thin film samples that exhibit low magnetic moments [41].

However, a SQUID itself can only measure changes in the magnetic flux. One approach to measure the quantitative magnetic moment of a sample is to operate the SQUID as a zero field detector in a so called Flux-locked loop. In a constant external magnetic field, required to magnetize a sample, no signal is picked up. When the sample is moved through the pickup coils along the field direction, a change of the magnetic flux as a function of the sample position is created and induces a current I_s in the pickup coils. The SQUID detects this current by a coil that induces a magnetic flux Φ_s . A feedback loop is connected to the SQUID output and controls the current I_f through a second coil to create a magnetic flux Φ_f of the same magnitude as Φ_s , but in the opposite direction. If both fluxes exactly cancel each other out, the effective screening current I_b in the SQUID is 0. In this case, the signal of the SQUID stays constant. Since $I_s \propto I_f$, the magnetic moment of the sample can be calculated as a function of I_f [41,42].

3 Magnetism

A short introduction in the theory of diamagnetism will be given in section 3.1 to describe the magnetic behaviour of the substrates used. In the following, section 3.2, the basic principles governing the intrinsic properties of ferromagnets are discussed. A short introduction to the Weiss theory of ferromagnetism, which applies to localized magnetic moments, will be given. In the next step, the Stoner model of ferromagnetism will be discussed in order to explain the behaviour of delocalized electrons and the resulting non integer values of magnetic moments as observed in, for example, Fe and α' -Fe₃N. Finally, the underlying mechanisms for permanent magnets, the magnetic anisotropy in different crystals (magnetocrystalline anisotropy) as well as different shapes (shape anisotropy) are discussed in section 3.3.

3.1 Diamagnetism

Diamagnetism is present in every element and compound. Due to its small susceptibility, its effect is usually much smaller in magnitude compared to stronger magnetic responses caused by net magnetic moments available. In the Langevin theory of diamagnetism, a charge q travelling on a circular orbit with an angular frequency ω is considered. It can be viewed as a current I with

$$I = \frac{-q\omega}{2\pi} \quad (30)$$

which in turn induces a magnetic moment μ with

$$\mu = \frac{-q\omega r^2}{2}, \quad (31)$$

r being the radius of the circular orbit. For an electron that has an orbital angular momentum \vec{l} and the charge $q = e$, the magnetic moment can be written as

$$\vec{\mu} = \frac{-e}{2m_e} \vec{l}, \quad (32)$$

with m_e being the electron mass. If a magnetic field with the induction

$$\vec{B} = \mu_0 \vec{H}, \quad (33)$$

and μ_0 being the permeability of free space, is applied, $\vec{\mu}$ will be subjected to a torque according to

$$\vec{\tau} = \vec{\mu} \otimes \vec{B} = \mu_0 \frac{e}{2m_e} \vec{H} \otimes \vec{l}. \quad (34)$$

Here, the term $\mu_0 \frac{e}{2m_e} \vec{H}$ is the so called Larmor frequency ω_L which is in the range of GHz for electrons and in the range of MHz for protons and describes the precession of μ around \vec{B} . According to Faraday's

law, this precession will induce a magnetic moment $\vec{\mu}_p$ that is opposed to \vec{B} in its direction. The magnitude of $\vec{\mu}_p$ depends on $R^2 = x^2 + y^2$ by

$$|\vec{\mu}_p| = \frac{e|\omega_L| \langle R^2 \rangle}{2}. \quad (35)$$

If one considers an atom with the atomic number Z , the sum of all Z magnetic moments of the electrons contributes to the induced magnetic moment \vec{m} of the atom,

$$\vec{m} = -\frac{\mu_0 e^2 \vec{H}}{4m_e} \sum^Z \langle R_i^2 \rangle = -\frac{\mu_0 e^2 \vec{H}}{6m_e} \sum^Z \langle r_i^2 \rangle. \quad (36)$$

The electron travels on a surface of a sphere with $\langle R^2 \rangle = 2/3 \langle r^2 \rangle$ in case of a symmetric spherical orbit of the electron. For $\langle r^2 \rangle$ being the square of the average radius for all Z electrons in the atom, \vec{m} can be expressed by

$$\vec{m} = -\frac{\mu_0 e^2 \vec{H}}{6m_e} Z \langle r^2 \rangle. \quad (37)$$

From this expression, the magnetization \vec{M}_{dia} as the magnetic moment per unit volume can be calculated by multiplying \vec{m}_p with $N_0 \rho / A$, N_0 being Avogadro's number, ρ the density, and A the atomic weight, resulting in

$$\vec{M}_{dia} = -\frac{N_0 \rho}{A} \frac{\mu_0 e^2 \vec{H}}{6m_e} Z \langle r^2 \rangle. \quad (38)$$

As a direct consequence, the magnetic susceptibility $\chi_{dia} = M_{dia}/H$ is always negative and independent of the net magnetic moment of the atom as well as the temperature [18,43]. When plotting the magnetic moment of any diamagnetic material as a function of the applied field, a straight line with a negative slope is obtained. In an ideal case, the diamagnetic contribution can be easily subtracted from a measurement of a ferromagnetic thin film that is grown on top of a diamagnetic substrate. In reality, even single crystalline substrates contain a finite amount of ferro- and/or paramagnetic impurities. When looking at the SQUID measurement of an MgO substrate shown in Fig. 9, the data clearly deviates from the straight line expected

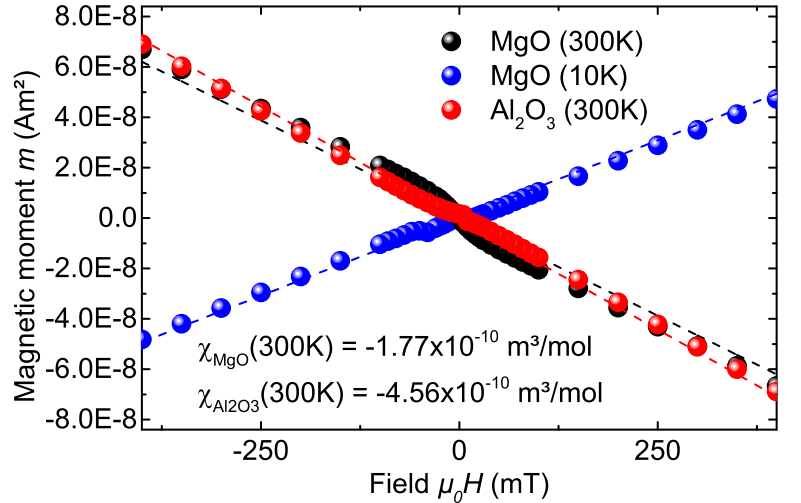


Figure 9: SQUID measurement of bare MgO and Al_2O_3 substrates at 300 K compared to MgO at 10 K (symbols). The displayed susceptibilities are extracted from a fit of the linear part of the measurements (dashed lines).

for a purely diamagnetic material. The susceptibility extracted from a fit of the linear regime in the measurement is $-1.77 \times 10^{-10} \text{ m}^3/\text{mol}$ ($-14.05 \times 10^{-6} \text{ emu/mol}$), which differs by nearly 40% from the reported value of $-1.29 \times 10^{-10} \text{ m}^3/\text{mol}$ ($-10.3 \times 10^{-6} \text{ emu/mol}$) [44]. In a direct comparison, the magnetic susceptibility of a Al_2O_3 substrate is $-4.56 \times 10^{-10} \text{ m}^3/\text{mol}$ ($-36.25 \times 10^{-6} \text{ emu/mol}$) which is nearly identical to the literature value of $-4.65 \times 10^{-10} \text{ m}^3/\text{mol}$ ($-37.0 \times 10^{-6} \text{ emu/mol}$) [44–46]. By measuring an MgO substrate at a temperature of 10 K, the paramagnetic response becomes even more dominant which results in a positive susceptibility of $1.4 \times 10^{-10} \text{ m}^3/\text{mol}$ ($11.16 \times 10^{-6} \text{ emu/mol}$) due to the $M \propto 1/T$ behaviour of paramagnetism which, at low temperatures, overcomes the temperature independent diamagnetism. The deviation of the measured curve from a straight line is not an effect of the substrates but is caused by the utilized measurement mode which has a comparably high error at low moments that occur at weak magnetic fields around or close to the point of origin.

3.2 Ferromagnetism

In opposition to diamagnetic atoms, ferromagnetic atoms have a net magnetic moment. The corresponding moments align parallel to form magnetic domains which in turn align themselves to minimize the magnetostatic energy of the system. In the demagnetized state, this causes all moments to cancel each other out.

3.2.1 Weiss theory of ferromagnetism

Pierre-Ernest Weiss empirically explained the deviation between the high fields necessary to saturate paramagnets compared to those necessary for ferromagnetic materials in 1906 [47]. To do so, he modified the Langevin theory of paramagnetism by assuming the existence of an internal molecular field \vec{H}_{int} that aligns the magnetic moments which in turn causes domains to be formed. Due to this internal field that was thought to arise from the magnetization of the neighbouring magnetic moments, the magnitude of the external field \vec{H} , required to change the orientation of these moments along the direction of the applied field, is greatly reduced. The resulting total field within the material then amounts to $\vec{H}_{tot} = \vec{H} + \vec{H}_{int}$. In addition, Weiss postulated that the internal field was proportional to the magnetization by the mean field constant or Weiss constant λ by $H_{int} = \lambda \vec{M}$ which is a measure for the strength of the exchange interaction. With this, the potential energy of an atomic magnetic moment inside the system is

$$E_{pot} = \vec{m} \cdot \vec{B} = -\mu_0 \vec{m} \cdot \vec{H}_{tot} = -\mu_0 \vec{m} \cdot (\vec{H} + \lambda \vec{M}). \quad (39)$$

For a system with N total magnetic moments, the magnetization follows the Langevin function, $\mathcal{L}(x) = \coth(x) - 1/x$, according to

$$M = Nm\mathcal{L}(a) \quad (40)$$

with the Langevin parameter

$$a = \frac{\mu_0 m H_{tot}}{k_B T} = \frac{\mu_0 m (H + \lambda M)}{k_B T} \quad (41)$$

as a ratio between the thermal energy and the potential energy field of an atom in a magnetic field. For values of $a \ll 1$, the higher order terms of the $\coth(a)$ can be neglected, resulting in

$$M = Nm \left(\frac{1}{a} + \frac{a}{3} - \frac{a^3}{45} + \dots - \dots + \dots - \frac{1}{a} \right) \approx Nm \frac{a}{3}. \quad (42)$$

From this, the susceptibility

$$\chi_{Weiss} = \frac{M}{H} = \frac{\mu_0 N m^2}{3k_B T - \mu_0 N m^2 \lambda} \quad (43)$$

can be derived. With the Curie temperature $T_C = \lambda C = \frac{\mu_0 N m^2 \lambda}{3k_B}$, and the Curie-Weiss constant C , the susceptibility can be rewritten as

$$\chi_{Weiss} = \frac{C}{T - T_C}, \quad (44)$$

also known as the Curie-Weiss law. However, it has to be noted that $a \ll 1$ only applies at high temperatures and that $T = T_C$ is a singularity in the susceptibility. In addition, Weiss' theory of ferromagnetism can not explain the non-integer μ_B values of magnetic moments that are observed in the elemental ferromagnets iron, cobalt, and nickel. Here, an itinerant electron model, described by the Stoner model of ferromagnetism in section 3.2.2, has to be applied [18, 43, 48].

3.2.2 Stoner model of ferromagnetism

For $3d$ transition metals and alloys, the assumption of localized electrons to explain the magnetic behaviour of the compound is not valid. The valence electrons are not localized at the atomic cores but have an itinerant character that is represented by the electronic band structure of the compound. For N electrons, the density of states describes the number of available states in an energy interval E by

$$g(E) = \frac{3n_0 \sqrt{E}}{2E_F^{2/3}} \quad (45)$$

with n_0 being the total density of electrons and E_F being the Fermi energy which is the highest energy of an occupied electron state at 0 K. For temperatures above absolute zero, the Fermi-Dirac distribution gives the probability of a state at an energy E to be occupied

$$f(E) = \frac{1}{e^{\frac{E-\mu}{k_B T}} + 1} \quad (46)$$

where μ is the temperature dependent chemical potential which equals E_F at 0 K. The density of occupied states is thereby

$$n(E) = g(E)f(E). \quad (47)$$

For $3d$ transition metals that exhibit a magnetic moment, this density of occupied states can be divided into two distributions, one for spin-up electrons and one for spin-down electrons. When a number of electrons in the energy range δE is transferred from spin-down to spin-up bands, the density of occupied states for spin-up is increased

$$n_\uparrow = \frac{1}{2}(n_0 + g(E_F)\delta E) \quad (48)$$

while the density of occupied states for spin-down is decreased

$$n_\downarrow = \frac{1}{2}(n_0 - g(E_F)\delta E). \quad (49)$$

Assuming the magnetic moment of each electron to be $1 \mu_B$, the splitting of the density of occupied states results in a spin based magnetization M of

$$M = \mu_B(n_\uparrow - n_\downarrow) = \mu_B g(E_F) \delta E \quad (50)$$

and an increase in the overall kinetic energy of the system

$$\Delta E_{kin} = \frac{1}{2} g(E_F) (\delta E)^2 \quad (51)$$

caused by increasing the energy of $g(E_F) \delta E / 2$ electrons by δE . In addition, the potential energy of the system changes according to

$$\Delta E_{pot} = - \int_0^M \mu_0 \vec{H} \cdot d\vec{M}' = -\mu_0 \lambda \frac{M^2}{2} = -\frac{\mu_0 \lambda}{2} (\mu_B g(E_F) \delta E)^2 \quad (52)$$

due to the internal magnetic field $H = \lambda M$, introduced in the previous section. The total change of the energy of the system

$$\Delta E = \Delta E_{kin} + \Delta E_{pot} = \frac{1}{2} g(E_F) (\delta E)^2 (1 - \mu_0 \lambda \mu_B^2 g(E_F)) \quad (53)$$

is then obtained by combining the equations 51 and 52. If $\Delta E < 0$, the splitting of spin-up and spin-down bands with a resulting magnetization is possible, resulting in

$$\mu_0 \lambda \mu_B^2 g(E_F) > 1, \quad (54)$$

the Stoner criterion for ferromagnetism in metals which is fulfilled only for iron, cobalt, and nickel which is in accordance to experiments. However, the Stoner model of ferromagnetism can not be applied to rare-earth based compounds, since the $4f$ electrons carry the magnetic moment of the rare-earths. These partially filled inner shells are not responsible for bonding, resulting in a localized magnetic moment. The internal magnetic field H is caused by interatomic exchange interactions which in turn are caused by the Coulomb interaction. With $U = \mu_0 \lambda \mu_B^2$, U being the Coulomb energy, the Stoner criterion can be expressed as

$$U g(E_F) > 1. \quad (55)$$

To estimate the magnetic moment, one can consider the $3d$ and the $4s$ band, having n_{sum} electrons in sum, to overlap to one effective band and apply a rigid band model that approximates a rectangular shape of the density of states. In addition, one spin state is assumed to be fully occupied with $n_\uparrow = 5$

and $n_{\downarrow} = n_{sum} - n_s - 5$ in the other state. For nickel with an electron configuration of $3d^8 4s^2$, $n_d = 10$. The magnetic moment of one atom m can then be calculated by

$$m = \mu_B(n_{\uparrow} - n_{\downarrow}) = \mu_B(10 - n_{sum} + n_s) \quad (56)$$

with n_s being the number of $4s$ electrons. The magnetic moment of nickel is $0.6 \mu_B$ per atom, resulting in an approximated n_s of 0.6. With the rigid band assumption, n_s is identical for all $3d$ transition metals, resulting in $m_{Fe} = 2.6 \mu_B$ with $n_{d,Fe} = 8$ and $m_{Co} = 1.6 \mu_B$ with $n_{d,Co} = 9$ which is reasonably close to the experimentally observed values of 0.62, 2.22 and $1.72 \mu_B$ per atom [18, 43, 48–50].

3.3 Magnetic anisotropy

Both previously discussed explanations for the occurrence of magnetic moments in atoms imply an isotropic distribution of these magnetic moments within a material. However, the magnetization vectors are known to reduce the magnetocrystalline energy

$$E_{mc} = \int_0^M \mu_0 \vec{H} \cdot d\vec{M} \quad (57)$$

of any given magnetic material by lying along specific crystallographic orientations, an effect expressed by the term magnetocrystalline anisotropy which is a material specific intrinsic property. In addition, the macroscopic shape of a sample can influence the demagnetization energy by changing these orientations. This so called shape anisotropy is an extrinsic parameter that is especially important to consider for thin films, where the magnetization lies preferably in the film plane due to a quasi-two-dimensional nature of the samples [18, 43, 48].

The preferred orientations of the magnetization vector are divided into the easy axes, the directions along which a small field is sufficient for all magnetization vectors being oriented parallel whereas the directions with the highest field required for saturation are called the hard axes.

3.3.1 Magnetocrystalline anisotropy

The origin of the magnetocrystalline anisotropy lies in the spin-orbit interaction and the dipolar interaction. However, since the contribution of the dipolar interaction is zero for cubic systems and negligible for lower symmetries, the focus is put on the effect of the spin-orbit interaction which is essentially a coupling between the electrons spin angular momentum \vec{s} and orbital angular momentum \vec{l} to result in an effective angular momentum,

$$\vec{j} = \vec{l} + \vec{s}. \quad (58)$$

The coupling of \vec{j} to the crystal lattice is caused by the coupling of the electrons orbital motion to the electrostatic fields of the nuclei which in turn gives rise to specific orientations of the electron orbits. Due to the spin orbit coupling, the spins in the material are therefore preferably oriented depending on the crystal structure [18, 43, 48].

For cubic crystals, the magnetocrystalline energy $E_{mc,c}$ is a function of the direction cosines a_i between the magnetization vector and the crystallographic directions. Due to the cubic symmetry, the series expansion for the magnetocrystalline energy should be independent on a sign change of a_i , resulting in the removal of odd power terms and all $a_i a_j$ where $i \neq j$. In addition, all a_i are equivalent, which causes the factor of the first term to become $a_1^2 + a_2^2 + a_3^2 = 1$, a constant term in the series expansion. The lowest not constant terms of the series are thus the fourth and sixth order terms which are usually sufficient to describe a sample. This leads to a magnetocrystalline anisotropy energy (MAE) of the form

$$E_{mc,c} = K_0 + K_1(a_1^2 a_2^2 + a_2^2 a_3^2 + a_3^2 a_1^2) + K_2(a_1 a_2 a_3)^2 \quad (59)$$

where K_i are the anisotropy coefficients of a material for a set temperature. E_{mc} is usually expressed in spherical coordinates, changing equation 59 to

$$E_{mc,c} = K_0 + K_1\left(\frac{1}{4}\sin^2\theta\sin^22\phi + \cos^2\theta\right)\sin^2\theta + \frac{K_2}{16}\sin^22\phi\sin^22\theta\sin^2\theta \quad (60)$$

where θ and ϕ are the angular coordinates. K_i are terms of energy densities in the range of 10^3 to 10^2 to 10^7 J/m³ (10^8 erg/cm³), increasing in magnitude with decreasing crystal symmetry. Since K_0 is isotropic, it can be ignored when the energy difference between two orientations is calculated. Depending on the magnitude as well as the sign of the anisotropy coefficients, the easy and the hard axis can be determined. Iron, the point of origin for this work, has values of $K_1 = 4.8 \times 10^4$ J/m³ (4.8×10^5 erg/cm³) and $K_2 = 5 \times 10^3$ J/m³ (5×10^4 erg/cm³) with $\langle 100 \rangle$ being the easy direction, $\langle 110 \rangle$ the semi-hard, and the crystal diagonal $\langle 111 \rangle$ the hard direction. For tetragonal crystals, the magnetocrystalline anisotropy $E_{mc,t}$ has a different angular dependence

$$E_{mc,t} = K_0 + K_1\sin^2\theta + K_2\sin^4\theta. \quad (61)$$

Since a second order term is involved in equation 61, the magnitude of $E_{mc,t}$ is larger than $E_{mc,c}$. This can be explained by calculating the magnetic anisotropy constants through perturbation theory with n th order systems requiring n th order perturbation theory. The last term of the Pauli Hamiltonian, the spin-orbit Hamiltonian \mathcal{H}_{SO} is expressed by

$$\mathcal{H}_{SO} = \frac{-e\hbar^2}{4m_e^2c^2r} \frac{dV(r)}{dr} \vec{l} \cdot \vec{s} = \xi(r) \vec{l} \cdot \vec{s} \quad (62)$$

with $\xi(r)$ being the radial average of the spin-orbit constant over the d -orbitals. By assuming the electrical field close to the nucleus to be spherical in nature,

$$\xi(r) = \frac{-e\hbar^2}{4m_e^2c^2r} \frac{dV(r)}{dr} = \frac{-\mu_B^2\mu_0Z}{2\pi r^3}. \quad (63)$$

For a hydrogen atom with only l and n as quantum numbers, eq. 63 can then be rewritten into

$$\xi = \frac{-\mu_B^2 \mu_0 Z^4}{2\pi a_0^3 n^3 l(l + \frac{1}{2})(l + 1)}. \quad (64)$$

Due to ξ being proportional to Z^4 , heavy elements are used in permanent magnets to achieve a large spin-orbit interaction and through it, a large magnetocrystalline anisotropy. The change in energy ΔE_{SO} for a crystal where a second order anisotropy constant applies is expressed by

$$\Delta E_{SO} = \sum_{exc} = \frac{|\langle exc | \mathcal{H}_{SO} | gr \rangle|^2}{E_{gr} - E_{exc}} \quad (65)$$

with exc and gr labelling the excited and ground state, respectively [51]. By considering only excited states above the fermi level, the anisotropy constant for an uniaxial system can be estimated through the d -band width w and the spin-orbit constant by

$$K_1 \sim \frac{\xi^2}{w}. \quad (66)$$

Accordingly, the n th order anisotropy constant K_1 can be estimated by

$$K_1 \sim \frac{\xi^n}{w^{n-1}}. \quad (67)$$

Since ξ is of the order of tens of meV while w is between 1 and 10 eV, a higher n effectively reduces the magnitude of K_1 [43, 51].

Experimentally, the anisotropy constant K_1 can be directly approximated from a $M-H$ -loop by assuming the existence of an anisotropy field \vec{H}_a which is parallel to the easy direction. If the magnetization lies in the plane of a cubic crystal, $\phi = 0$, resulting in $E_{mc,c} = K_0 + K_1 \cos^2 \theta \sin^2 \theta$. When minimizing the total energy of the system, comprised of the magnetostatic and anisotropy energy, according to

$$\frac{\partial E_{tot}}{\partial \theta} = \frac{\partial}{\partial \theta} (E_{mc,c} - \mu_0 M H_a \sin \theta) = 0, \quad (68)$$

the anisotropy constant can be calculated by

$$2K_1 \theta = \mu_0 M H_a \theta \Leftrightarrow K_1 = \frac{\mu_0 H_a M}{2}, \quad (69)$$

with the small angle approximation of $\sin \theta \approx \theta$. The anisotropy field can be easily obtained as the field where the easy- and the hard-axis magnetization curves intersect [18, 43, 48].

3.3.2 Shape, surface, and strain anisotropies

Although the dipolar interaction plays only a minor role for the magnetocrystalline anisotropy, it is the origin of the shape anisotropy which plays a major role in magnetic thin films. The magnetostatic energy of an ellipsoid is given by

$$E_{ms} = \frac{\mu_0}{2} N M_s^2 \quad (70)$$

where N is the demagnetization factor. For any ellipsoid, the demagnetization factors in the easy direction along the elongated axis, N_e , and the hard direction perpendicular to the elongated axis, $N_h = 1/2(1-N_e)$, result in a magnetostatic energy of

$$E_{ms} = \frac{\mu_0}{2} N_h M_s^2 \sin^2 \theta + \frac{\mu_0}{2} N_e M_s^2 \cos^2 \theta, \quad (71)$$

with the components of the magnetization along the easy $M_{s,e} = M_s \cos \theta$ and $M_{s,h} = M_s \sin \theta$ along the hard axis. By rearranging,

$$E_{ms} = \frac{\mu_0}{2} N_e M_s^2 + \frac{\mu_0}{2} (N_h - N_e) M_s^2 \sin^2 \theta \quad (72)$$

takes the form of an uniaxial anisotropy with $K_0 = \mu_0 N_e M_s^2 / 2$ and the shape anisotropy constant $K_s = \mu_0 M_s^2 (1 - 3N_e) / 4$. For a thin film in the xy -plane, the demagnetization factor is

$$\begin{pmatrix} N_x \\ N_y \\ N_z \end{pmatrix} = \begin{pmatrix} 0 \\ 0 \\ 1 \end{pmatrix} \quad (73)$$

which results in a shape anisotropy constant of $K_s = -\mu_0 M_s^2 / 2$. For iron, $K_{s,Fe} = -1.85 \times 10^6 \text{ J/m}^3$ ($-1.85 \times 10^7 \text{ erg/cm}^3$) is larger in magnitude than the magnetocrystalline anisotropy, imposing an easy-plane anisotropy in the film plane [18, 43, 48].

An additional anisotropy that is especially important for nanoparticles and thin films is the surface anisotropy K_{sf} . The topmost surface layer has a major impact on the surface anisotropy due to the broken long range order which is also manifested, albeit to a smaller degree, in the following layers. For the magnetic transition metals Cr, Mn, Fe, Co, and Ni, the density of atoms is between 8.33×10^{28} (Cr) and $9.11 \times 10^{28} / \text{m}^3$ (Ni). With Néel's approximation of the surface anisotropy of approximately 1 mJ/m^2 per atom, this gives rise to an anisotropy of the surface layer of about 4.17×10^6 (4.17×10^7) (Ni) to $4.55 \times 10^6 \text{ J/m}^3$ ($4.55 \times 10^7 \text{ erg/cm}^3$) (Cr) [52]. Since the surface anisotropy scales inversely with the ratio of surface to volume, a total or effective anisotropy

$$K_{tot} = K_v + \frac{K_s f}{t} \quad (74)$$

can be formulated with the volume anisotropy constant of the films' material K_v and the film thickness t . For very thin films below a critical thickness t_c the surface anisotropy can cause a spin reorientation,

causing the easy axis to point out of the film plane against the in-plane easy axis imposed by the shape anisotropy [18, 43, 48].

The last contribution to the anisotropy that will be discussed in this section is the strain anisotropy K_{st} which is mostly only relevant for thin films. This anisotropy depends on the stress σ and the magnetostriction constant λ along a certain direction, according to

$$K_{st} = \frac{3}{2}\lambda\sigma. \quad (75)$$

Contrary to the surface anisotropy that is exclusively present in the few topmost surface layers, the strain can be maintained for several layers before relaxation occurs. Due to this, the intermediate thickness regime with thicknesses above t_c is dominated by the strain anisotropy. As an example, an iron thin film with a Young's modulus of $2.1 \times 10^{11} \text{ N/m}^2$ that is grown on MgO with a mismatch of -3.68% results in a stress of $-7.73 \times 10^9 \text{ N/m}^2$. With the bulk magnetostriction constant λ_{100} of -2×10^{-5} [53], the strain anisotropy constant amounts to approximately $2.32 \times 10^5 \text{ J/m}^3$ ($2.32 \times 10^6 \text{ erg/cm}^3$) which is large enough to alter the orientation of the easy axis [18, 43, 48].

Depending on the ratio of the total uniaxial anisotropy comprised of the surface and bulk anisotropies to the shape anisotropy for materials exhibiting a perpendicular magnetic anisotropy, the effective easy axis is altered. This is described by the quality factor

$$Q = -\frac{K_u}{K_s}, \quad (76)$$

where K_u denotes the strength of uniaxial perpendicular anisotropy. For the shape anisotropy being larger than the uniaxial anisotropy, $Q < 1$ and the easy axis lies in-plane. For $Q > 1$, the magnetization is not entirely out-of-plane but canted at an angle which increases asymptotically towards 90° as a function of the uniaxial anisotropy [18, 48].

4 Literature review on α'' -Fe₁₆N₂

Iron nitrides offer a wide variety of mechanical, electrical, and magnetic properties, making it a system of interest for research as well as applications due to its constituents' abundance. When focusing on the magnetic properties, the net magnetic moment that is observed increases with the relative iron concentration of the different phases. With an equal amount of iron and nitrogen, corresponding to the highest nitrogen concentration available in this system, two cubic FeN phases exist. For the NaCl-type γ''' -FeN with a lattice constant of 4.5 Å, antiferromagnetism was observed at 4.2 K with a Néel temperature around 220 K [54–57]. Interestingly, the ZnS-type γ'' -FeN with a slightly smaller lattice constant of 4.33 Å was shown to have no local magnetic moment at the iron site, resulting in a stable nonmagnetic character with metastable antiferro- and ferromagnetic variations which are energetically only slightly less favourable [54, 55, 58]. Similarly, ζ -Fe₂N was examined with Mössbauer spectroscopy by Hinomura et al., revealing a paramagnetic doublet at temperatures from room temperature down to 10 K, below which antiferromagnetism was observed. Having a variable stoichiometry, ϵ -Fe_xN with x between 2 and 3.2 is a ferromagnetic hexagonal phase with a wide range of saturation magnetization values, starting at about 202 kA/m (202 emu/cm³) for $x = 2.3$ over 907 kA/m (907 emu/cm³) in the case of $x = 3$ up to 1418 kA/m for $x = 3.2$ (1418 emu/cm³) [59–61]. Similar to the trend of the saturation magnetization observed for this phase, the Curie temperature is 567 K for $x = 3$ and drops rapidly with increasing nitrogen content, down to about 300 K for $x = 2.3$, while ϵ -Fe_xN becomes paramagnetic for $x < 2.3$ [61, 62]. In addition to their ferromagnetic ordering, ϵ -Fe_xN as well as γ' -Fe₄N have a high spin-polarization, making both phases potentially interesting for spintronic applications [63]. γ' -Fe₄N is made up of an fcc iron lattice with one nitrogen atom at the body centre. With a higher iron content compared to ϵ -Fe_xN, γ' -Fe₄N has a higher saturation magnetization and Curie temperature of about 1432 kA/m (1432 emu/cm³) and 761 K, respectively [63, 64].

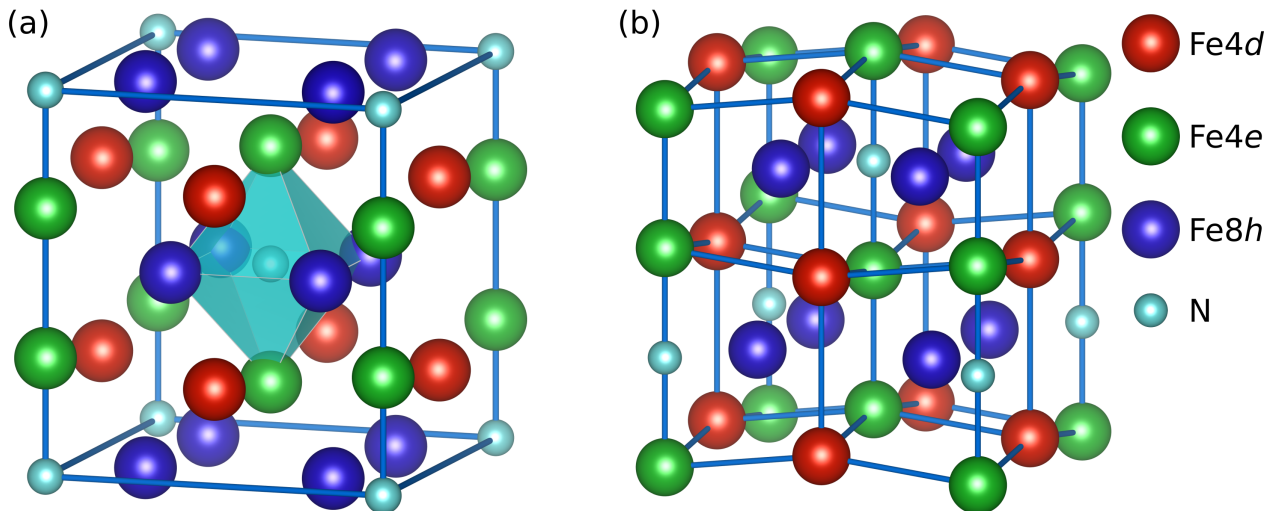


Figure 10: (a) bct unitcell of α'' -Fe₁₆N₂ with $a = 5.72$ Å and $c = 6.29$ Å, (b) the same structure but displayed with a z-offset. Drawn according to structural data reported by K.H. Jack [65].

However, since ϵ -Fe_xN and γ' -Fe₄N are soft ferromagnets with a saturation magnetization below that of α -Fe, the only phase of interest as a permanent magnet candidate is α'' -Fe₁₆N₂. First described by

Jack in 1951, $\alpha''\text{-Fe}_{16}\text{N}_2$ is a metastable phase and lies in thermodynamic competition with two stable phases, $\alpha\text{-Fe}$ and $\gamma'\text{-Fe}_4\text{N}$ [65–67]. This makes the synthesis of $\alpha''\text{-Fe}_{16}\text{N}_2$ difficult, as illustrated by the thermodynamic equilibrium phase diagram of the iron nitrogen system, where $\alpha''\text{-Fe}_{16}\text{N}_2$ occupies only a narrow space at exactly 11.1 at.% nitrogen content in a small temperature window up to 486 K [67,68]. The nitrogen atoms are ordered and occupy every twenty fourth octahedral interstitial position in a bcc $\alpha\text{-Fe}$ lattice which, in addition to a doubling of the lattice constants to a $2 \times 2 \times 2$ bcc unit cell, leads to a distortion of the lattice resulting in a tetragonal structure with the space group $I4/mmm$ and lattice constants $a = 5.677 \text{ \AA}$ and $c = 6.253 \text{ \AA}$, resulting in a c/a ratio of 1.1 [65,66,69]. By displaying the structure of $\alpha''\text{-Fe}_{16}\text{N}_2$ with a z-offset, as shown in Fig. 10(b), the interstitial arrangement and the according distortion along the c -axis can be visualized more clearly. Depending on the distance and the arrangement of the Fe atoms relative to the octahedral N interstitial, three different Fe sites, $4d$, $4e$, and $8h$ can be distinguished and are marked in Fig. 10(a) and (b) [65]. The $4e$ and the $8h$ sites are similarly close to the nitrogen atom with a distance of 1.93 and 1.8 \AA and occupy the axial positions as well as the positions in the N plane, thereby forming a distorted octahedron while the $4d$ site is the furthest away from the nitrogen with a distance of 3.26 \AA [65,70].

The magnetic properties of $\alpha''\text{-Fe}_{16}\text{N}_2$ were not known until 1972, when Kim and Takahashi deposited thin films composed of a mixture of $\alpha\text{-Fe}$ and $\alpha''\text{-Fe}_{16}\text{N}_2$ onto glass substrates in a low pressure nitrogen atmosphere. After determining the volume fraction of both phases from temperature dependent magnetization measurements, a saturation magnetization of 2250 kA/m (2250 emu/cm³) and a corresponding magnetic moment per iron atom of $3.0 \mu_B$, considerably higher than the values for $\alpha\text{-Fe}$ of 1710 kA/m (1710 emu/cm³) and $2.2 \mu_B$ respectively, were ascertained [49,71]. For nearly two decades, several attempts to reproduce thin films with similarly high saturation magnetization values by sputtering [72,73], ion reacting deposition [74], or chemical vapour deposition [75] were not successful. Finally, a research group of the Hitachi Research Laboratory grew thin film samples containing a high volume fraction of $\alpha''\text{-Fe}_{16}\text{N}_2$ on GaAs(100) and InGaAs(001) substrates by MBE. $\alpha''\text{-Fe}_{16}\text{N}_2$ with a saturation magnetization as high as 2548 kA/m (2548 emu/cm³) with a magnetic moment, later referred to as a giant magnetic moment, of $3.5 \mu_B$ per iron atom was reported for these samples [76,77]. Their first report in 1991 also contains one of the few estimations of the Curie temperature, which was extrapolated to be at about 813 K, a temperature well beyond the decomposition of the phase [77]. Interestingly, Sugita et al. also measured the anisotropy constant of $\alpha''\text{-Fe}_{16}\text{N}_2$ by torque magnetometry at room temperature and found it to be identical to that of $\alpha\text{-Fe}$ with $K_1 = 4.8 \times 10^4 \text{ J/m}^3$ ($4.8 \times 10^5 \text{ erg/cm}^3$) [77,78]. This report stands in contrast to Nakajima and Okamoto who, despite of reporting a saturation magnetization of only 1911 kA/m (1911 emu/cm³), found evidence for a reorientation of the easy axis from lying in the film plane to pointing out of plane parallel to the $\langle 001 \rangle$ direction of $\alpha''\text{-Fe}_{16}\text{N}_2$. In addition to this perpendicular magnetic anisotropy (PMA), an increase of the magnetocrystalline anisotropy to $K_1 = 6.2 \times 10^5 \text{ J/m}^3$ ($6.2 \times 10^6 \text{ erg/cm}^3$) was observed [79]. These first reports of a high saturation magnetization with a potentially giant magnetic moment in combination with a magnetocrystalline anisotropy in the range of commercial magnets with $K_1 = 3.7 \times 10^6 \text{ J/m}^3$ ($3.7 \times 10^7 \text{ erg/cm}^3$) for Nd₂Fe₁₄B [80] or $K_1 = 3.6 \times 10^5$ to roughly $5 \times 10^5 \text{ J/m}^3$ (3.6×10^6 to $5 \times 10^6 \text{ erg/cm}^3$) for SrFe₁₂O₁₉ [18,81] motivated many research groups to investigate $\alpha''\text{-Fe}_{16}\text{N}_2$ in the following years, as summarized in table 1.

The first section of this chapter, section 4.1, describes and discusses the origin of the magnetic moment in α'' -Fe₁₆N₂ based on literature reports. In the following, section 4.2 brings up and elucidates the reported values for its magnetocrystalline anisotropy as well as the occurrence of PMA. Finally, section 4.3 deals with the literature available on the thermal stability of α'' -Fe₁₆N₂, which includes a discussion of the decomposition mechanism and reports of possible improvements of the temperature stability of the phase.

4.1 Origin of the giant magnetic moment in α'' -Fe₁₆N₂

Shortly after the discovery of the giant magnetic moment, theoretical investigations based on the linearised muffin-tin orbital (LMTO) as well as the augmented spherical wave (ASW) method were conducted to find the origin of this giant magnetic moment. It was found that the different Fe sites exhibit different magnetic moments, the highest magnitude of which was found to be in the range of 2.74 to 2.89 μ_B for the 4*d* site while the 4*e* and 8*h* site, being closer to the nitrogen atom, have a lower magnetic moment between 2 and 2.4 μ_B [70, 82, 83]. The increased moment on the 4*d* site was explained by a reduction of the occupancy of the spin down state in combination with a *d*-band narrowing, both due to the long bond length to the nitrogen and the longer near-neighbour Fe distance, resulting in a charge transfer between the inequivalent iron sites compared to α -Fe [82, 83]. Contrary to this, the hybridization between the nitrogen atom and the 4*e* as well as the 8*h* sites causes a delocalization of the *d*-band which reduces their magnetic moment. Despite the greatly increased magnetic moment on the 4*d* site compared to the moments of α -Fe, the average magnetic moments found in these early calculations was found to lie between 2.4 and 2.5 μ_B [70, 82, 83]. Min and Sakuma both conclude, that the lattice expansion caused by nitrogen interstitials is the origin of the increased average magnetic moment on all sites while the 3*d*-2*p* hybridization between the nitrogen and the octahedrally coordinated iron atoms around it counteract this effect to a certain degree by decreasing the spin imbalance in the neighbouring iron atoms around the nitrogen interstitial [82, 83].

The scaling of the magnetic moments with expanding lattice agrees well with calculations performed by several groups who analysed the effect of lattice expansion upon α -Fe and α'' -Fe₁₆N₂. In all cases, a monotonously increasing trend for the magnetic moment as a function of the lattice volume was found, although Sims et al. reason that through the simultaneous increase of both parameters the net gain of magnetization is insignificant [84–86]. Experimental results by Mitsuoka et al., Takahashi et al., and Okamoto et al. were among the first to show a tendency for an increased magnetic moment with increased unit cell volume. However, in the latter reports the long range nitrogen ordering in the samples, presumed to be another reason for increased magnetic moments, is increasing simultaneously, thus preventing a precise statement on the matter [87–89].

Table 1: Reported substrates, buffer layers, and deposition temperatures T_s (for thin film samples) as well as sample production techniques with respect to the obtained M_s and K_1 . If no sample density was reported, the M_s values for the bulk samples were obtained via the theoretical density of α'' -Fe₁₆N₂.

Substrate	Technique	Buffer layer	M_s /(kA/m, emu/cm ³)	K_1 /(J/m ³ , (erg/cm ³))	T_s /K
GaAs	FTS	Fe, Ag	1910 [90], 2133 [91–93], 2308 [94], 2500 [95]	9×10^5 (9×10^6) [93]	300 [90–95]
	IBAD	-	1762 [96]	-	-
	MBE	-	1650 [97], 2387 [76,98], 2570 [99]	6.4×10^5 (6.4×10^6) [100]	300, 373 [98], 423 [76], 473 [98], 473 [98,99]
	Sputtering	Fe, Ag	1910 [89], 1989 [101], 2069 [102,103]	-	300 [89, 101–103], 373, 423 [89]
Ge	Sputtering	-	1710 [104,105]	-	300 [104,105]
Glass	Evaporation	-	1873 [106], 2250 [71]	8.3×10^4 (8.3×10^5) [106]	300 [71,106]
	Ion nitriding	-	2210 [107]	-	483 [107]
	Sputtering	-	1829 [108], 2342 [109]	-	300 [108,109]
In _{0.2} Ga _{0.8} As	MBE	Fe	2374 [110–112] 2548 [77,99,113]	4.8×10^4 (4.8×10^5) [77], 1.6×10^6 (1.6×10^7) [111], 7.8×10^5 (7.8×10^6) [110]	423 [77,110], 473 [99,113], 473 – 513 [111,112]
MgO	FTS	Fe, Ag	1710 [114], 1725 [88], 1770 [115–117] ((FeCo) ₁₆ N ₂),1890 [118], 2499 [119]	-	300 [88,114–119]
	Ion implantation	-	1911 [79,120]	6.2×10^5 (6.2×10^6) [79]	300 [79,120]
	Sputtering	Fe, Ag	1671 [121], 1859 [122], 1900 [123,124], 1911 [125]	4×10^4 (4×10^5) [121]	373 [122–125]
NaCl	Sputtering	-	2215 [126]	-	423 [126]
Si	Sputtering	-	1800 [127], 2223 [128], 2308 [129]	-	400 [128], 473 [127]
-	Ball milling	-	1562 [130]	-	-
-	Field anneal	-	1688 [131] (rods)	-	-
-	Ion implantation	-	1673 [132], 2201 [133]	-	-
-	Powder nitridation	-	945 [134], 1264 [135], 1443 [136], 1539 [137], 1599 [138], 1725 [139], 1740 [140, 141], 1896 [142], 2119 [143]	2.7×10^5 (2.7×10^6) [135], 6.9×10^5 (6.9×10^6) [141], 9.6×10^5 (9.6×10^6) [140]	-
-	Strained wire	-	2037 [144]	-	-

Finally, three years later, Okamoto et al. presented proof of the correlation between magnetic moments from 2.5 up to $2.8\mu_B$ with respective unit cell volumes of about 204 and 205.8\AA^3 independent of the nitrogen ordering [102,103]. These results were confirmed by Dirba et al., who demonstrated a linear scaling of the magnetic moment with the c lattice constant up to about $2.6\mu_B$ for as grown samples containing only disordered α' -Fe₈N [145]. Polarized neutron reflectometry (PNR) results presented by Ji et al. and Zhang et al. support this assumption and add a potential explanation for a giant magnetic moment. By fitting the reflectivity of upwards and downwards polarized neutrons, the saturation magnetization as a function of the probing depth was obtained for α'' -Fe₁₆N₂ containing samples. Saturation magnetization values between approximately 2300 and 2499 kA/m (2300 and 2499 emu/cm^3) were found in a few nanometre thick layer at the interface. It was shown that the magnitude of the strain, controlled by the thickness of the buffer layer, had a direct impact on the interfacial saturation magnetization [94,119].

The above-mentioned moment reduction for the closest iron neighbours was confirmed by Coehoorn et al., who used the full-potential linearised-augmented-plane-wave (FLAPW) method and employed the local spin-density approximation (LSDA) to calculate a virtually distorted bct iron system with the lattice constants of α'' -Fe₁₆N₂. They find that for bct iron the average moment per atom is $2.41\mu_B$, slightly higher than their result obtained for α'' -Fe₁₆N₂, which is found to be $2.37\mu_B$. To validate these results, γ' -Fe₄N moments are calculated, confirming a similar reduction in moment by hybridization as also experimentally observed by Frazer [146,147]. Similarly, band calculations based on the improvement of the LSDA by the generalized gradient approximation (GGA) or the self-interaction correction (SIC) yield average magnetic moments of $2.5\mu_B$ and $2.4\mu_B$, respectively [148,149].

In addition, Lai et al. and Umino et al. both discuss, that the many-body effect of screening needs to be taken into account in order to properly explain the magnetism in α'' -Fe₁₆N₂ [148,149]. When comparing their LSDA to their LSDA+U results, Lai et al. find that the introduction of the on-site Coulomb interaction by the Hubbard U parameter results in an average magnetic moment of $2.85\mu_B$, corresponding to a saturation magnetization of roughly 2080 kA/m (2080 emu/cm^3), caused by an increased spin imbalance which is most pronounced for the $4d$ site. However, they argue that the magnitude of the U parameter has a strong impact on the results and needs to be further investigated [148]. A similar conclusion is reached through the comparison of GGA+U, GW, hybrid functional method (HSE06), and constrained random-phase approximation (cRPA) by Sims et al. resulting in average moments up to $2.9\mu_B$ per iron atom with HSE06. While these results are closer to the giant magnetic moments of $3\mu_B$ and higher, they have to be considered carefully since simultaneously performed calculations of the magnetic moments in α -Fe yielded magnetic moments up to $2.6\mu_B$ [86].

While the previously discussed models based on the LSDA provide a good understanding for saturation magnetization values between approximately 1710 (2.15) and about 1900 kA/m (1900 emu/cm^3) without contradicting the limit of the Slater-Pauling curve, no reasonable explanation for a giant moment exceeding an average magnetic moment of $3\mu_B$ per iron atom was found. In order to finally fill this gap, Ji et al. stated that a combined itinerant and localized electron model with partially localized electrons which show a long range order would be necessary to properly describe the magnetism of α'' -Fe₁₆N₂ [150]. They state that the Fe-N octahedra are isolated from each other due to the relatively large distance between the $8h$ and $4e$ sites of two different octahedra, causing a charge transfer between the inside ($8h$ and $4e$ sites) and the outside ($4d$ sites) of the octahedra. This charge difference arises due to on-site Coulomb interaction between the octahedra and the $4d$ sites which are considered as a metallic iron environment with a small U value around 1 eV . It is stated that, in line with the observations of Lai et al., the use of two different U values is necessary to properly take the screening into account [148,150]. The resulting magnetic structure has localized orbitals in the octahedral as well as delocalized orbitals due to hybridization to the $4d$ site, declared to be a necessary effect for a ferromagnetic long range ordering. Ji et al. observe, that small U values on the $4d$ site indeed favour large magnetic moments while for the other sites, large U values exceeding 6 eV give rise to an average magnetic moment above

$3\mu_B$ per iron atom. However, Ji et al. state that a realistic choice of U only yields moments of about $2.8\mu_B$, thus falling short of the experimentally observed giant moment [150].

In a subsequent experimental report of the same group, it was observed that the ordering of Fe-N octahedra in the structure leads to an increase of the magnetic moment. Ji et al. explain this increase by considering the randomized iron octahedra positions in α' -Fe₈N which are statistically scattered and therefore not necessarily separated from each other. Through a binomial distribution, the percentage of iron sites with x nitrogen atoms as nearest neighbour were calculated to be 44.88%, 38.47%, 13.74%, and 2.61% for $x = 0, 1, 2,$ and $3,$ respectively. It is discussed that compared to α'' -Fe₁₆N₂, where 75% of the iron sites have only one nearest nitrogen neighbour, this distribution leads to a bandlike behaviour similar to iron and thus causes a reduction of the average magnetic moment to about $2.6\mu_B$ per iron atom [92]. However, when the structure is perfectly ordered, the iron octahedra are separated from each other which leads to highly localized moments for the $4e$ and $8h$ sites which therefore have an increased magnetic moment. This ordering, measured by the α'' -Fe₁₆N₂ (002) reflex, occurred only after prolonged annealing of around 2 hours up to 90 hours or longer at 373 to 473 K [77,88,89,91,92]. With ideally every other octahedral being occupied, an ordering parameter was defined by the ratio of observed I_{obs} and calculated I_{calc} integrated intensity ratios of (002) and (004) reflexes. Several approaches to quantify this through either

$$D = \frac{I_{obs}(002)/I_{obs}(004)}{I_{calc}(002)/I_{calc}(004)} \quad (77)$$

by Ji et al. [92],

$$I_r = \frac{I_{obs}(002)}{I_{obs}(002) + I_{obs}(004)} \quad (78)$$

by Sugita et al. [113], or $R_I = 1/I_r$ by Takahashi et al. [88] exist.

Multiple reports demonstrate a scaling of saturation magnetization with ordering from samples with no superstructure reflex, equivalent to $D = I_r = 0$, and saturation magnetization values around or slightly higher than that of α -iron up to values of $I_r = 0.024$ with 2150 kA/m (2150 emu/cm³) or $I_r = 0.1$ with 2307 kA/m (2307 emu/cm³) [77,91,92,113]. For comparison, the data of these references has been plotted in Fig. 11. Contrary to these reports, Takahashi et al. as well as Higashikozono et al. performed similar experiments that did not lead to an increase of the magnetic moment. For their samples, it was shown that annealing also lead to the appearance of the (002) superstructure reflex with increasing intensity through prolonged annealing. However, the resulting increased ordering did not change the saturation magnetization significantly [88,97,102,117]. The reported saturation magnetization values can be roughly divided into two groups, the first with an M_s around that of α -Fe, the second with an M_s around 2300 kA/m

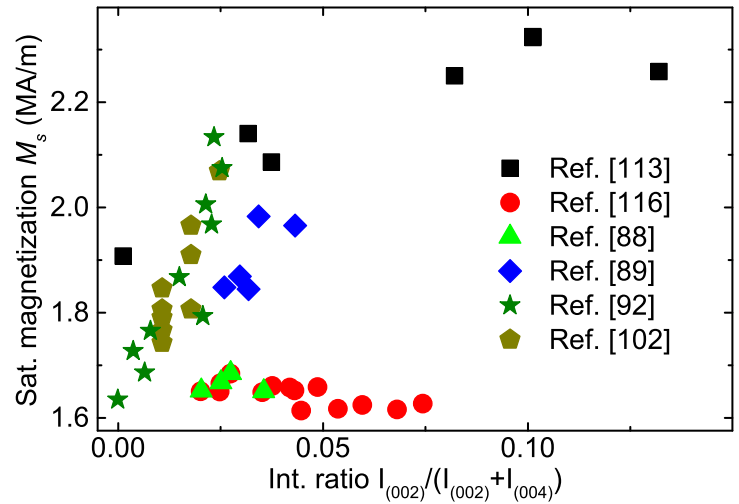


Figure 11: Saturation magnetization as a function of the ordering, estimated by the XRD intensity ratios. Data adapted from refs. [88,89,92,102,113,116].

(2300 emu/cm³).

Although, as demonstrated, many contradictory reports exist, some conclusions can be drawn. The most likely explanation for the giant magnetic moment, mostly found by Wang's group from Minnesota and Sugita's group of the Hitachi Research Laboratory, is an increase in lattice constants of their thin film samples, resulting in an increased lattice volume which in turn induces larger magnetic moments. Especially when also considering the different levels of epitaxial strain depending on the choice of substrate, the buffer layer, as well as the film and buffer layer thickness, different cell volumes and modified lattice distortions and therefore different magnetic moments are to be expected. In addition, the precise determination of the film volume and weight in order to determine the volume and mass magnetization have to be considered as a cause of error, especially since one of the most used buffer layer materials, α -Fe, is not only ferromagnetic but also shares many similarities with α'' -Fe₁₆N₂ in terms of its structure. One particular difficulty that arises due to the low intensities observed in XRD measurements is the correct evaluation of the volume fraction of α'' -Fe₁₆N₂ by integrated X-ray peak intensity ratios in the samples in order to calculate the volume fractions and from that the magnetization of the phases present in the sample. This becomes clear when looking at the reported values for the volume magnetization of bulk samples, shown in the last section of table 1. Here, even for samples with close to 100% volume fraction of unoxidised α'' -Fe₁₆N₂, the volume magnetization is close to that of α -Fe with 1710 kA/m (1710 emu/cm³) and is, with the exception of two reports, well below the magnetization of 1910 kA/m (1910 emu/cm³) for Fe₆₅Co₃₅, the material lying at the top of the Slater-Pauling curve [49, 138, 151]. This is confirmed by theoretical predictions based on state of the art LSDA+U calculations, where giant magnetic moments can only be obtained by utilizing Hubbard U parameter values far exceeding reasonable levels. Realistic U values result in magnetic moments which are larger than for α -Fe, an effect that is counteracted by the increased cell volume and thus results in a saturation magnetization similar to that of α -Fe.

4.2 MAE and PMA in α'' -Fe₁₆N₂

Although the potential existence as well as the origin of the giant moment in α'' -Fe₁₆N₂ was discussed by most reports, the occurrence of a perpendicular magnetic anisotropy as well as the magnitude and origin of the increased magnetocrystalline anisotropy was rarely investigated, even though it was observed by several groups [79, 87, 114, 123, 152]. The increase of MAE caused by a tetragonal distortion can be understood by the breaking of cubic symmetry which causes second-order anisotropy terms to appear, as discussed in section 3.3.1. Qualitatively, this effect was confirmed for α' -Fe₈N_x thin film samples with nitrogen content of $0 \leq x \leq 1$ [123, 152]. Interestingly, the reported K_1 values vary in a wide range, similar to the reported magnetization, from about 4×10^4 up to 1.6×10^6 J/m³ (4×10^5 to 1.6×10^7 erg/cm³) as evident from table 1.

Calculations for α -Fe with increasing c/a ratio indicated a complicated behaviour with the magnetic easy axis along [001] for $1 < c/a < 1.07$. With further increase of c/a beyond 1.07, the easy axis aligns along [100] until it comes close to the fcc limit, where yet another reorientation back to [001] takes place [153]. Since for α' -Fe₈N_x only one spin reorientation from [100] to [001] is observed at $x \approx 1.06$, a description based purely on the distortion of the α -Fe lattice is insufficient. Ke et al. performed quasiparticle self-consistent GW approximation (QS GW) calculations on α'' -Fe₁₆N₂ which revealed that the orbital magnetic moment is decreased for 8*h* sites and increased for 4*d* and 4*e* sites. By evaluating the atomic magnetic anisotropy energy, they find that the 8*h* site favours an easy axis lying parallel to the [100] direction. The 4*e* and, to a lesser extent, the 4*d* site contribute to this easy axis orientation which is an energetically more favourable configuration, hence aligning the magnetic easy axis parallel to the vertical axis of the iron octahedra [154]. To further investigate this effect, Zhang et al. considered variations of the locally ordered iron octahedra in a $2 \times 2 \times 2$ supercell of α -Fe. Although only two types of iron sites are taken into account, they confirm that the 4*d* orbital contribution induces a PMA for all geometries with the exception of vertically stacked iron octahedra. Interestingly, the reason for this orbital alignment is found to be the nitrogen interstitial atom. The most stable configuration with

separated octahedra has the highest MAE with about $6 \times 10^5 \text{ J/m}^3$ ($6 \times 10^6 \text{ erg/cm}^3$). The MAE is reduced by a factor of about two for the remaining geometries which are nearly equivalent in terms of their anisotropy [124]. Experimentally, a similar conclusion is drawn by Higashikozono et al., who found that through annealing, the nitrogen in their MBE grown samples improves. While this has no effect on their saturation magnetization, they observe an increased saturation field, corresponding to an increased anisotropy, after an annealing of their α' -Fe₈N samples for 20 hours [97].

This result could explain the variation of MAE observed in experiments through the restriction to low temperatures necessary to synthesize samples of α'' -Fe₁₆N₂ and/or α' -Fe₈N limit the diffusion of nitrogen in α -Fe. By applying a finite processing time, a less than perfect local ordering of nitrogen is obtained which, in turn, reduces the MAE.

4.3 Thermal stability of α'' -Fe₁₆N₂

An important property which was not discussed so far is the decomposition temperature as well as the thermal behaviour of the magnetic properties exhibited by α'' -Fe₁₆N₂. As already mentioned in the introduction to this chapter, α'' -Fe₁₆N₂ is metastable and has a low decomposition temperature. This not only limits its potential applications drastically, but also complicates the synthesis of samples. Although the decomposition, according to the phase diagram, should take place at 486 K, most reports only use either room temperature or temperatures in the range of 373 to approximately 423 K for sample synthesis, with decomposition starting at around 453 to 473 K. Below these temperatures, the saturation magnetization decreases with increasing temperature in a reversible manner [65, 66, 76, 88, 89, 145, 152, 156].

Contrary to this, Kim and Takahashi as well as Sugita et al. claim a reversible change in the magnetization up to about 576 and 676 K, respectively. While these reports seem to initially contradict each other, Widenmeyer et al. could demonstrate by differential scanning calorimetry (DSC) and in situ neutron diffraction that the decomposition temperature of α'' -Fe₁₆N₂ strongly depends on the heating rate during the experiment. By adjusting the heating rate to 10 K/min, an immediate decomposition into α -Fe and N₂ takes place at above 730 K. A decomposition into γ' -Fe₄N and, at even higher temperatures, α -Fe was observed for rates of 5 K/min and below at 486 and 583 K, respectively [157]. Although the Curie temperature of 813 K is sufficiently high for use in, e.g., electric motors or generators with temperature requirements of around 473 K, the abovementioned decomposition temperatures of α'' -Fe₁₆N₂ are already in a similar regime [158]. In addition, time dependent temperature studies revealed a long time temperature stability with a performance of 99% for 100 a to be achieved only below 355 K, as shown for different amounts of decomposed phase d in Fig. 12 [155]. At temperatures close to the reported decomposition temperature, full decomposition takes place in as little as a few minutes [65, 155, 157]. Based on these findings, the annealing process that is reported to be necessary for the formation of the ordered phase should be further investigated. By utilizing the parameters of Yamamoto et al. to calculate the amount of decomposed phase for the required annealing temperatures and times, it becomes clear that the underlying process for the decomposition and formation of the α'' - and therefore also the α' -phase are energetically close. This is illustrated by

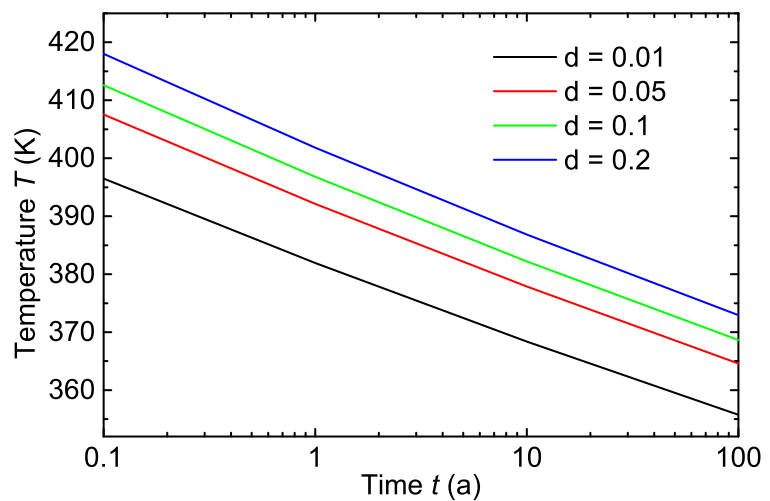


Figure 12: Temperature stability of α'' -Fe₁₆N₂ as a function of time for different fractions of phase decomposition d . Adapted from Yamamoto et al. [155].

Fig. 13, where the expected fraction of phase decomposition d is plotted for different temperatures as a function of the time according to Yamamoto et al. with indicators for reported annealing parameters utilized by different groups [77, 79, 88, 89, 91–93, 102, 104, 109, 113, 115, 117, 118, 120, 125, 127, 155, 159, 160]. Elevated annealing temperatures as for example claimed by Gao et al. (773 K, not shown in Fig. 13) and Abdellateef et al. (573 K) are expected to fully decompose the phase of interest even for considerably shorter annealing times than utilized by both groups [109, 159]. In addition, even for the majority of reported annealing temperatures of either 423 or 473 K, $d \geq 0.01$ is expected for annealing times of longer than 20 hours or 3 minutes, respectively.

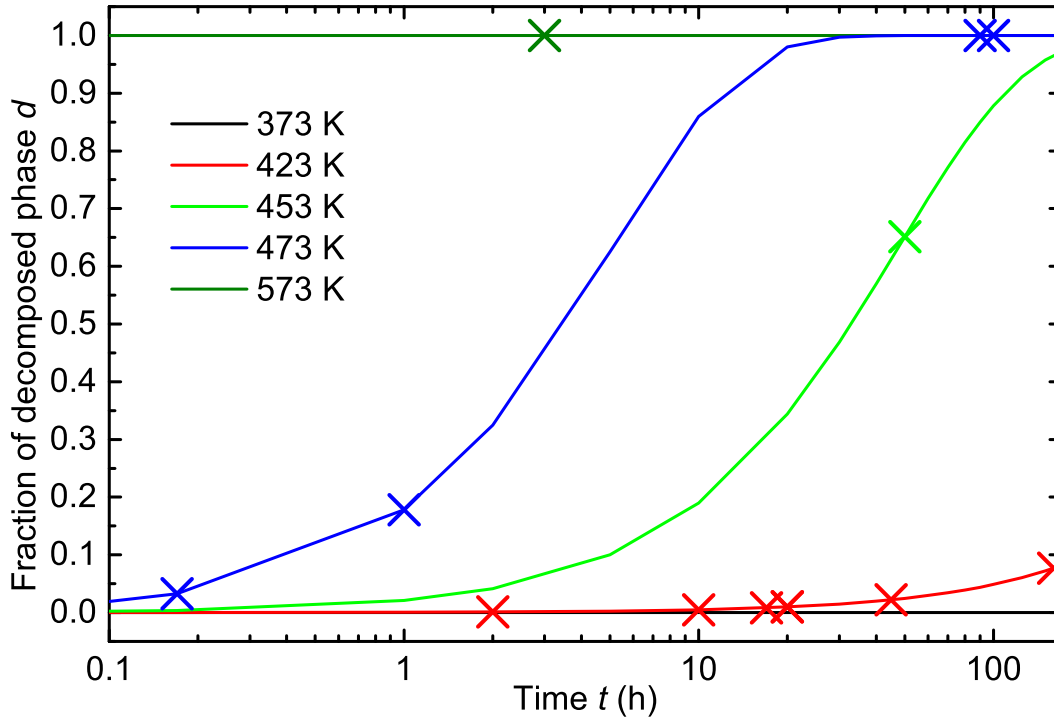


Figure 13: Fraction of α'' -Fe₁₆N₂ phase decomposition d as a function of time for different annealing times. Several experimental reports with different parameters are indicated in the respective curves [77, 79, 88, 89, 91–93, 102, 104, 109, 113, 115, 117, 118, 120, 125, 127, 159, 160]. Adapted from Yamamoto et al. [155].

Even though the reports of the investigation of the decomposition temperature described above are conclusive and give a good quantitative understanding of the decomposition, the underlying mechanisms that govern this process are not yet fully understood. As mentioned above, α'' -Fe₁₆N₂ decomposes into γ' -Fe₄N and α -Fe and, upon further (or faster) heating, into α -Fe and N₂. Jack suspected, that the metastability of the α' and α'' structures is caused by their similarity to γ' -Fe₄N and α -Fe. This is further backed by the volume per iron atom of α'' -Fe₁₆N₂ which lies, with 12.86 Å³, in between α -Fe with 11.79 Å³ and γ' -Fe₄N with 13.61 Å³ [65]. Yamamoto et al. determined the activation energy of the decomposition to be 199 kJ/mol, a value much higher than the activation energy for diffusion of nitrogen in iron nitrides of approximately 90 kJ/mol [155, 161]. This activation energy is similar to that of iron self diffusion in α -Fe with about 250 kJ/mol, a finding supported by Gupta et al. who additionally determined that nitrogen diffusion relieves the stresses in Fe-N thin films [162, 163].

A similar conclusion is drawn by Tayal et al. who found that through doping with Zr or Al, the thermal stability of iron rich iron nitrides can be improved. An estimation of the diffusivity for iron self diffusion by PNR shows a reduction of the diffusion coefficient upon introduction of Zr and Al [164]. By calculating the cohesive energy of α'' -Fe_{16-x}Z_xN₂ doped with Z = Cr, Mn, Co, or Ni and $x = 1$ or

2, Huang et al. take a different approach. Replacing two iron atoms with cobalt improves the cohesive energy dramatically from 0.067 eV, for the initial α'' -phase, to -0.417 eV compared to chromium and manganese which had a smaller but still significant impact and respective cohesive energies of -0.256 and -0.292 eV [165]. However, experimental results for cobalt doping provided by Takashi et al. suggest a different behaviour. With increasing cobalt content up to 30 at.%, the decomposition temperature of the phase was systematically reduced down to room temperature, although an increase in the saturation magnetization could be observed [116]. By supplementing 15 wt.% nickel to their powder samples, Wallace et al. observed reversible formation of the α' -phase at temperatures around 275 K instead of a moderately increased temperature stability. When manganese was added to their sample, the phase formation was fully suppressed and only a nonmagnetic γ -Fe-Mn phase was obtained [143]. However, the addition of only 3 to 10 at.% titanium leads to an increased decomposition temperature of about 1070 K as reported by Wang et al. [166].

These findings are qualitatively in good agreement with a classification of the effect that alloying elements have on the phase diagram of iron, a work which was cumulated by Bain in 1939. He states that the addition of Co, Mn, or Ni would reduce the phase space of the α -phase, therefore leading to a reduced formation temperature and stoichiometry window. Other elements, amongst which Ti can be found, have the opposite effect and reduce the formation window of the γ -phase up to effectively suppressing it [167]. It can be argued that by removing γ' -Fe₄N as the next more stable nitride phase from the phase diagram, the decomposition of α'' -Fe₁₆N₂ could be deferred. This could potentially lead to a higher solubility of nitrogen in the α' -phase, which would result in a larger tetragonal distortion, thus giving rise to a further increase in magnetic anisotropy [154]. The few existing reports in literature that deal with the alloying of α'' -Fe₁₆N₂ substantiate the claim that the formation of the iron rich iron nitrides can be influenced in accordance to the classification of Bain. Surprisingly, a systematic study based on this at least 80 year old knowledge has yet to be performed in order to finally understand and thereby tune the thermal stability as well as the magnetic properties of this family of compounds.

5 Experimental investigation of the iron nitride phase diagram

One of the main objectives of this work was the growth, characterization, and potential modification of α' -Fe₈N and optionally α'' -Fe₁₆N₂. In order to resolve the origin of the variation of magnetic moment and anisotropy reported (see table 1), a low temperature iron nitride thin film phase diagram was established to provide a solid fundamental understanding of the iron nitride system as a first step. With a nitrogen content of α' -Fe₈N and α'' -Fe₁₆N₂ of about 11 at.%, the experimental focus was set to the low nitrogen content regime of the iron nitride phase diagram. Another point that had to be considered is the low decomposition temperature of the α' - and α'' -phases below 473 K, due to which temperatures above 623 K, where the growth of the ϵ -phase would be expected according to the phase diagram, were not explored [67]. In addition, according to a report by Sugita et al., the growth of α' -Fe₈N by MBE with a reasonable crystal quality is only possible with growth rates at or below 0.1 Å/s, further restricting the parameter space [77]. While the reduction of the iron growth rate proved to be unproblematic by MBE, the least possible nitridation was limited by the operation window of the rf radical source, requiring a minimum pressure in the discharge tube to strike and maintain a stable plasma. Samples grown during preliminary experiments consisted of γ' -Fe₄N or even ϵ -Fe_xN for the lowest nitrogen flow and rf power at which the plasma in the source would not break down. For this reason, the custom made aperture and discharge tube, illustrated in appendix A were used. The target thickness for all films was 30 nm and all films could be reproduced with either e-gun or effusion cell evaporation of iron.

In the following, the evaluation of the two growth temperature regimes, below 473 K (section 5.1) and at as well as above 473 K (section 5.2) will be given. Below 473 K, the parameters for α' -Fe₈N as the phase of interest are ascertained. A detailed optimization of α' -Fe₈N growth parameters as well as a discussion of the structural and magnetic properties are omitted at this point and included in the following chapter. Based on the phases obtained at different growth temperatures and nitridation conditions, a low temperature MBE phase diagram will be presented in section 5.3.

5.1 Growth temperatures below 473 K

For this initial study, the growth temperature was chosen to be 373 K in order to allow α' -Fe₈N to stabilize and to maintain temperatures well below its decomposition. The iron deposition rate was varied in 0.02 Å/s steps from 0.04 Å/s to 0.1 Å/s while nitridation was kept constant at a flow of 0.7 standard cubic centimetres per minute (sccm) and a power of 140 W applied to the rf radical source.

The deposition was carried out onto MgO (100) substrates with $a = b = c = 4.211$ Å, MgAl₂O₄ (MAO) (100) substrates with $a = b = c = 8.083$ Å, and Al₂O₃ (0001) with $a = 4.7587$ Å and $c = 12.9929$ Å. α -Fe ($a = b = c = 2.868$ Å [168]), α' -Fe₈N, as well as α'' -Fe₁₆N₂ ($a = b = 5.718$ Å [66, 69]) are rotated by 45° in-plane with respect to MgO and MAO[100]. The resulting lattice mismatch is -3.68% and -3.95% for MgO as well as 0.5% and 0.08% for MAO, respectively [123]. γ' -Fe₄N ($a = b = c = 3.790$ Å [169]) shows no in-plane rotation with respect to MgO and MAO[100] which translates to a -10% and -6.2% lattice mismatch [123, 170]. For the growth on c-cut Al₂O₃, no literature reports could be found on the subject of the α - and α' -phases [152].

The XRD patterns of this series are displayed in Fig. 14, where the relative nitrogen content increases from top to bottom in each panel by reducing the growth rates. For iron rates at and above 0.08 Å/s, the α -Fe reflex at 64.97° as well as the α' -Fe₈N reflex at 58.64° can be observed for samples grown on MgO and MAO substrates (Fig. 14(a) and (c)). Reducing the rate results in an increasing ϵ -Fe_xN reflex while the growth of α' -Fe₈N is suppressed. An additional γ' -Fe₄N peak can only be found for samples grown at iron rates of 0.06 Å/s and below with the growth being more favourable on MgO. For all investigated growth rates, a residual amount of iron is present in samples grown on MgO and MAO, evident from the non vanishing peak. As expected, samples grown on Al₂O₃, their XRD patterns being shown in figure 14(b), favour the growth of ϵ -Fe_xN with decreasing growth rate, although the low intensity peaks indicate a poor crystallinity. Additionally, samples grown at 0.08 Å/s and above include a (011) oriented α -Fe component and no evidence for the α' -phase can be found. From the order of appearance,

it can be concluded that the hexagonal ϵ -Fe_xN is more favourable than γ' -Fe₄N at low temperatures and mostly independent of the substrates used in this study. The general behaviour is in accordance with the thermodynamic equilibrium phase diagram, where γ' -Fe₄N occupies only a narrow composition range [67,68]. However, the preferential growth of crystalline α -Fe, α' -Fe₈N, and ϵ -Fe_xN can be adjusted by the choice of substrate and the corresponding crystal symmetry [152].

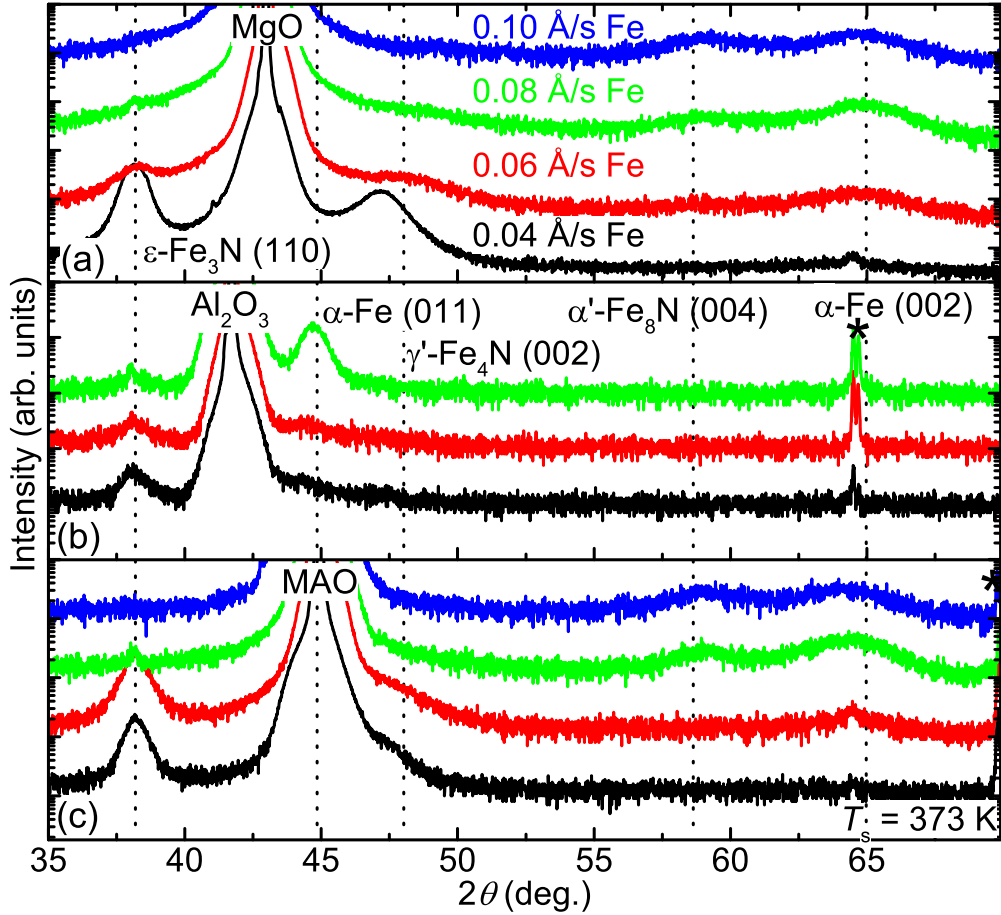


Figure 14: XRD patterns of a series of Fe-N films with increasing iron deposition rate from 0.04 Å/s to 0.1 Å/s at constant nitridation conditions onto (a) MgO (100), (b) Al₂O₃ (0001), and (c) MAO (100) substrates at a growth temperature of 373 K. The star marks a substrate peak of Al₂O₃ as well as MAO.

While Fig. 14 shows a rough scan through the phase diagram by the means of modifying the iron rate, the nitrogen content can be fine-tuned by changing the rf power applied to the radical source producing the atomic nitrogen. For this first estimation of suitable α' -Fe₈N growth parameters, the rf power was changed from 120 to 200 W in steps of 20 W at a constant nitrogen flow of 0.07 sccm. The substrate temperature was kept as in the previous study at 373 K. As shown in Fig. 15, the X-ray reflection associated with Fe₈N_x shifts towards the expected position with an increase of the rf power from 120 to 140 W, indicating the elongation of the c-axis by introduction of nitrogen interstitials as previously observed in sputtered Fe-N thin films [123]. At the same time, the peak intensity originating from the (002) α -Fe reflection decreases strongly. For samples with rf powers beyond 140 W, the peak intensity of (004) reflection of α' -Fe₈N continuously decreases. Finally, for the sample grown at an rf power of 200 W, the α' -Fe₈N reflex is lost and only a weak α -Fe reflex remains. No other Fe-N phase appeared in this narrow region of growth parameters.

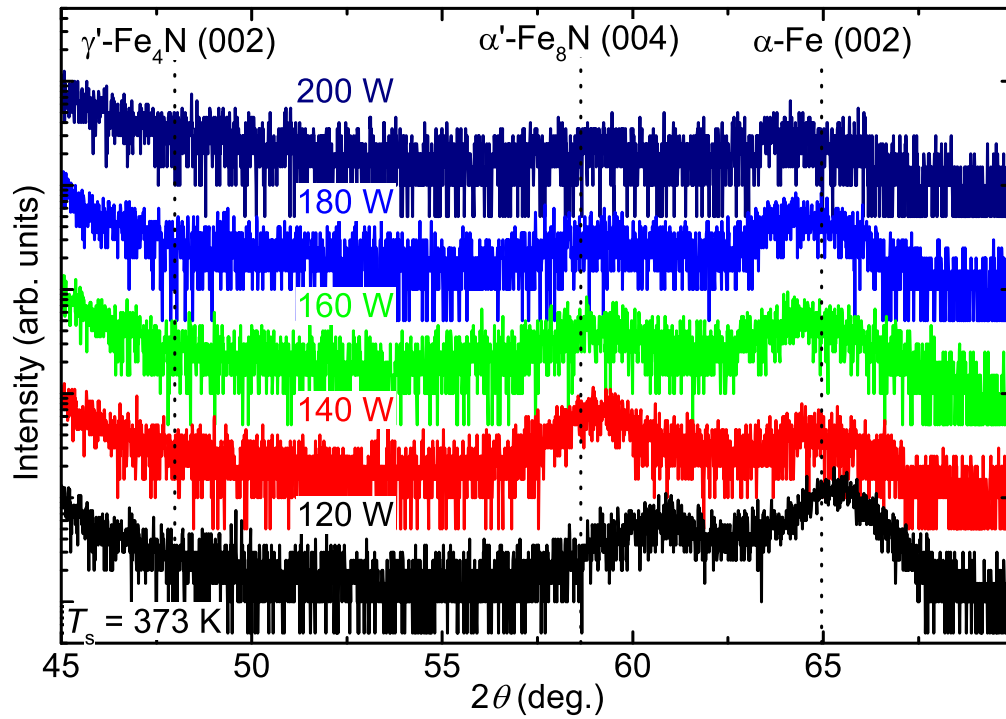


Figure 15: XRD patterns of Fe-N thin films with rf powers ranging from 120 to 200 W applied to the nitrogen radical source grown on MgO (100) at 373 K substrate temperature and a growth rate of 0.1 Å/s.

5.2 Growth temperatures of and above 473 K

In order to investigate the phase formation of γ' -Fe₄N on MgO (100) in more detail, the substrate temperature was increased to 473 and 623 K and the nitrogen flow was varied. For this temperature study, the iron rate as well as the rf power were kept constant at 0.1 Å/s and 300 W, respectively. At each temperature, the nitrogen flow was then varied from 0.02 to 0.3 sccm. As can be seen in Fig. 16, at 473 K, γ' -Fe₄N is stable over a wide range of nitrogen flow rates. Up to a flow of 0.07 sccm, the intensity of the γ' -Fe₄N (002) reflection increases continuously. Once the maximum intensity is reached, the peak starts to shift to lower angles. This indicates, that it is possible to a certain extent to expand the γ' -Fe₄N lattice in growth direction by supplying additional nitrogen which is then incorporated, for example, on interstitial positions. In-plane XRD measurements of the γ' -Fe₄N (022) reflex further corroborate these findings. As shown in Fig. 17, the *c*-axis lattice constant increases up to nitrogen flows around 0.05 sccm, where a local plateau at $c = 3.783$ Å is reached. At higher flows, the lattice constant increases monotonously up to 3.858 Å at flows of around 0.2 sccm, beyond which no further change can be observed. The inset of Fig. 17 confirms that the in-plane lattice constant *a* shrinks from initially approximately 3.816 down to 3.744 Å, which, combined with the simultaneous expansion of the lattice in *c*-direction, results in an anisotropic lattice expansion with a *c/a* ratio up to about 1.03 [152].

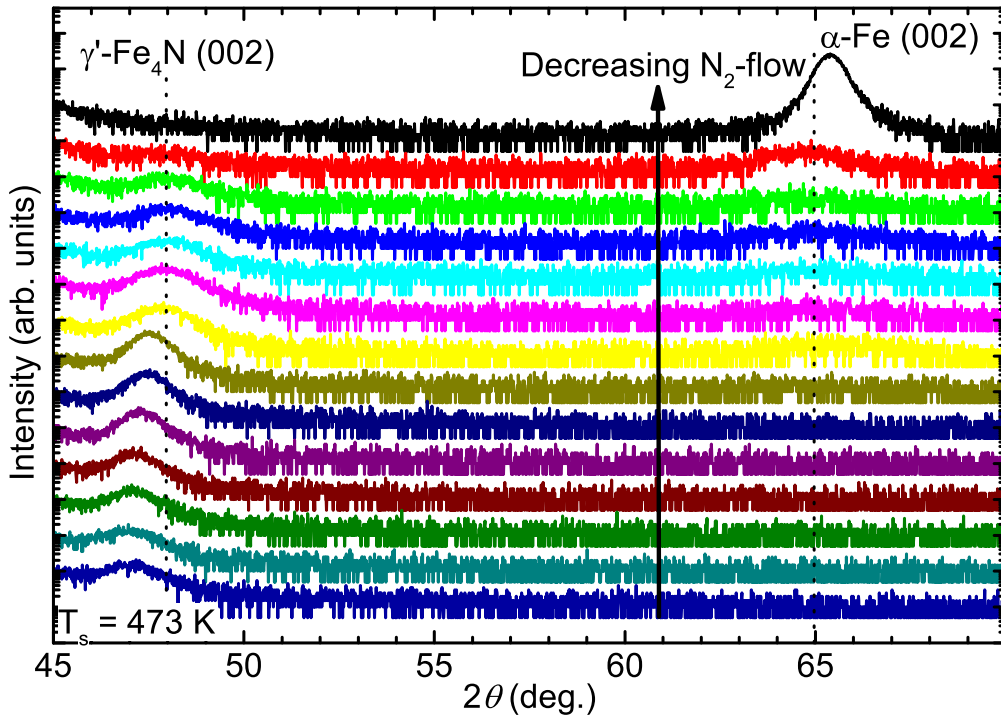


Figure 16: XRD patterns of thin films grown on MgO (100) with an increasing (from top to bottom) nitrogen flow through the radical source of 0 sccm, 0.02 to 0.10 sccm in 0.01 sccm steps, and 0.15 to 0.30 sccm in 0.05 sccm steps at a constant rf power of 300 W at 473 K.

The corresponding magnetization data of the previously discussed samples is shown in Fig. 18 where the volume saturation magnetization, M_s , is plotted against the supplied nitrogen flow. M_s drops from the pure α -Fe value to the expected saturation magnetization at a plateau for the range of nitrogen flows around 0.05 sccm which result in lattice constants close to the reported literature values for pure γ' -Fe₄N. Upon further increase of nitrogen flow, the saturation magnetization drops down to about 1000 kA/m (1000 emu/cm³) at 0.3 sccm. This could be either attributed to the effect of interstitial nitrogen in γ' -Fe₄N and/or to the formation of amorphous or randomly oriented nanocrystallites of nitrogen rich

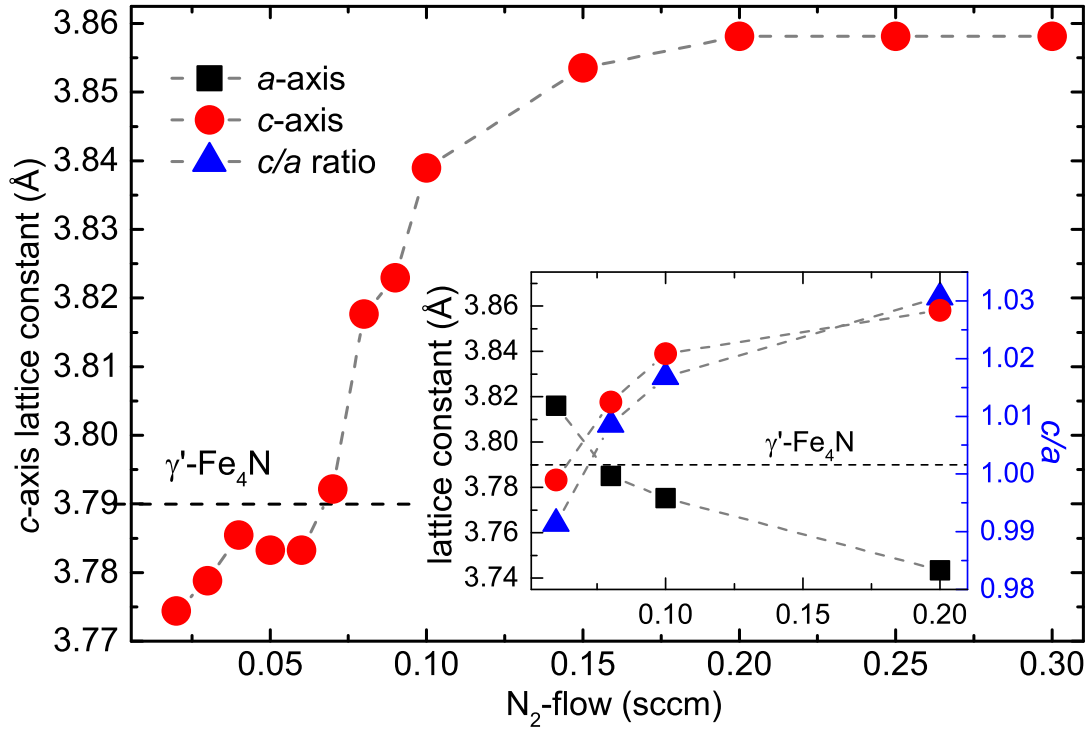


Figure 17: Evolution of the c-axis lattice constant as a function of the nitrogen flow at constant rf power of 300 W at 473 K. In the inset, in-plane (black square) and the respective out-of-plane lattice constants (red circles) as well as the c/a ratio (blue triangles) are shown.

phases such as ϵ -Fe_xN, ζ -Fe₂N, and/or FeN. The first explanation is supported by the increased lattice constant, as similarly observed for α' -Fe₈N_x. The latter explanation is supported by the continuous decrease of the density of the films as obtained from XRR, consistent with the decreasing density of Fe-N phases with higher nitrogen content. Since the lattice constants show no further change at higher flows while the density further decreases, it can be assumed that both effects occur simultaneously with a fraction of the nitrogen expanding the γ' -Fe₄N lattice while the surplus is bound in the form of nitrogen rich phases. Contrary to magnetic hardening of α' -Fe₈N_x with x nearing unity, all samples containing γ' -Fe₄N show no change in their soft magnetic behaviour, even though the lattice is distorted towards lower symmetry. This becomes obvious by comparing the half hysteresis curves of the lowest with the highest utilized nitrogen flow in the inset of Fig. 18. Although no theoretical predictions are available on the evolution of the anisotropy for distorted γ' -Fe₄N, the reduced magnetic anisotropy of fcc iron compared to its bcc allotrope implies that even in the case of γ' -Fe₄N being tetragonalised would lead to an increased magnetic anisotropy, the resulting magnetic properties would be inferior compared to α' -Fe₈N [152, 171].

The highest growth temperature utilized in this study, 623 K led to the growth of γ' -Fe₄N, as seen from the XRD patterns shown in Fig. 19. For these samples, an increase of the nitrogen flow did not cause any systematic lattice expansion, the c-axis lattice constant being stable within a deviation of approximately 0.15% (inset Fig. 19). Although no other crystalline iron nitride phases are present, the measured saturation magnetization, shown in the inset of Fig. 19, is lower than the expected 1432 kA/m (1432 emu/cm³) and decreases with increasing nitrogen flow. Similar to the samples grown at lower temperatures, this phenomenon can be explained by the formation of amorphous or nanocrystalline nitrogen rich iron nitrides. However, at elevated temperatures, γ' -Fe₄N is the most stable phase, a finding which is also supported by reports of 623 K being close to the optimum growth temperature of γ' -Fe₄N [123, 172, 173].

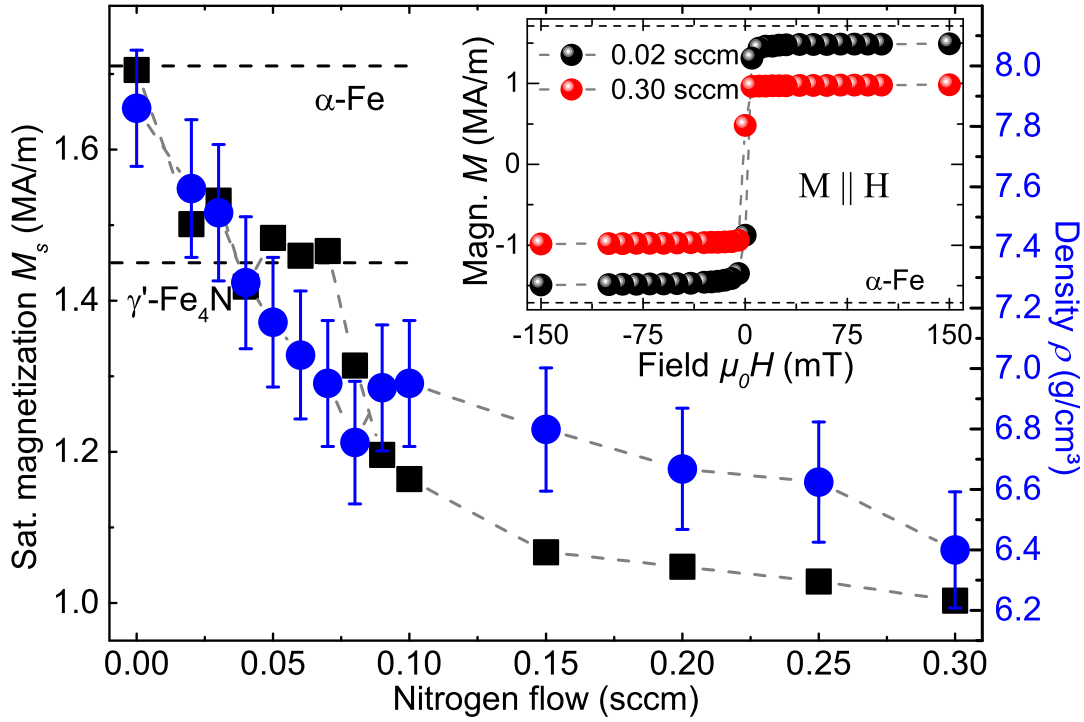


Figure 18: Saturation magnetization at 300 K and density versus nitrogen flow of samples grown at 473 K. The inset depicts a comparison between the magnetization curves for the lowest (black) and highest flow (red) utilized.

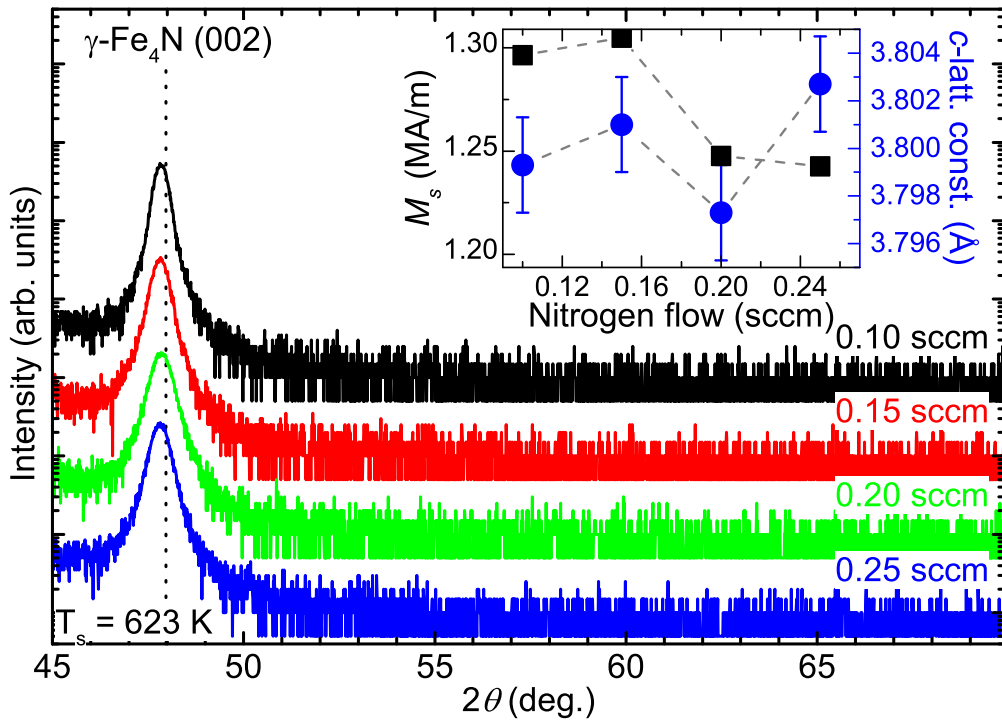


Figure 19: XRD patterns of γ' -Fe₄N thin films grown on MgO (100) at different nitridation conditions at 623 K. In the inset, the *c*-axis lattice constant (blue) and saturation magnetization M_s (black) are shown.

5.3 Low temperature MBE phase diagram

The results of the investigation of the growth of iron nitride thin films by MBE using a nitrogen radical source can be summarized in a thin film phase diagram as shown in Fig. 20. The nitrogen content was approximated by the occurrence of the corresponding iron nitride phases in the XRD patterns as well as the lattice constant of α' -Fe₈N_x. At 373 K and for low nitrogen content, a mixture of α -Fe without and with N interstitials, corresponding to α' -Fe₈N_x, is found. Here, α' -Fe₈N seems to be a fix point where also the ordered phase, α'' -Fe₁₆N₂, exists, although no evidence of it was found in the as deposited films. Beyond the corresponding nitrogen content of 11.1%, there is a coexistence region of α -Fe, α' -Fe₈N, γ' -Fe₄N, and ϵ -Fe_xN. For the samples grown at 473 K, the thin film phase diagram reproduces almost the thermodynamic equilibrium phase diagram. However, the growth window of γ' -Fe₄N at temperatures above approximately 450 K is larger than expected from the thermodynamic equilibrium phase diagram where γ' -Fe₄N occupies only a needle shaped region around its optimal nitrogen content of 20%. Phase pure samples of γ' -Fe₄N can be obtained only at further increased temperatures, e.g., at 623 K with a broader range of nitridation. For the nitrogen content exceeding roughly 20%, a coexistence of γ' -Fe₄N and ϵ -Fe_xN can be observed. In an intermediate temperature range, γ' -Fe₄N forms predominantly, mixed with residual α -Fe occurring in parallel at lower nitridation conditions [152].

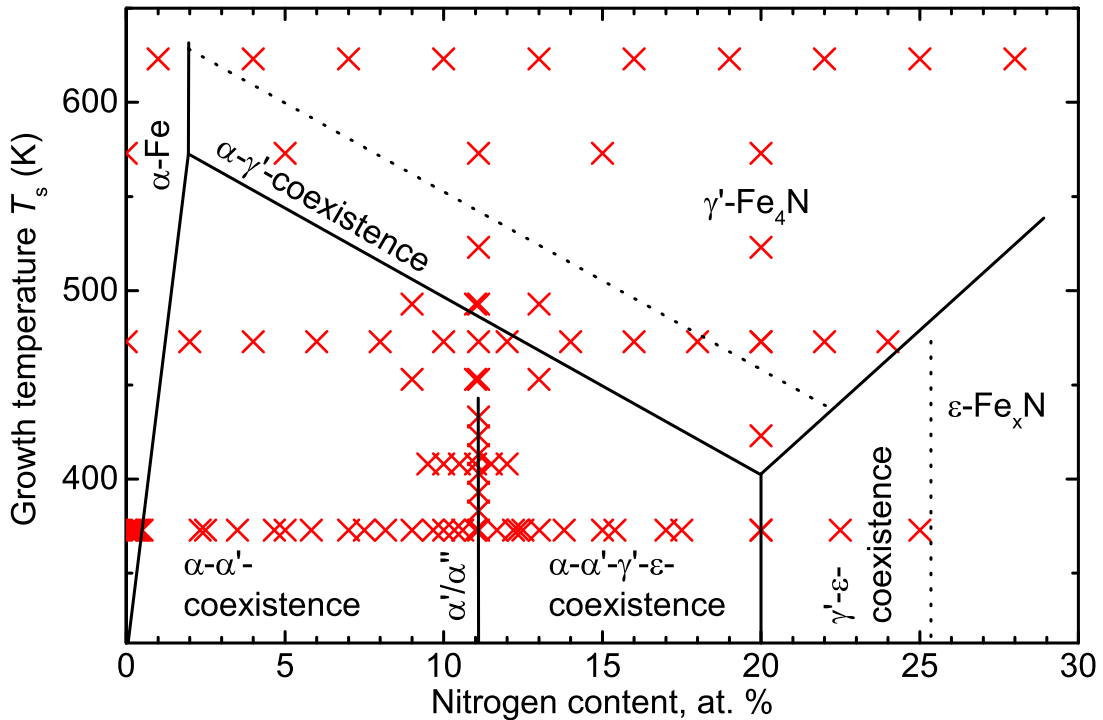


Figure 20: MBE thin film phase diagram of the iron nitride system, with the nitrogen being supplied by a nitrogen radical source. The experimental points used for this phase diagram are indicated by the crosses.

6 Growth and characterization of α' -Fe₈N

Since Dirba et al. determined that the ordered phase, α'' -Fe₁₆N₂, is not required in order to achieve high magnetic moments and an elevated magnetic anisotropy, the focus of this work lies on the disordered but otherwise equivalent α' -Fe₈N [123]. Based on the initial investigation described previously in section 5.1, a detailed analysis of the magnetic properties of α' -Fe₈N as a function of the growth conditions as well as the resulting structural properties will be given in section 6.1. In the following, a comparison of samples synthesized by both utilized thin film growth methods, MBE and sputtering, is given in section 6.2. In addition, the effect of different substrates and film thicknesses on the phase formation and the magnetic properties is described in section 6.3. Section 6.4 elucidates the decomposition temperature of α' -Fe₈N by prolonged annealing of samples in vacuum. Cobalt doping as a potential means to improve the thermal stability of α' -Fe₈N in accordance with Huang et al. was performed and is described in section 6.5 [165]. Finally, a brief discussion of the magnetic properties of α' -Fe₈N with respect to its potential use as a permanent magnet is given in section 6.6.

All samples in this study were grown with a target thickness of 30 nm and were capped with a 5 to 10 nm thick film of either Al, Ag, or Ta, with Ag and Ta employed for the MBE grown films and Al utilized solely for samples synthesized by sputtering. The thickness was chosen in order to achieve a fully closed layer which was to be thicker than the native oxide in order to prevent oxidation of the Fe-N films [174]. While Ag is diamagnetic with a volume susceptibility of χ_V of -2.38×10^{-5} , Al and Ta are paramagnetic with susceptibilities of 2.10×10^{-5} and 8.49×10^{-7} , respectively [18, 175]. However, since these susceptibilities are much smaller than that of α -Fe with 1.74×10^6 , their linear contribution could be subtracted from the SQUID M versus H measurements [18].

6.1 α' -Fe₈N formation and properties grown by MBE

As a first step, a detailed study of the formation of α' -Fe₈N as a function of growth temperature was performed on MgO (100) substrates. To fill the gaps in the previously performed study, the growth temperature was varied between 373 and 573 K at a nitrogen flow of 0.07 sccm and an rf power of 145 W. As can be seen in Fig. 22, the incorporation of nitrogen as well as the amount of residual α -Fe in the samples is strongly dependent on the growth temperature. For 373 and 393 K, the α' -Fe₈N (004) reflex is not fully shifted to the expected position and, additionally, a significant α -Fe (002) reflex can be observed. At around 413 K, the residual iron is the lowest of all samples. At higher temperatures of 433 K and above, the α' -Fe₈N reflex vanishes and the α -Fe reflex becomes more prominent. Finally, starting at 473 K, a small γ' -Fe₄N (002) reflex appears and becomes more prominent with increased temperature. This is mirrored by the saturation magnetization at 300 K (see Fig. 21) which, up to approximately 453 K, decreases continuously with growth temperature. For higher temperatures, the saturation magnetization remains mostly constant until, at 573 K, it is strongly increased, albeit with a large error. Most likely, the first temperature regime is dominated by the formation of α' -Fe₈N with diminishing amounts of α -Fe in the

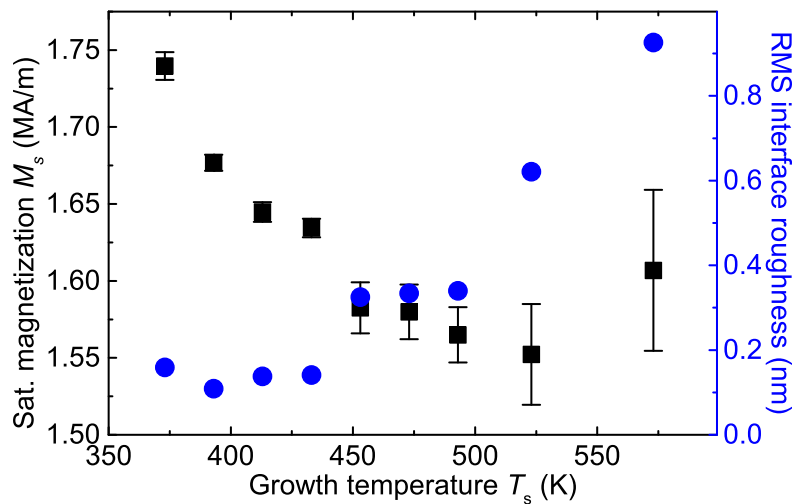


Figure 21: Evolution of $M_s(300\text{ K})$ and RMS roughness in α' -Fe₈N samples as a function of growth temperature.

samples, in addition to amorphous or nanocrystalline nitrogen rich nitrides becoming more prominent at increased temperatures. In the intermediate temperature regime, γ' -Fe₄N crystallizes while the formation of the α' -phase is impeded, which causes α -Fe to become more prominent. Finally, both α -Fe and γ' -Fe₄N crystals form in the samples grown at higher temperatures, resulting in an increasing defect density. The dramatically increasing RMS roughness that was extracted from XRR fits, represented by the second y-axis in Fig. 21, supports this explanation.

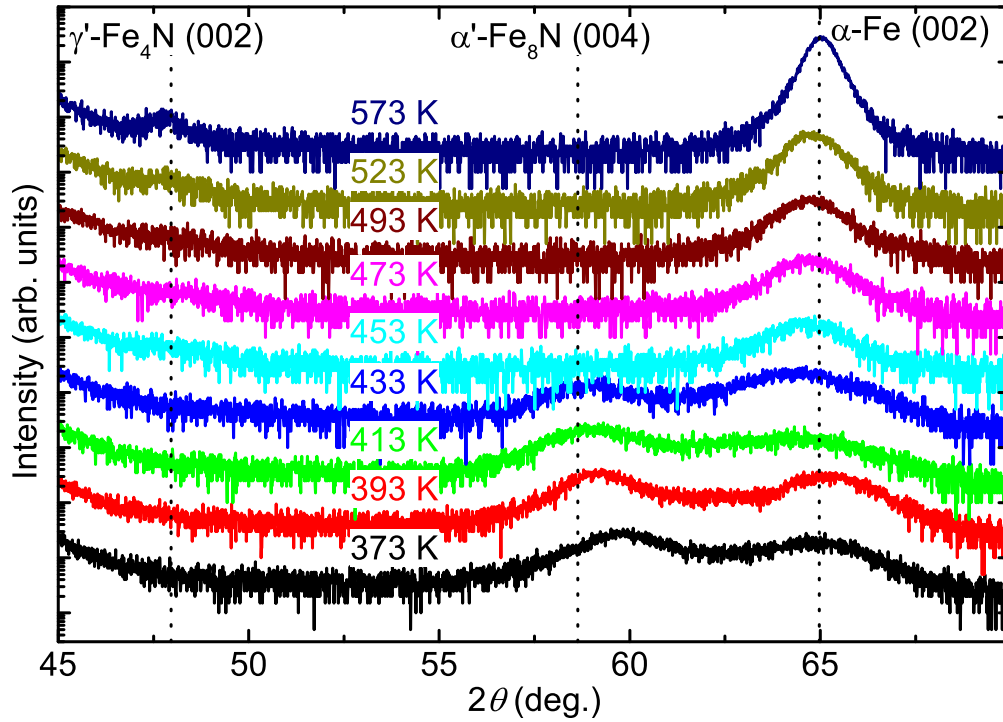


Figure 22: XRD patterns of Fe-N thin films with constant nitridation conditions grown on MgO (100) at substrate temperatures between 373 and 573 K and a growth rate of 0.1 Å/s.

The first study presented in section 5.1 showed, in accordance with the phase diagram, that only a narrow window of nitrogen concentration allows the formation of α' -Fe₈N. A fine-scan of the rf power between 125 and 150 W with an increment of 5 W was performed at a constant flow of 0.07 sccm in order to find the optimal nitridation conditions. The XRD patterns of the corresponding samples are shown in Fig. 24. For rf powers up to 140 W, the α' -Fe₈N (004) reflex shifts to lower angles until finally coming close to the expected value, thus connoting a tetragonal distortion. In addition to the peak shift, a residual amount of α -Fe, as indicated by a low intensity (002) reflex around 65°, can be found in all samples. Further increase of the nitrogen content results in a reduced peak intensity. Additionally, a ϕ -scan of α' -Fe₈N (022) and MgO (022) of the sample grown at 140 W (Fig. 23) reveals the relative growth orientation with α' -Fe₈N [110] || MgO[100]. As a result,

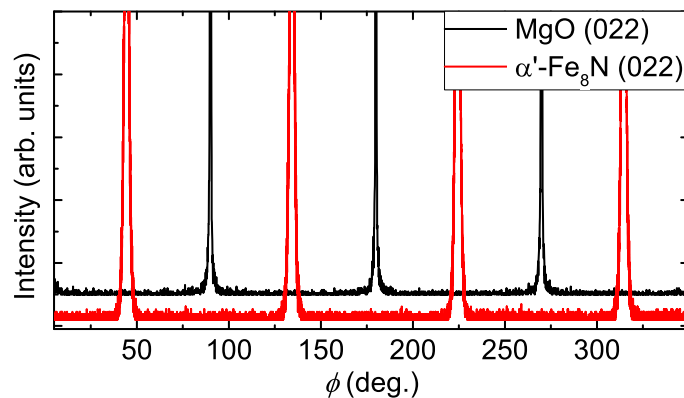


Figure 23: ϕ -scan of α' -Fe₈N (022) with respect to MgO (022).

the lattice mismatch to MgO increases from the starting material α -Fe with -3.68% up to -5.58% for stoichiometric α' -Fe₈N.

During the sample preparation, the growth was in-situ monitored via RHEED with an acceleration voltage of 30 kV in order to identify the growth mode as well as to get an insight on the evolution of the in-plane lattice constant of α' -Fe₈N. RHEED pictures were extracted in 10 Å intervals of film thickness as monitored by the QCM of the iron source. As can be seen from the sample grown with an rf power of 145 W of the series displayed in Fig. 24 with its RHEED patterns shown from Fig. 25(a) to 25(f), the initial growth mode is layer-by-layer growth with sharp streaks up to thicknesses of approximately 20 Å. The broadening of the streaks and general loss of intensity from thicknesses of 40 Å and above indicates an increased defect density and/or reduced crystal quality and therefore a relaxation of the film, although the growth mode remains the same. Interestingly, at thicknesses beyond 200 Å, an additional pattern becomes visible. Although the intensity of the pattern is comparable or even higher than the streak pattern, no additional XRD peaks could be found at this time. Later, this pattern could be attributed to the growth of (011) out-of-plane oriented α -Fe, an effect that was observed for both, nitrogen and boron incorporation and is discussed in further detail in the appendix, section B.

Due to the camera having a resolution of 640×480 pixels in this RHEED setup, one pixel at 30 kV corresponds to 0.06 Å, thereby representing the minimum observable change in the lattice. It is expected that the in-plane lattice changes from α -Fe with $a = b = 2.868$ Å to α' -Fe₈N with $a/2 = b/2 = 2.859$ Å, with a difference of 0.009 Å that is much smaller than the aforementioned resolution [69]. In addition, the diffuse nature of the streaks results in further inaccuracies amounting to approximately 0.2 Å, due to which a reasonable estimation of the in-plane lattice constants by RHEED was found to be not feasible.

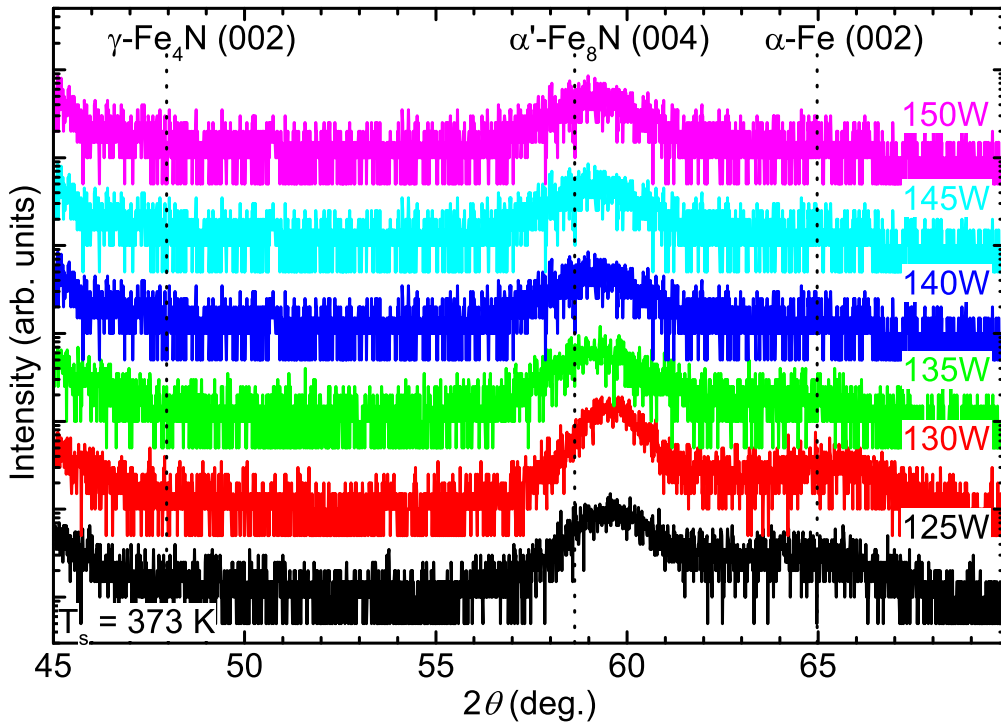


Figure 24: XRD patterns of Fe-N thin films with rf powers ranging from 125 to 150 W applied to the nitrogen radical source grown on MgO (100) at 373 K substrate temperature and a growth rate of 0.1 Å/s [152].

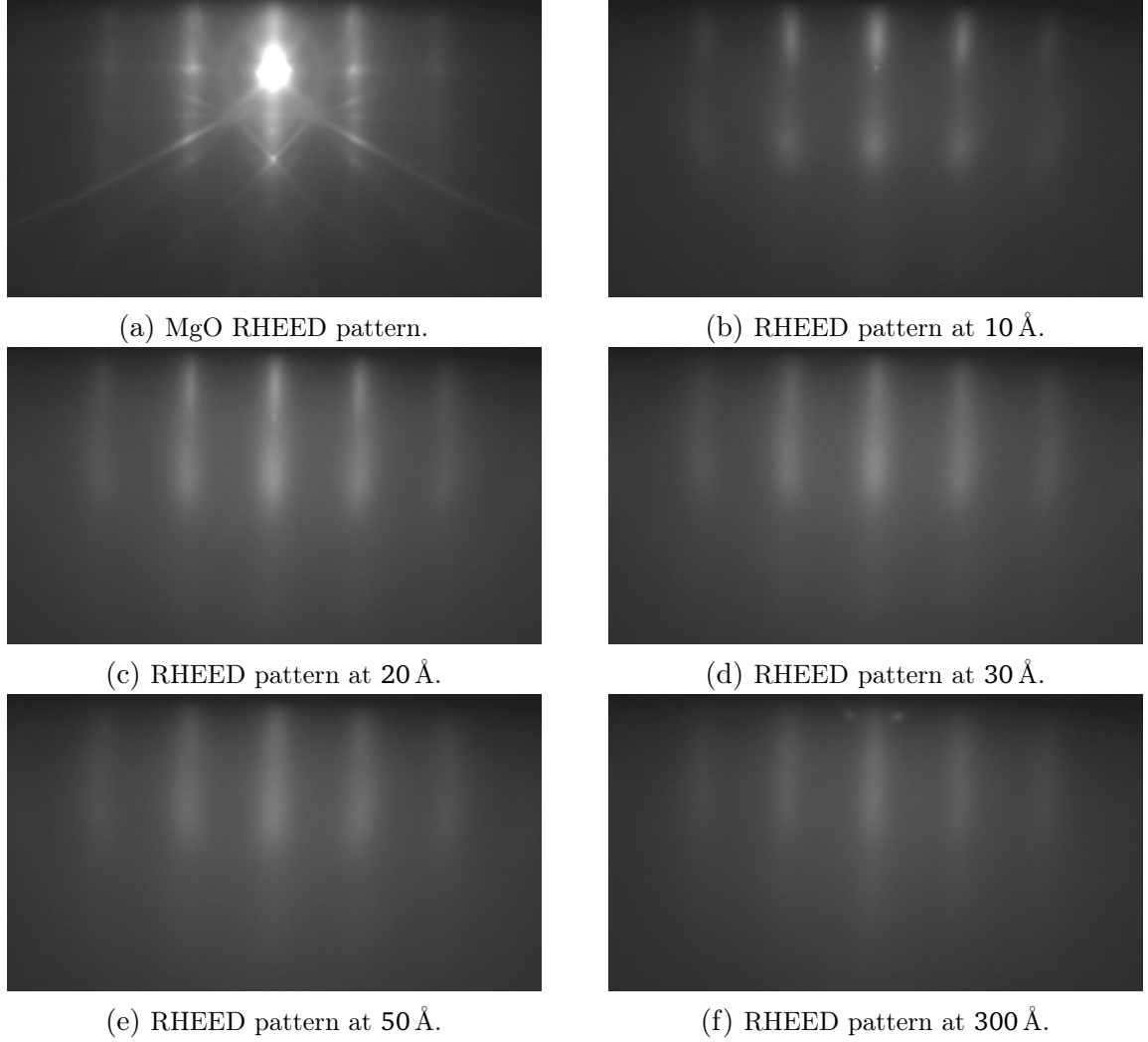


Figure 25: RHEED patterns of α' -Fe₈N grown with a rate of 0.1 Å/s and an rf power of 145 W for increasing film thicknesses. The electron beam is parallel to the (100) orientation of MgO.

Through the tetragonal distortion, the magnetic hard axis of α -Fe tilts into the film plane and an increase of the magnetic anisotropy occurs and becomes more prominent with increasing c/a ratio. The magnetic anisotropy of the films (see Fig. 26) increased from about $K_1 = 2.9 \times 10^4 \text{ J/m}^3$ ($2.9 \times 10^5 \text{ erg/cm}^3$) for the lowest rf power to a maximum of about $1.19 \times 10^5 \text{ J/m}^3$ ($1.19 \times 10^6 \text{ erg/cm}^3$) for the sample synthesized at 145 W of rf power. This value lies within the reported range of 4.8×10^4 to $1.6 \times 10^6 \text{ J/m}^3$ (4.8×10^5 to $1.6 \times 10^7 \text{ erg/cm}^3$), despite the first two samples exhibiting K_1 values lower than that of α -iron [77, 111]. As opposed to the magnetic anisotropy, the volume saturation magnetization at room temperature shows, except for one sample, a continuously decreasing trend, ultimately resulting in a lower magnetization value as compared to α -Fe. Here, the increase in absolute magnetic moment is counteracted by the increased volume of the unit cell in α' -Fe₈N_x, a trend which will be discussed in more detail in the following section. The inset of Fig. 26 shows in-plane and out-of-plane volume magnetization as a function of applied magnetic field for a sample grown with 150 W rf power. In-plane data identifies clearly the hard axis of the grown α' -Fe₈N_x, whereas out-of-plane data denotes to a shape anisotropy field of around 2 T (20 kOe). A pure α -Fe sample (without nitrogen) exhibits an M_s of 1702 kA/m (1702 emu/cm³) and a K_1 of $4.1 \times 10^4 \text{ J/m}^3$ ($4.1 \times 10^5 \text{ erg/cm}^3$), which is in reasonable agreement with the known literature values [152].

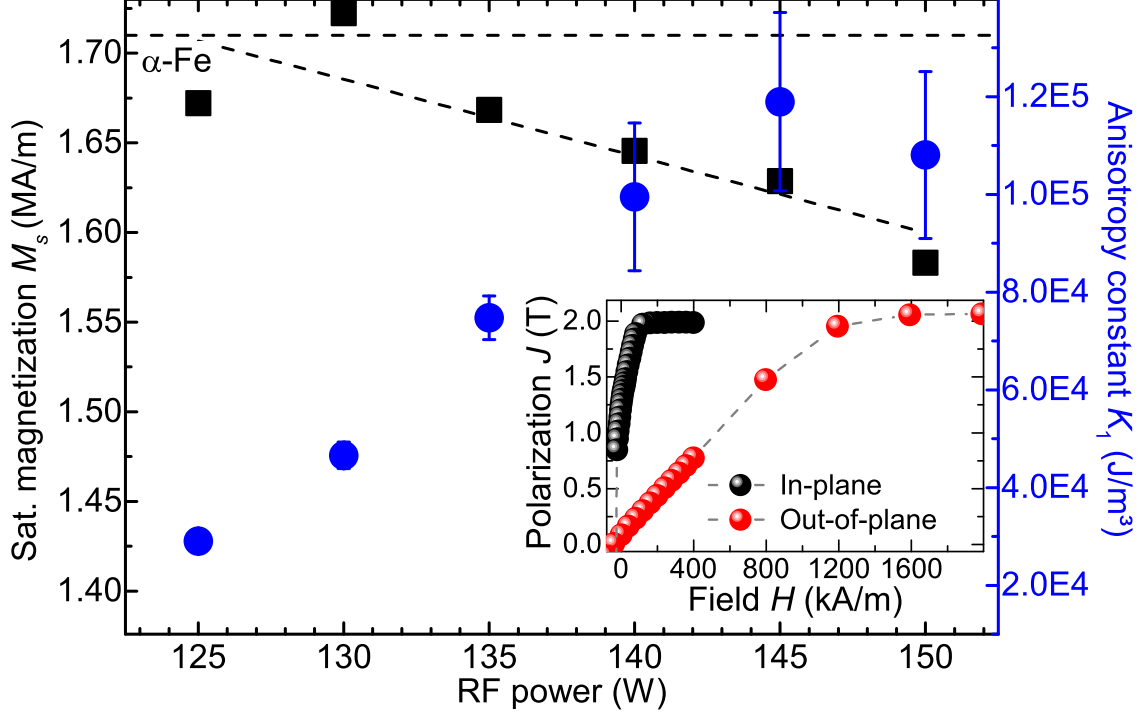


Figure 26: Saturation magnetization $M_s(300\text{ K})$ (squares) and anisotropy constant K_1 (circles) of α' - Fe_8N_x as a function of the rf power applied to the nitrogen radical source. The inset shows the M_V - H -curves of the sample grown with 150 W rf power.

Since the Curie temperature of α'' - Fe_{16}N_2 and α' - Fe_8N is higher than the decomposition temperature, only few attempts to estimate it were performed. Sugita et al. estimated the T_C of their α'' - Fe_{16}N_2 containing thin film samples around 813 K [77]. In comparison, Dirba et al. synthesized nearly phase pure α'' - Fe_{16}N_2 nanoparticles which exhibited a lower T_C of 634 K, an effect that was attributed to either surface effects of the nanoparticles or an overestimated T_C of Sugita et al. due to their mean-field based fit [138]. While the temperature range available in the utilized MPMS is limited to an upper temperature of 350 K, an attempt to fit the data in a meaningful manner was made. Initially, a bare MgO substrate was measured with the same conditions as the α -Fe and α' - Fe_8N samples that were investigated. This step was necessary in order to eliminate or at least reduce the contribution of the paramagnetic impurities, for example Mg surface defects, within the MgO substrates since they become significant at low temperatures [176]. After subtracting the substrate effect of the measurement, the corrected data was fitted to the equation

$$M_s(T) = M_s(0\text{K}) \left[1 - s \left(\frac{T}{T_C} \right)^{3/2} - (1-s) \left(\frac{T}{T_C} \right)^p \right]^{1/3} \quad (79)$$

with $p > 3/2$ and $5/2 > s > 0$ which was proposed by Kuz'min [177]. The fitting parameter p is empirical while

$$s \approx 0.176 \frac{\mu_B}{M_0} \left(\frac{k_B T_C}{D} \right)^{3/2} \quad (80)$$

depends on the spin-wave stiffness D , the 0 K magnetization, and the T_C [177]. The resulting corrected data as well as the fits are displayed in Fig. 27. A reasonable overall conformity can be achieved, although the measurement deviates from the fit for temperatures below approximately 70 K, an effect that is most

likely caused by the paramagnetic nature of the Ta capping layer utilized for this study. Due to this effect, a meaningful 0 K saturation magnetization value could not be extracted from the fits. Despite these challenges and a consequential large error, the fitted Curie temperature for α -Fe is (1056 ± 56) K which lies in good agreement with the literature value of 1044 K [49]. The fitting parameters $s = 0.43 \pm 0.03$ and $p = 3.18 \pm 0.44$ are, with the expected inaccuracy caused by fitting only a fraction of the whole temperature range between 0 K and the Curie temperature, comparable to Kuz'min's findings of 0.35 and 4 for s and p , respectively, thereby confirming the viability of the procedure. Accordingly, the spin wave stiffness $D = (271 \pm 27) \text{ meV}\text{\AA}^2$ lies close to the reported value of $(307 \pm 15) \text{ meV}\text{\AA}^2$ [178]. α' -Fe₈N is found to have a T_C of (770 ± 73) K, a larger value than the reported T_C of Dirba et al.. However, the general trend for an increased T_C as a function of decreasing interstitial nitrogen content points towards a higher Curie temperature than that of γ' -Fe₄N with 767 K [63, 179]. Compared to α -Fe, the s parameter of α' -Fe₈N is found to be significantly larger with 0.5 ± 0.1 which, in combination with the lower T_C , results in a reduced spin wave stiffness of $(180 \pm 41) \text{ meV}\text{\AA}^2$, much higher than the reported $70 \text{ meV}\text{\AA}^2$ [99]. More precise values for T_C and s require a larger temperature range to be measured in addition to utilizing a diamagnetic capping layer like silver. Measuring the M against T behaviour of each substrate in the SQUID prior to the film deposition could further improve the measurement, evident from the varying magnetic responses that were obtained from substrates which originated from the same single crystal and production batch.

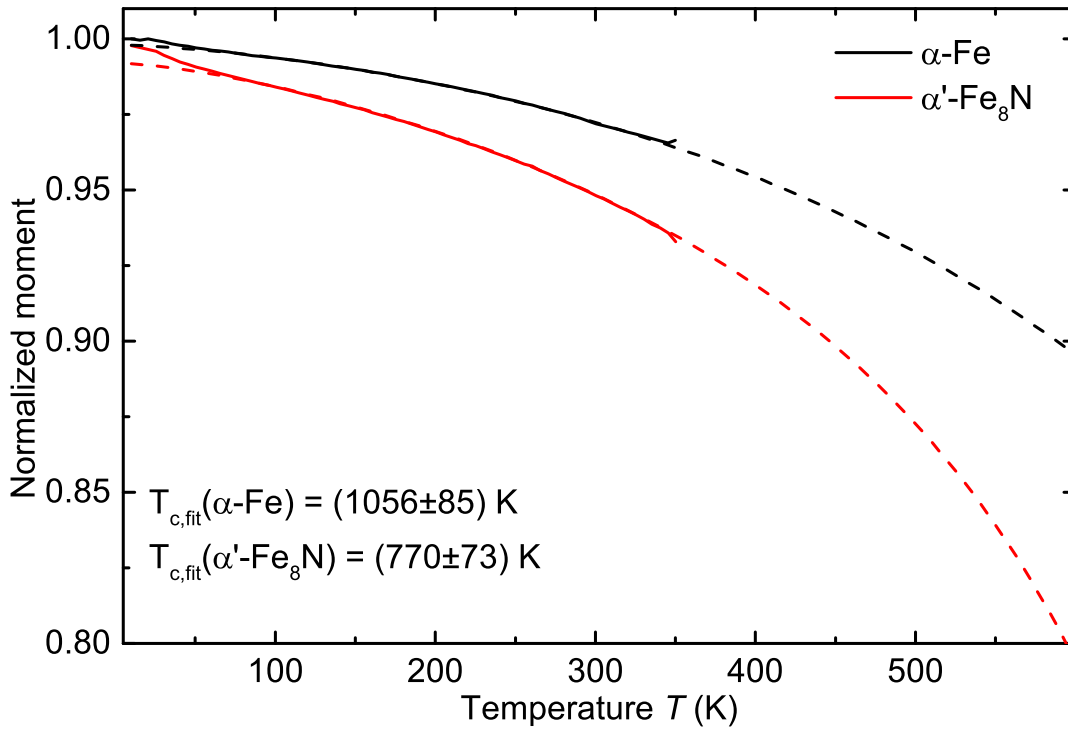


Figure 27: Magnetization versus temperature measurements from 10 to 350 K for α -Fe and α' -Fe₈N. The displayed Curie temperatures were extracted by fitting the curves from 100 to 350 K.

6.2 α' -Fe₈N growth via sputtering

A set of films was synthesized by rf magnetron sputtering in the unit described in section 2.3 in addition to the previous studies which were exclusively performed on MBE grown samples. In general, MBE allows for lower rates, smoother interfaces, and a more uniform growth through the feedback available via in-situ growth monitoring. However, when using sputtering, the kinetics of film growth can be adjusted by the pressure of the sputtering gas in the chamber. In this specific case, sputtering allowed for a continuous study starting from pure α -Fe up to α' -Fe₈N, a series which could not be performed with MBE due to the limits imposed by the operation window of the rf radical source.

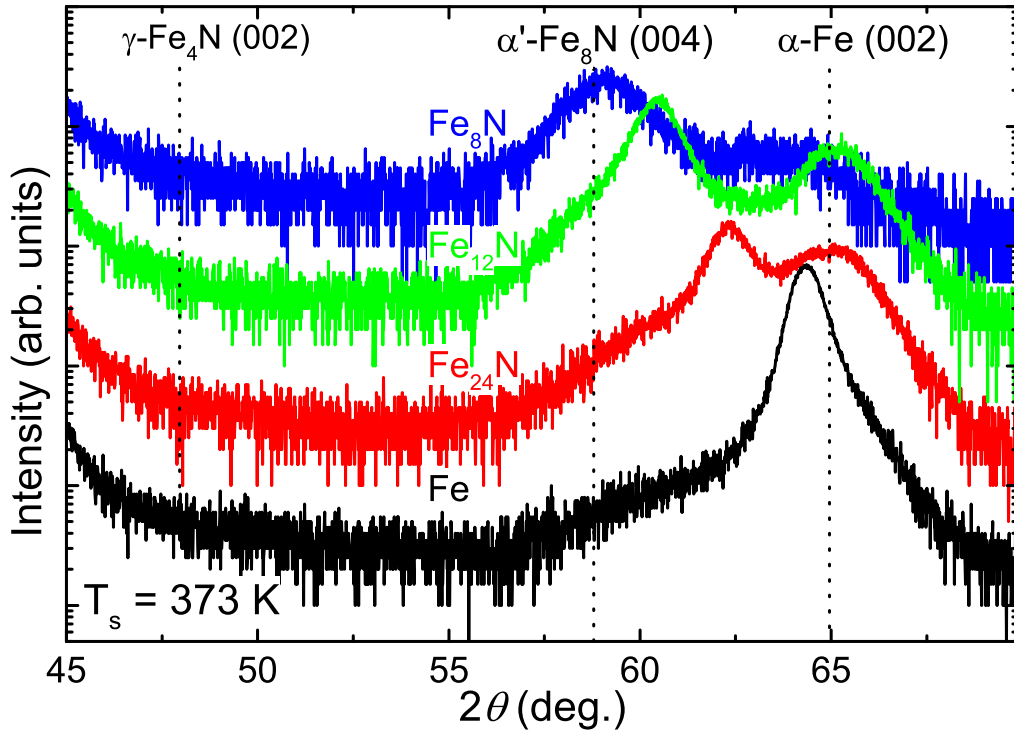


Figure 28: XRD patterns of samples grown on MgO (100) by rf magnetron sputtering with a background pressure of 5 Pa (0.05 mbar), a total flow into the chamber of 4 sccm, 373 K growth temperature, 5.5 cm substrate to target distance, and 100 W rf power.

After a brief optimization, the growth conditions were set to a background pressure of 5 Pa (0.05 mbar) with a total flow into the chamber of 4 sccm, 373 K growth temperature, 5.5 cm substrate to target distance, and 100 W rf power. The nitridation was carried out via introduction of a 90 : 10 ratio Ar to N₂ gas from Air Liquide S.A. with a purity of 99.999% by adjusting the flow ratio of pure Ar to the Ar:N₂ mixture from 4 : 0 to 0.3 : 3.7 sccm in 0.1 sccm steps. The XRD patterns of the resulting samples, shown in Fig. 28, confirm a linear evolution of the peak position to lower angles. Although, similar to the samples grown by MBE, residual α -Fe is present in the samples, its formation could be strongly modified by varying the background pressure in the chamber. In contrast, the temperature only had a minor influence on the phase formation. This is to be expected, since the formation of α' -Fe₈N is strongly limited by its low decomposition temperature, which results in a narrow thermodynamic window. The growth kinetics, however, are not impeded, thus offering a parameter which can be tuned in a wide range.

The anisotropy constant K_1 , derived from the anisotropy field H_a according to equation 69, as well as the saturation magnetization as a function of the c -axis lattice constant for sputtered and MBE grown samples are shown in Fig. 29. It can be seen that the sputtered samples exhibit a significantly higher anisotropy of $2.05 \times 10^5 \text{ J/m}^3$ ($2.05 \times 10^6 \text{ erg/cm}^3$) compared to $1.19 \times 10^5 \text{ J/m}^3$ ($1.19 \times 10^4 \text{ erg/cm}^3$) for MBE grown films with the whole curve being shifted to lower lattice constant values by approximately 0.05 \AA . Interestingly, the saturation magnetization of samples grown by both techniques lie in close proximity to each other, indicating that the phase formation during growth is similar for both techniques, albeit with a different local ordering being achieved during sputtering. However, the sputtered α' -Fe₈N film exhibits an RMS interface roughness of 2.1 nm , one order of magnitude higher compared to a roughness of 0.15 nm for a similar sample synthesized by MBE, evident from the XRR (Fig. 30). Here, the MBE grown film shows clear oscillations beyond 2θ values of 8° .

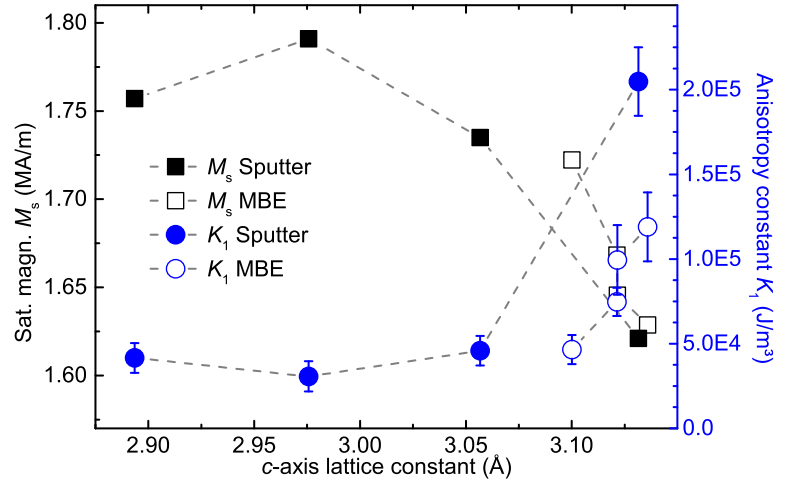


Figure 29: Comparison of M_s (squares) and K_1 (circles) at 300 K for sputtered (filled symbols) and MBE grown (open symbols) samples.

The increased roughness was most likely caused by Ar bombardment of the growing film due to the small substrate to target distance which resulted in the sample being immersed in the plasma discharge. This was necessary to achieve a sufficiently high iron rate for the proper Fe:N ratio. The evolution of the magnetic moment as well as the density of the films which was derived from fitted XRR curves are displayed as a function of the c -axis lattice constant in Fig. 31. In accordance to Vegard's law [180], the c -axis lattice constant elongates as a linear function of the nitrogen flow, evident from the inset in Fig. 31, while the density decreases simultaneously. Similar to the results obtained by Dirba et al., the magnetic moment increases continuously from (2.28 ± 0.07) to $(2.47 \pm 0.07)\mu_B/\text{Fe}$ with the c -axis elongation [123]. At the same time, the in-plane lattice constant shrinks from 2.864 to 2.811 \AA with both, the α -Fe and the α' -Fe₈N lattice constant, being slightly smaller than the reported values of 2.868 and 2.839 \AA , respectively [69, 168]. While a deviation of thin film lattice constants compared to the bulk values is expected, it is surprising that the negatively mismatched films exhibit smaller lattice constants. Since only the relative crystallographic orientation of the film to the substrate are known from ϕ -scans, the precise atomic arrangement

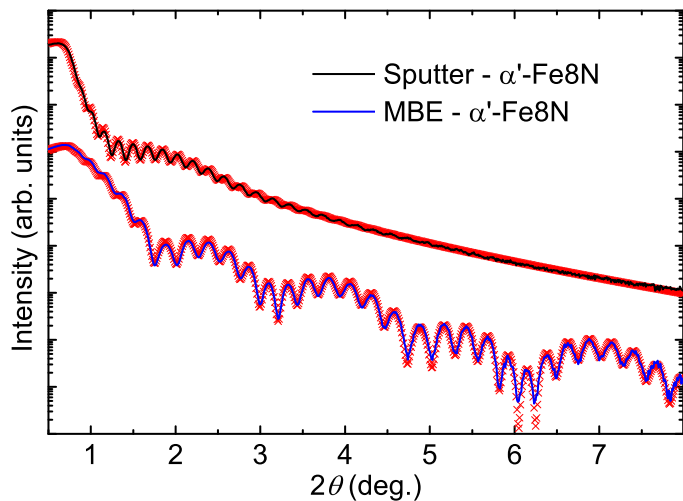


Figure 30: XRR measurements (straight lines) and fitted curves (crosses) for two α' -Fe₈N samples; one grown by MBE and one grown by sputtering.

at the interface would require further study with, for example, high resolution TEM in order to resolve the reason for the diminished lattice constants.

In order to confirm the evolution of the magnetic moments and get further insight on the orbital and spin contribution, X-ray magnetic circular dichroism (XMCD) with self-absorption correction was performed at ANKA by Yu-Chun Chen from MPI IS Stuttgart. To eliminate a potential effect of a heavy capping layer material on the measurement, the films were capped with 3 nm thin aluminium instead of tantalum. Additionally, DFT calculations of the orbital and spin contributions of α -Fe and α' -Fe₈N were carried out by Hongbin Zhang from TU Darmstadt for comparison. Fig. 32 shows the total magnetic moment obtained from these different methods. The data derived from SQUID measurements at 300 K agrees well with the presently preliminary XMCD values measured at 10 K, even though a higher moment is expected for the lower measurement temperature. This deviation is most likely due to the error resulting from the thickness and density fitting of the XRR data. In comparison, the magnetic moments calculated by DFT are lower than expected for α' -Fe₈N. During the studies encompassed in this work, no evidence of an extraordinarily large ‘giant’ magnetic moment was found [71].

Unfortunately, the ratio of orbital to spin moment m_l/m_s for all samples, shown in the inset of Fig. 32, is around 0.09 and mostly constant over the whole range of nitrogen content. For reasons unknown so far, this is several times higher than the reported values for the case of α -Fe which has an m_l/m_s of 0.043 for 5 to 7 nm thin films [181]. Only in iron clusters containing 2 to 9 atoms, an increase to 0.08 – 0.22 was observed [182].

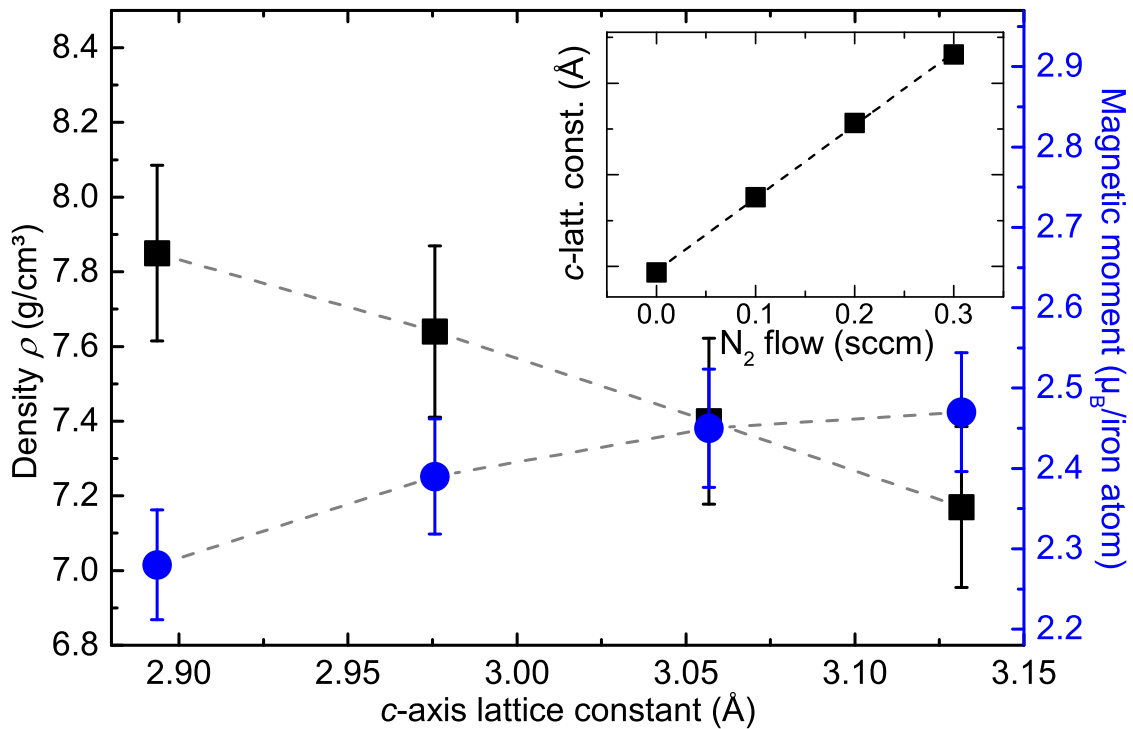


Figure 31: Density (black) and magnetic moment (blue) of sputter grown α' -Fe₈N_x films as a function of the c-axis lattice constant. The inset depicts the evolution of the c-axis as a function of nitrogen flow with a linear fit through the data points.

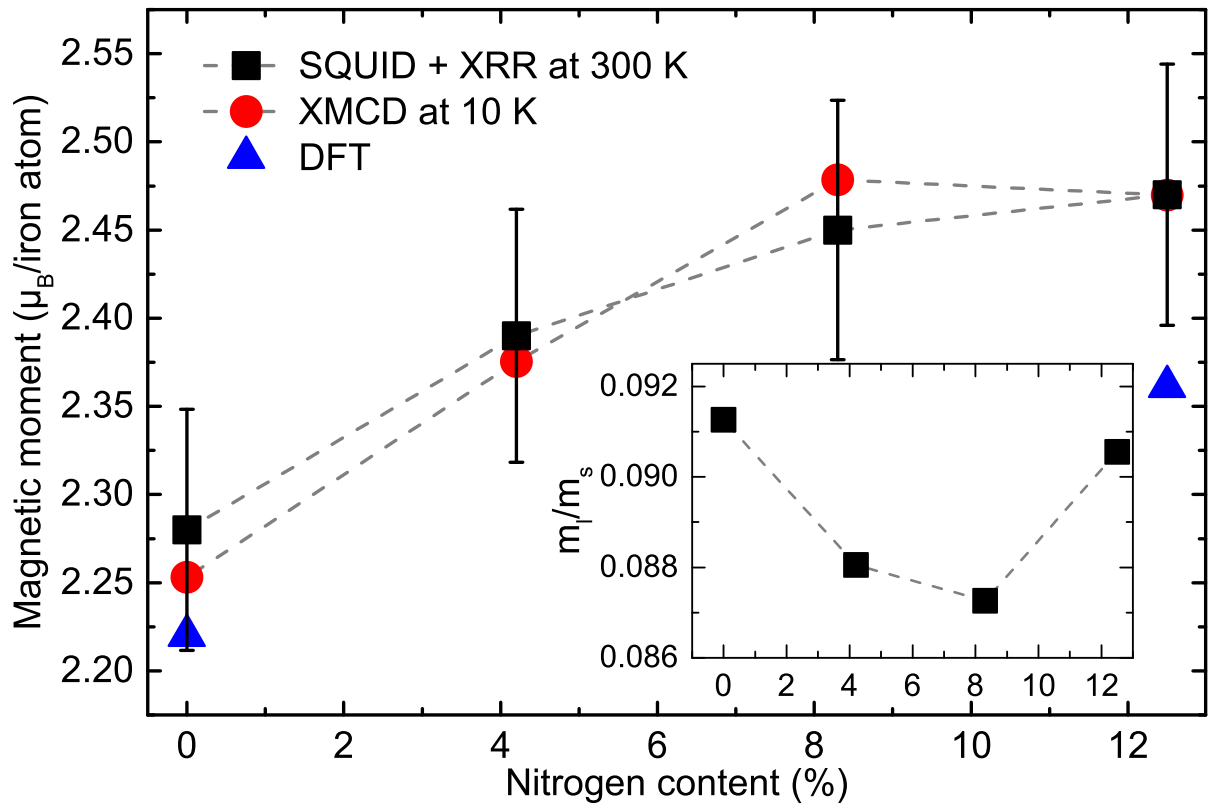


Figure 32: Magnetic moment determined by SQUID (black) and XMCD (red) measurements at 300 and 10 K of sputter grown α' -Fe₈N_x films, respectively, as well as DFT calculations (blue) as a function of the nitrogen content. The inset shows the evolution of the ratio of orbital to spin moment, m_l/m_s .

6.3 Thickness study of α' -Fe₈N on MgO, MAO, and STO

To determine the role of interface effects on the structural and magnetic properties of α' -Fe₈N, MgO, MAO, and SrTiO₃ (STO) substrates were used with a growth temperature of 403 K, an iron rate of 0.1 Å/s, and nitridation parameters of 0.07 sccm and 140 W. With α' -Fe₈N expected to grow 45° rotated with respect to these three substrates, the in-plane lattice mismatch corresponds to -3.95 , 0.08 , and 3.58 %. In addition, samples with three thicknesses of around 30, 50, and 70 nm were grown, as shown in Fig. 33. To ensure identical growth conditions between the different substrates, all samples of the same thickness were synthesized in the same deposition. Interestingly, although the mismatch of STO is similar to that of MgO, albeit with reversed sign, α' -Fe₈N could not be observed in the samples. When comparing MgO and MAO, the samples have a matching ratio of α -Fe to α' -Fe₈N with higher average X-ray intensities for MAO grown samples, indicating a better crystal growth taking place with a better matched underlayer.

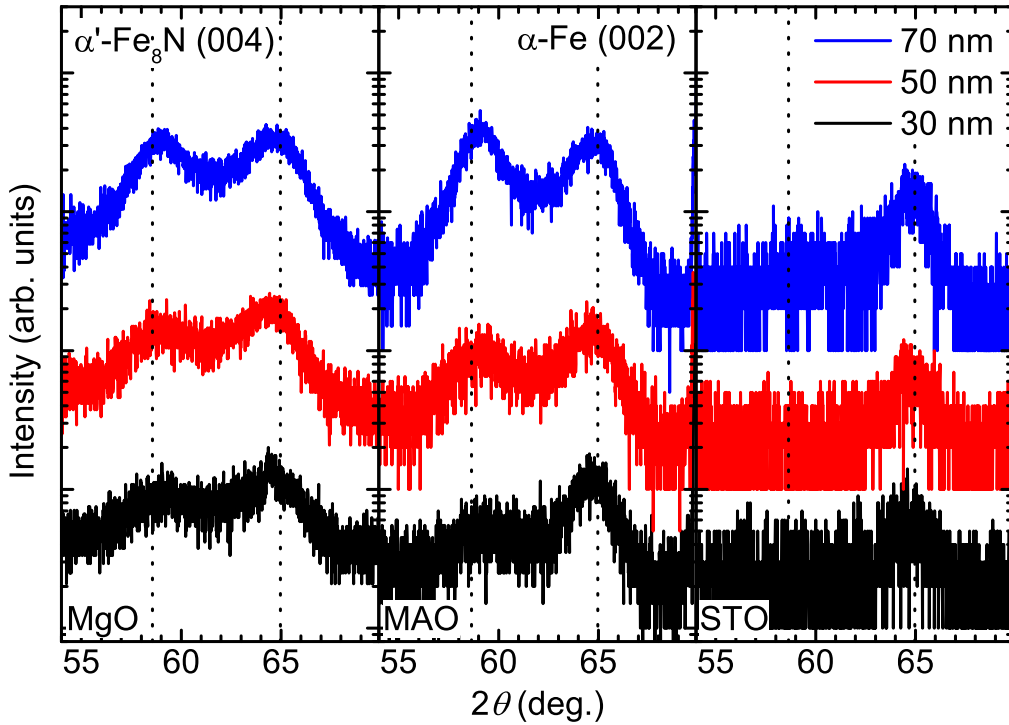


Figure 33: Influence of different substrates with -3.95 % (MgO, left graph), 0.08 % (MAO, centre graph), and 3.58 % (STO, right graph) mismatch on the XRD patterns of 30, 50, and 70 nm thick α' -Fe₈N films grown at 408 K with 140 W rf power, a nitrogen flow of 0.07 sccm and an iron growth rate of 0.1 Å/s.

The SQUID measurements, shown in Fig. 35, confirm this general trend. For STO, no significant magnetic hardening can be observed, while for MgO and MAO the anisotropy field is increased. For MgO grown samples, the anisotropy field $\mu_0 H_a$ is at around 0.15 T ($H_a = 1500$ Oe) compared to α' -Fe₈N on MAO with $\mu_0 H_a = 0.2$ T ($H_a = 2000$ Oe). However, the scaling of H_a with sample thickness has to be considered carefully. While the increased hardening for lower mismatch points to improved properties for relaxed, ergo thicker films, samples discussed in 6.1 achieved similarly high H_a even for thicknesses of around 30 nm. A potential reason for these discrepancies is the mass flow controller which regulates the nitrogen flow into the radical source. It is strongly affected by the close proximity to the source due to rf stray fields caused by the plasma discharge. This leads to small variations of flow in the range of 0.01 sccm which were observed to cause significant changes in the magnetic properties. While this issue

Table 2: Suitable buffer layer materials, their lattice constants (taken from [183]), and the respective mismatch to α' -Fe₈N with $a = b = 5.718$ Å.

Material	Lattice constant/Å	Diagonal/Å	Mismatch/%
Pd	3.891	5.501	4.0
Pt	3.923	5.548	3.1
Al	4.049	5.726	-0.1
Cr	2.884($\times 2$)	—	-0.7
Au	4.079	5.769	-0.8
Sn	5.831	—	-1.9

could be minimized by properly grounding the controller, it was not possible to fully eliminate it.

Contrary to Yang et al. and Ji et al., who observed an up to 20% increased magnetization with tensile strain by either utilizing an Ag underlayer or Fe underlayers on MgO with different thicknesses, the magnetization for these samples does not display a trend as a function of mismatch (Fig. 34) [118, 119]. For all substrates, RMS interface roughnesses, which were determined by XRR fitting, scale with layer thickness, thus further indicating that a relaxation is taking place for all films. Surprisingly, despite MgO having a large negative mismatch to α' -Fe₈N, the roughnesses are almost identical to those found for samples grown on MAO. However, α' -Fe₈N with a compressive strain to STO at the interface exhibit a large roughness of 4.6 nm for the approximately 70 nm thick film.

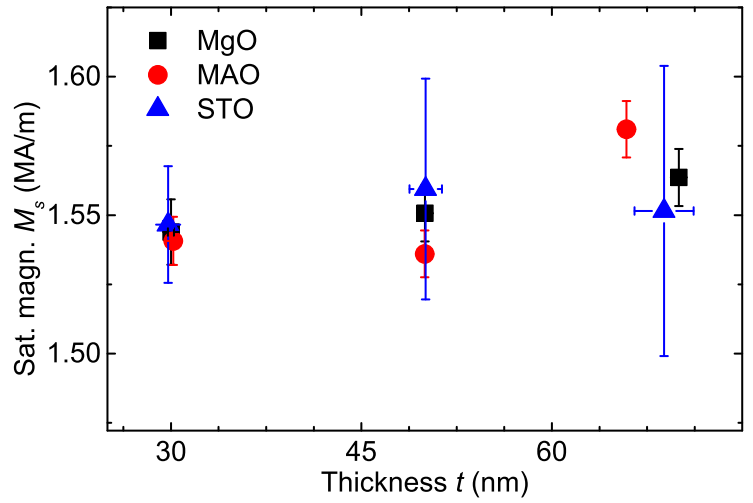


Figure 34: $M_s(300\text{K})$ of Fig. 35 and plotted against the α' -Fe₈N layer thickness for MgO, MAO, and STO.

It stands to reason that a mismatch between that of MAO and MgO could be beneficial for the growth of α' -Fe₈N. The mismatch could be engineered by either utilizing sufficiently thick, therefore fully relaxed, underlayers of suitable compounds, different substrates, or different underlayer thicknesses on a fixed substrate. However, to allow a precise determination of the magnetization, non-ferromagnetic materials should be chosen as buffer layers. A list of elemental buffer layer candidates with their respective mismatch to α' -Fe₈N is given in table 2.

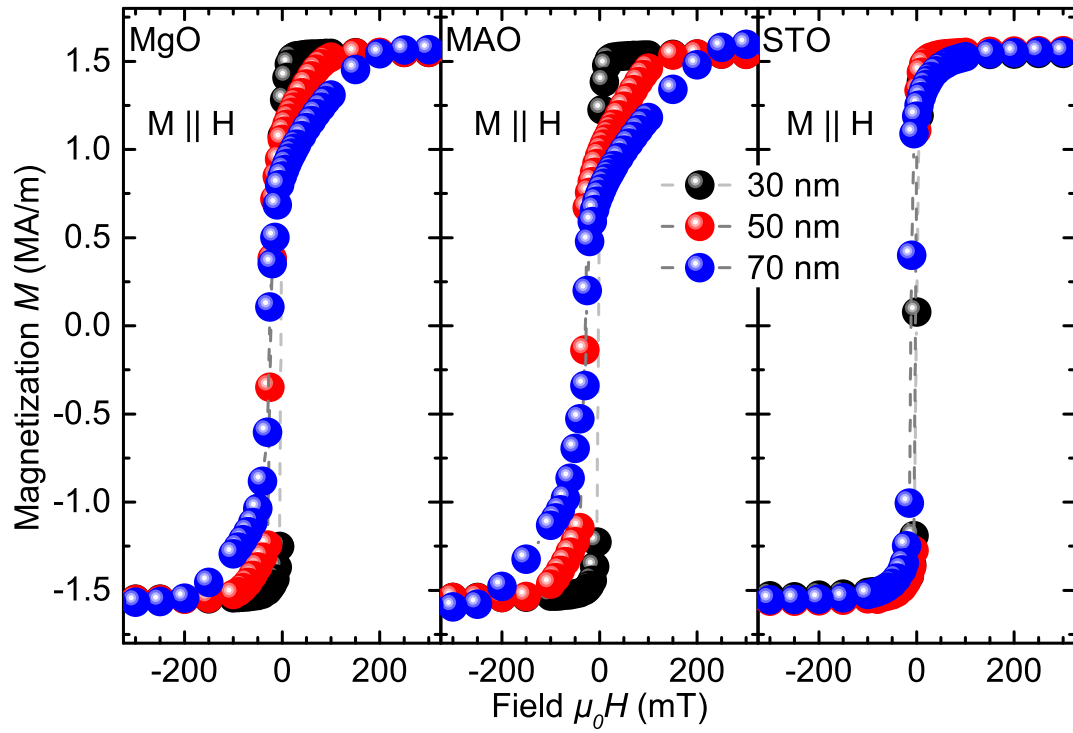


Figure 35: Room temperature half hysteresis SQUID measurements of α' -Fe₃N films with MgO, MAO, and STO substrates as a function of the thickness.

6.4 Annealing of α' -Fe₈N

According to established literature reports, the ordered phase α'' -Fe₁₆N₂ can be obtained from samples containing near phase pure α' -Fe₈N by annealing them at temperatures between 373 and 473 K. This induces a regular arrangement of the Fe-N octahedra in the sample and, as discussed in section 4.1, potentially results in an increased saturation magnetization. In order to investigate this effect, an MBE grown sample was subjected to an annealing procedure in a vacuum of approximately 5×10^{-3} Pa (10^{-5} mbar) for a total of 45 hours at 423 K. The experiment was conducted in an Anton-Paar heat dome, which allows to immediately observe any structural evolution by in-situ XRD measurements. In Fig. 37 the results from 26 to $32^\circ 2\theta$, to check the possible appearance of the α'' -Fe₁₆N₂ (002) superstructure reflex, and additionally from 55 to 67 to $32^\circ 2\theta$, to monitor any change in the (004) reflex, are displayed.

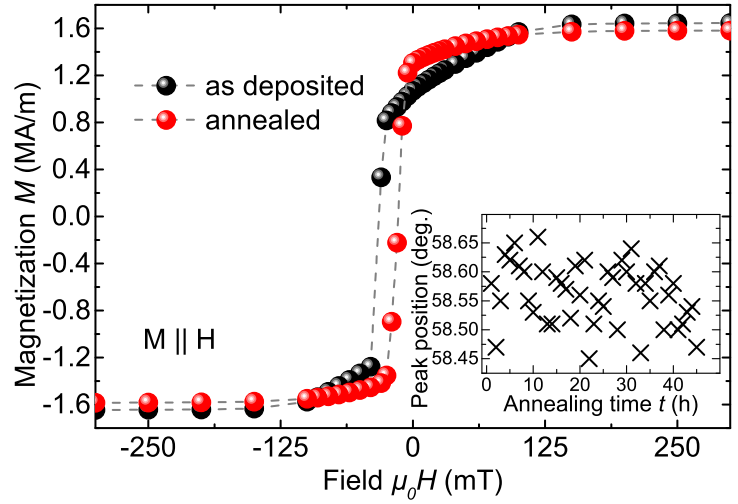


Figure 36: Comparison of room temperature SQUID measurements before and after annealing for 45 hours at 423 K. The inset shows the position of the α' -Fe₈N (004) reflex as a function of annealing time.

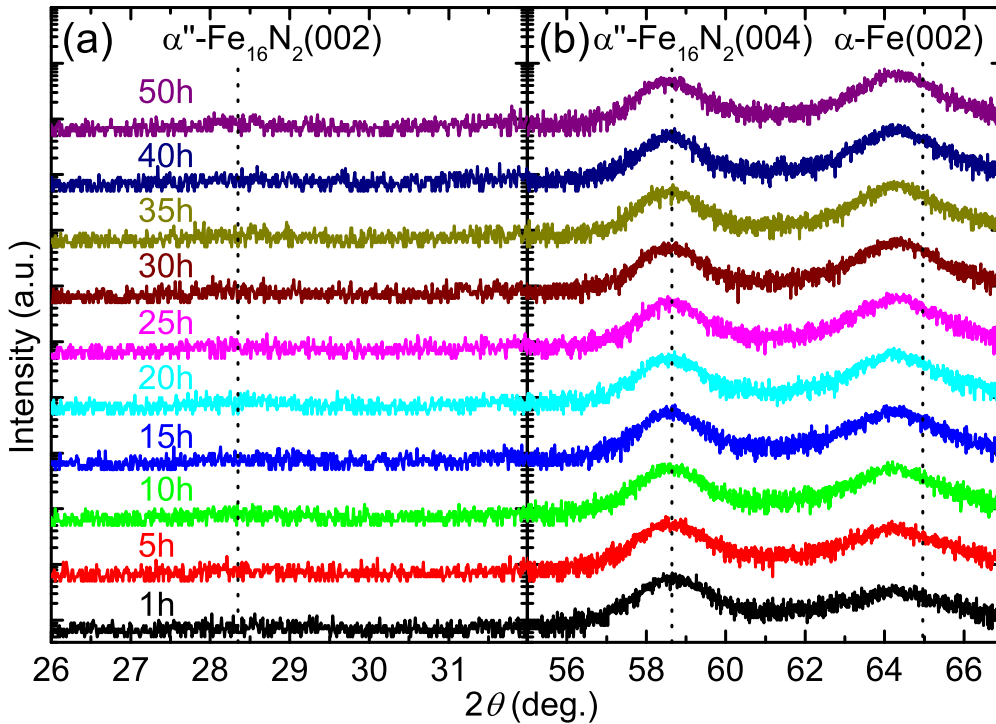


Figure 37: XRD patterns for (a) 26 to 32° and (b) 55 to 67 to $32^\circ 2\theta$ of an α' -Fe₈N sample annealed at 423 K.

Even for annealing times of 45 hours, the superstructure reflex that is expected to lie at $2\theta = 28.35^\circ$ does not appear, evident from Fig. 37(a). In addition, no significant increase of the α' -Fe₈N (004) peak intensity nor a peak shift (Fig. 36 inset) can be observed, as shown in figure 37(b). At the same time, iron recrystallizes in the sample, illustrated by the (002) reflection of α -Fe becoming more pronounced. This indicates a degradation of the phase, although the annealing temperature is well below the decomposition temperature given in most reports, around 453 to 473 K, as summarized in section 4.3. The degradation of the phase is also mirrored by the inferior magnetic properties, as evident by a direct comparison of the sample before and after the annealing experiment in Fig. 36. Both, saturation magnetization as well as anisotropy field are reduced after the annealing, reverting the sample from its semi-hard back to a soft magnetic behaviour, an effect also observed by Jiang et al. for annealing at 473 K [96]. Yamamoto et al. and Widenmeyer et al. both found similar properties for nanoparticle samples of α'' -Fe₁₆N₂, with the start of decomposition lying at around 373 K and the full decomposition requiring several tens of hours or longer [155, 157]. Although the applied temperature utilized in this experiment would be expected to result in a decomposition of approximately 2% of the phase according to Yamamoto et al., a more advanced decay could be caused by higher effective sample temperatures within the heat dome. However, a reduction of the magnetic anisotropy through differences in the local ordering does not require a large volume fraction of decomposed α' -phase. Similarly, the coercivity of a Fe-N magnet could significantly degrade by the decomposition into α -Fe, which acts as a centre for magnetization reversal.

To verify the results of Yamamoto et al., who extrapolated a long term stability for temperatures of 353 K or lower [155], a second sample was annealed at this temperature for a total of 55 hours, with otherwise identical conditions to the previous experiment. Similar to the previous experiment, the α'' -Fe₁₆N₂ (002) superstructure reflex does not appear in the XRD patterns plotted in Fig. 39(a). There are two possible reasons for this. For one, the intensity of the superstructure reflex is significantly lower than the (004) reflex with an expected intensity ratio of 1 : 13.8 for a sample with perfectly ordered Fe₆N octahedra [184]. However, even for this ideal case, the peak intensity would lie below the noise level of the XRD measurement. Another possibility for the absence of a long range ordering could be an insufficient temperature. Contrary to the previous experiment, the intensity of the α -Fe (002) reflex is not increased over the course of the experiment (see Fig. 39(b)), thereby giving a first indicator for the stability of the α' -phase at this temperature. This claim is confirmed by SQUID measurements, shown in figure 38. While the magnetic anisotropy is not as high as for the previously utilized sample due to differences in the stoichiometry, the measurements before and after the annealing step are essentially identical.

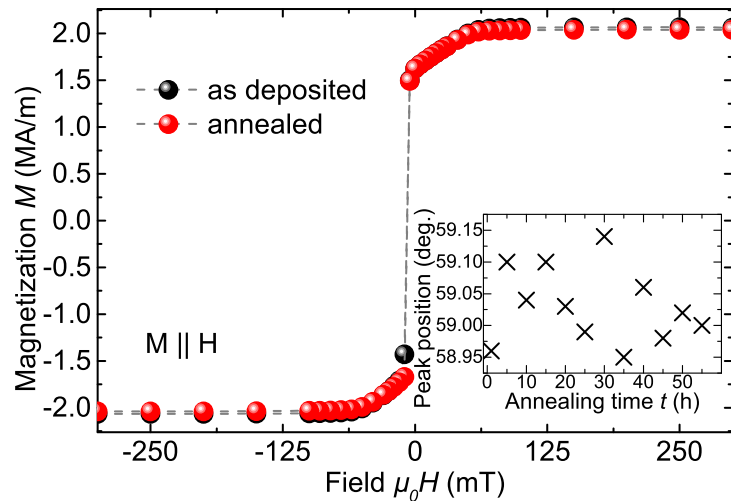


Figure 38: Comparison of room temperature SQUID measurements before and after annealing for 55 hours at 353 K. The inset shows the position of the α' -Fe₈N (004) reflex as a function of annealing time.

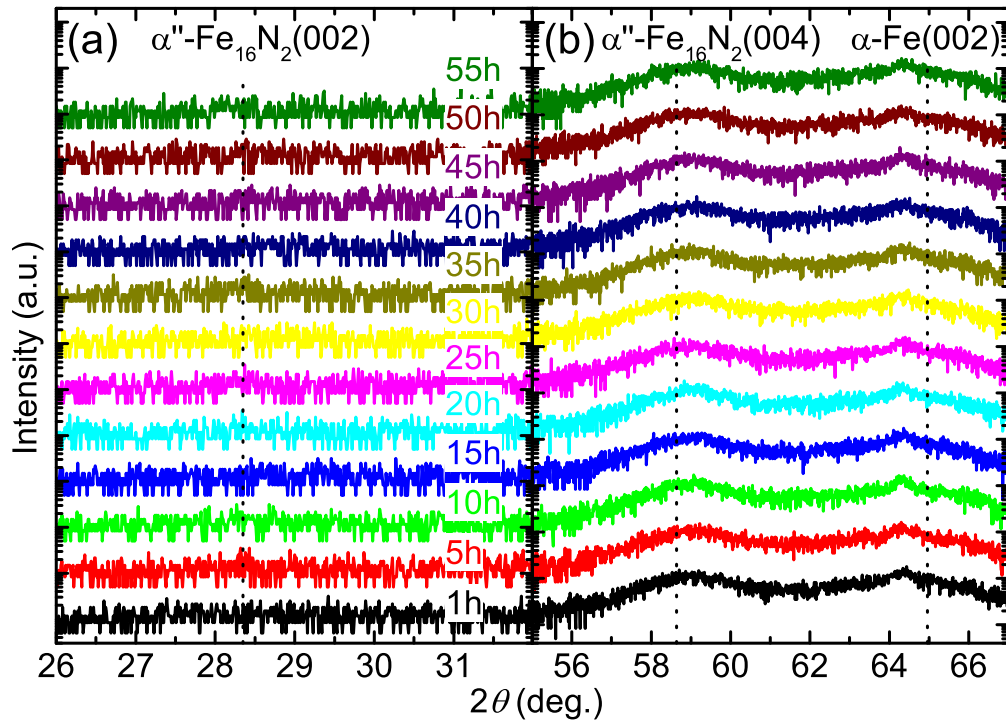


Figure 39: XRD patterns for (a) 26 to 32° and (b) 55 to 67 to 32° 2θ of an α' -Fe₁₆N₂ sample annealed at 353 K.

6.5 Substitution of Fe by Co in α' -Fe₈N

DFT simulations reported by Huang et al. show that by replacing one iron atom with cobalt in α'' -Fe₁₆N₂, a significant increase in the cohesive energy and therefore a decreased decomposition temperature of the phase could be achieved. Interestingly, the opposite effect is obtained once two iron atoms are substituted, resulting in a decrease of the cohesive energy to negative values around -0.42 eV [165]. While a study with Co content up to 30 at.% was already performed by Takahashi et al., the investigated stoichiometries were beyond the Co content equivalent to Fe₁₄Co₂N₂, which could explain the reported issues in forming such a phase [116].

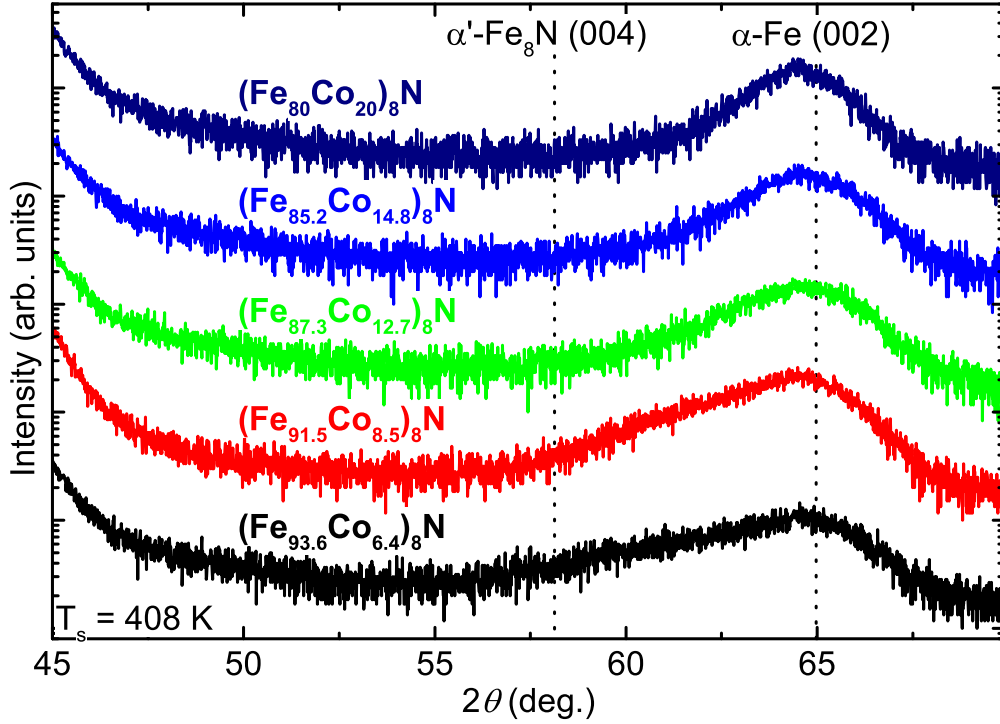


Figure 40: X-ray measurements of $(\text{Fe}_{100-x}\text{Co}_x)_8\text{N}$ samples grown on MgO (100) with 140 W rf power at 408 K and a total growth rate of 0.1 \AA/s .

To investigate this stoichiometry range, $(\text{Fe}_{100-x}\text{Co}_x)_8\text{N}$ films were grown by MBE. The growth parameters were chosen to be 140 W rf power, 408 K growth temperature, and a total growth rate of 0.1 \AA/s in order to achieve an optimum crystal growth, as described in section 6.1. The Co growth rates of 0.006 , 0.008 , and 0.012 \AA/s were calculated for a sticking coefficient of 100% in accordance to the desired iron to cobalt ratio of 15 : 1, 14.5 : 1.5, and 14 : 2, respectively. In addition, two non-stoichiometric samples with Fe:Co ratios of 85 : 15 and 80 : 20 were synthesized with Co rates of 0.014 and 0.019 \AA/s . As can be seen from the XRD patterns shown in Fig. 40, the lowest Co rate inhibits a tetragonal distortion of the unit cell within the sample. However, the α -Fe (002) reflex is strongly asymmetric with a FWHM of 5.8° , with the corresponding widths of 1.8 and 4° for the higher and the lower angle flank, respectively. Generally, reasons for XRD peak asymmetries are distributions of crystallite sizes or stacking faults as well as strain [185]. It stands to reason that the low growth temperature utilized for the samples leads to a reduced surface diffusion, resulting in inhomogeneously distributed Co. Due to cobalt locally reducing the incorporation of nitrogen in Fe_8N_x , a distribution of unit cell sizes and therefore varying levels of strain can be assumed as the reason for the peak asymmetry. This is supported by the samples grown with higher cobalt rates, where the asymmetric peak gradually reverts to a symmetric reflex at 64.5° . Higher rates lead to a more ho-

mogeneous cobalt distribution, resulting in a significantly limited but homogeneous incorporation of nitrogen. However, the XRD reflexes could originate from a mixture of α' -Fe₈N_x with amorphous Co or FeCo with interstitial N. In case of the formation of a FeCo alloy with lattice constants corresponding to $a = b = c = 2.867$, 2.866 , and 2.860 Å for Fe₉₄Co₆, Fe_{87.7}Co_{12.3}, and Fe₇₁Co₂₉, respectively, an increasing relative peak shift from 0.4 to 0.6° would be observed as a function of the Co content [186–188].

Further analysis by the in-plane SQUID measurements, shown in Fig. 41(a), reveal that all samples exhibit a soft magnetic behaviour. The saturation magnetization (inset Fig. 41(a)) has a maximum at the Co content corresponding to the Fe:Co ratio of $14 : 2$ and decreases at higher concentrations. Despite the increase of M_s for one sample, K_1 remains near constant with 2.5×10^4 J/m³ (2.5×10^5 erg/cm³), which is larger than the reported anisotropies amounting to less than 7.3×10^3 J/m³ (7.3×10^4 erg/cm³) for FeCo alloys of varying composition [189, 190]. However, this magnetic anisotropy is lower than that of pure α' -Fe₈N and falls short of $K_1 = 3.18 \times 10^6$ J/m³ (3.18×10^7 erg/cm³), predicted by Zhao et al. through DFT calculations, for Fe₁₂Co₄N₂ [191].

By fitting the temperature dependent magnetization data according to the equation proposed by Kuz'min and subtracting the substrate contribution in the manner described in section 6.1, the curves shown in Fig. 42 are obtained. The corresponding Curie temperatures for samples with Fe:Co ratios of $15 : 1$, $14 : 2$ and $80 : 20$ are (699 ± 43) , (730 ± 79) , and (955 ± 17) K, respectively. An increase in Co content results in an increased Curie temperature, although the samples with $15 : 1$ and $14 : 2$ Fe:Co ratio exhibit a slightly lower T_C compared to α' -Fe₈N. It can be concluded that this is likely due to the formation of FeCo phases, whose T_C is known to increase as a function of the Co content, in parallel to locally forming iron nitrides instead of forming a FeCoN alloy [151]. Especially for the samples with low Co content, difficulties were encountered when fitting the experimental data. This could only be reduced by separately fitting two temperature ranges, below 200 K and above. By doing so, each sample could be fitted by a T_C well above 1000 K, which is in the range of the expected values for FeCo and a significantly lower T_C . While these results initially appear to be contradictory to Takahashi et al., a significant nitrogen incorporation, as reported, was not achieved in this study [116].

In addition to varying the utilized Co rate, the effect of additional nitrogen by increasing the rf power was

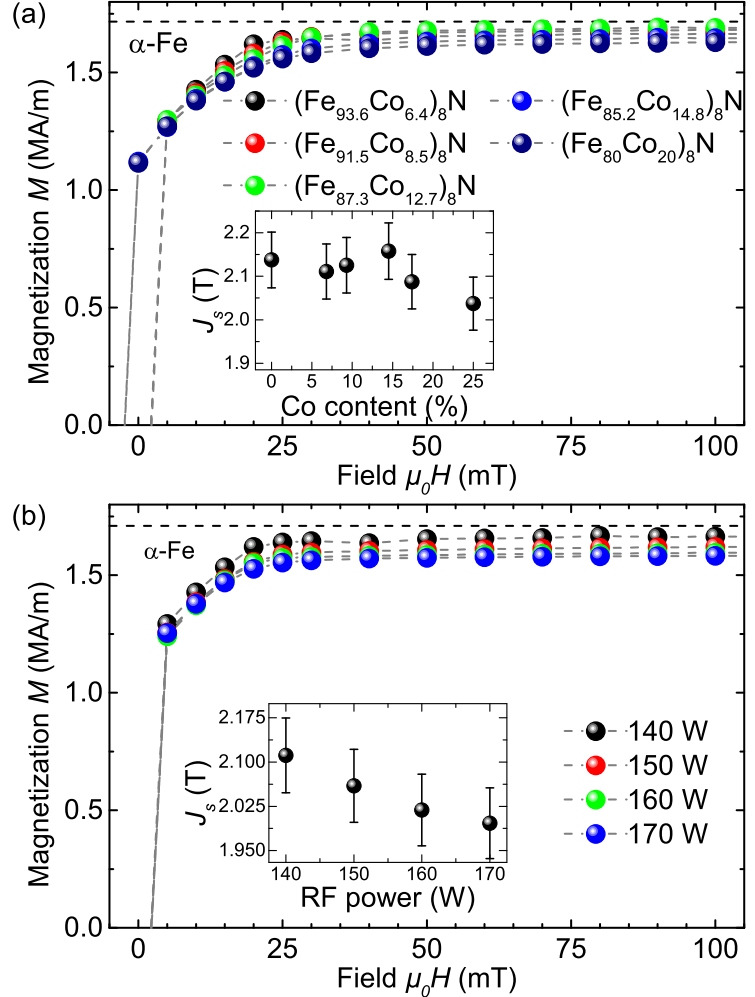


Figure 41: Room temperature half hysteresis curves of (a) $(\text{Fe}_{100-x}\text{Co}_x)_8\text{N}$ samples shown in Fig. 40 and (b) $(\text{Fe}_{93.6}\text{Co}_{6.4})_8\text{N}$ samples grown with increasing rf power. The insets depict M_s against the Co content and rf power, respectively.

studied for the rates corresponding to a Fe:Co ratio of 15 : 1 with otherwise identical conditions compared to the previous series. However, this resulted in identical XRD patterns which are therefore not shown and a continuously decreasing trend of the saturation magnetization as a function of the rf power (Fig. 41(b)). This could be caused by the formation of nanocrystalline γ' -Fe₄N or Co₄N with their respective reported saturation magnetization values of 675 and 1432 kA/m (675 and 1432 emu/cm³) [59, 63, 192].

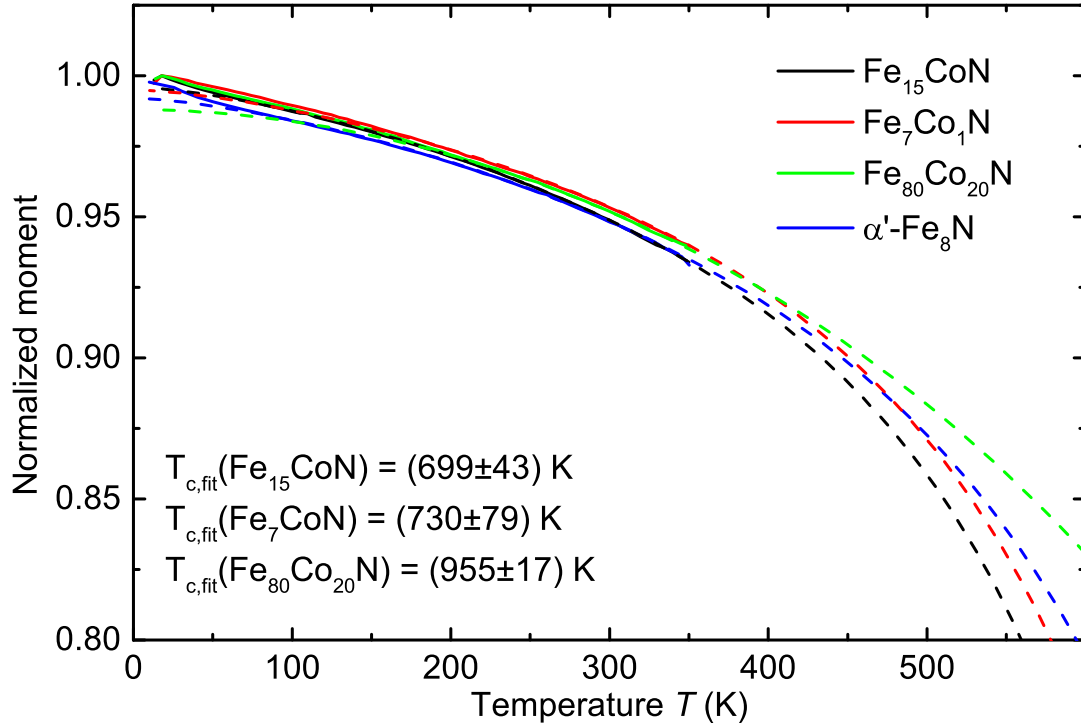


Figure 42: Magnetization versus temperature measurements from 10 to 350 K for $(\text{Fe}_{100-x}\text{Co}_x)_8\text{N}$ samples with $x = 6.4, 12.7,$ and 20 . The displayed Curie temperatures were extracted by fitting the curves from 100 to 350 K.

6.6 α' -Fe₈N as a potential permanent magnet candidate

The results obtained for the saturation magnetization of α' -Fe₈N support experimental as well as theoretical investigations which report M_s to lie close to that of α -Fe, if slightly lower. M_s values between 1620 and 1630 kA/m (1620 and 1630 emu/cm³) could be reproducibly obtained independent of the utilized deposition technique, giving further evidence against a giant magnetic moment. The anisotropy constant K_1 was extracted from the anisotropy field and amounted to 1.19×10^5 to 2.05×10^5 J/m³ (1.19×10^6 to 2.05×10^6 erg/cm³). The larger values for sputtered samples are most likely caused by the broader range of adjustment for the growth kinetics this technique offers compared to MBE. When separately comparing the magnetic anisotropy and magnetization, K_1 is of a similar magnitude as the commercially available SrFe₁₂O₁₉ with approximately 3.6×10^5 to 5×10^5 J/m³ (3.6×10^6 to 5×10^6 erg/cm³) while the M_s of α' -Fe₈N is more than four times larger than 366 kA/m (366 emu/cm³), the M_s of the ferrite. At the same time, due to iron being the most abundant transition metal in the earth's crust and nitrogen being the most abundant gas in our atmosphere, the resource cost of the iron nitrides is extremely low. However, for any given ferromagnetic material to be qualified as a permanent magnet, its intrinsic coercivity must be larger than its saturation magnetization [18]. Due to the high M_s of α' -Fe₈N in combination with its average anisotropy, a magnet built out of the iron nitride would demagnetize itself. This is mirrored in the empirical hardness parameter

$$\kappa = \left(\frac{2K_1}{\mu_0 M_s^2} \right)^{\frac{1}{2}} \quad (81)$$

which should be larger than 1 for a permanent magnet [18]. For α' -Fe₈N, κ lies between 0.19 and 0.25, for the least and most favourable M_s and K_1 combinations, respectively, both of which fall short of the required value.

The reported Curie temperature was confirmed by fits of the M versus T behaviour of the α' -phase and yielded (770 ± 73) K, albeit with a large error due to the limited temperature range available. While this T_C is lower than that of, e.g., AlNiCo₅ or Sm₂Co₁₇ with around 1100 K, it is suitably high for most applications in electric motors or generators and close to that of SrFe₁₂O₁₉ [18]. Unfortunately, the biggest drawback of α' -Fe₈N for its use in any application is the low decomposition temperature. As already mentioned in detail in section 4.3, the onset of decomposition lies slightly above 353 K. This result is supported by the performed annealing experiments, although further studies are necessary in order to precisely pinpoint the decomposition temperature. An attempt to improve this quantity through substitution of one or more iron atoms by cobalt was not successful, due to the increasingly limited nitrogen incorporation as a function of the Co rate. However, it stands to reason that no substitution of Fe by Co was achieved in this study.

7 Growth and characterization of interstitial Fe-B

Due to α' -Fe₈N and α'' -Fe₁₆N₂ reportedly starting to decompose at temperatures as low as 353 K, they are unsuitable for most applications [155, 158]. Interestingly, while Ohtsuka et al. theorized that by replacing the nitrogen by carbon similar, if slightly reduced, magnetic moments can be obtained through the lattice expansion, an effect that could also be exploited by boron was so far neglected [193]. This might be attributed to the fact that in the equilibrium phase diagram, no phases Fe_xB with $x \geq 3$ exist [194]. In addition, the boron solubility on interstitial positions in α -Fe is close to zero at room temperature, although it increases at elevated temperatures [195]. The challenge in this system is that known thermodynamic phases like Fe₂B and FeB as well as the metastable phase Fe₃B form at equilibrium conditions or higher temperatures due to the lower formation energy of substitutional compared to interstitial boron [194–198]. However, the interstitial concentration of boron in iron was shown to strongly depend on the presence of impurities in general or alloying elements like chromium [199, 200]. In addition, Reichel et al. performed DFT calculations which confirmed that for 11.1 at.% interstitial boron, a c/a ratio of 1.13 for a bct strained α -Fe can be achieved. While the change in magnetic anisotropy was not calculated for this scenario, it was shown experimentally that interstitial boron can be introduced in Co_{0.4}Fe_{0.6} to induce a tetragonal distortion and an increased magnetic anisotropy of $K_1 = 5 \times 10^5 \text{ J/m}^3$ ($5 \times 10^6 \text{ erg/cm}^3$) [200, 201]. Although these results are encouraging, the underlying mechanism of anisotropy increase in interstitially distorted materials is mostly unknown, as mentioned in section 4.2. Only recently, Zhang et al. found out that a specific local ordering of nitrogen interstitials in α'' -Fe₁₆N₂, in addition to the symmetry break by the tetragonal distortion, is crucial to the increased magnetic anisotropy as well as the occurrence of a perpendicular magnetic anisotropy [124, 202].

In the first section of this chapter, section 7.1, a study towards the formation of interstitial boron as a function of growth temperature is presented. The lattice distortion that results from interstitial boron in the iron lattice is then investigated in section 7.2. Finally, the deviation from the expected magnetic behaviour that was observed in the first two sections is analysed and explained via DFT in section 7.3. For all studies, boron was evaporated from a high temperature effusion cell (HTEZ, Dr. Eberl MBE Komponenten GmbH) with iron being supplied by e-gun evaporation. All samples were grown with a target thickness of 30 nm and were additionally capped with a 5 to 10 nm thick film of either Ag or Ta to prevent potential oxidation.

7.1 Temperature dependence of B solubility

To get a first estimation on the behaviour of the iron rich side of the iron boron system, the sample growth temperature was varied starting from 373 K, a temperature suitable for α' -Fe₈N growth, up to 773 K in steps of 100 K. For each temperature step, samples with three different boron rates of 0.004, 0.008, and 0.013 Å/s, were grown on MgO (100). The rates were chosen by the ratio of atoms assuming a sticking coefficient of 100% which would result in an expected boron content of approximately 2.9, 5.8, and 9.5 at.%, respectively. The XRD patterns of all samples for each temperature and each growth rate are shown in Fig. 43. Interestingly and contrary to nitrogen interstitials, growth temperatures of 373 and 473 K lead to films that are mostly amorphous for boron rates higher than 0.004 Å/s. This is caused both by an increased crystallization temperature, an effect which is known to scale with the boron content, as well as an increased defect density in the iron lattice [201, 203]. Starting at 473 K, a peak shift of the α -Fe (002) reflex towards lower angles can be observed. This effect is much more pronounced for a growth temperature window around 573 K, where a comparably good crystal quality can be observed in addition to a systematic peak shift to lower diffraction angles as a function of the boron rate, a first indicator for the existence of interstitial boron. At higher growth temperatures, the peak shift is reduced again or even vanishes, indicating that less or no boron can be incorporated into the lattice. In conclusion, a sufficiently high temperature is necessary in order to form a highly crystalline sample with boron interstitials, while at too high temperatures above 573 K, although being more favourable for interstitial occupation according to Fors et al., the thermodynamic formation of equilibrium iron boron

phases starts [195, 202].

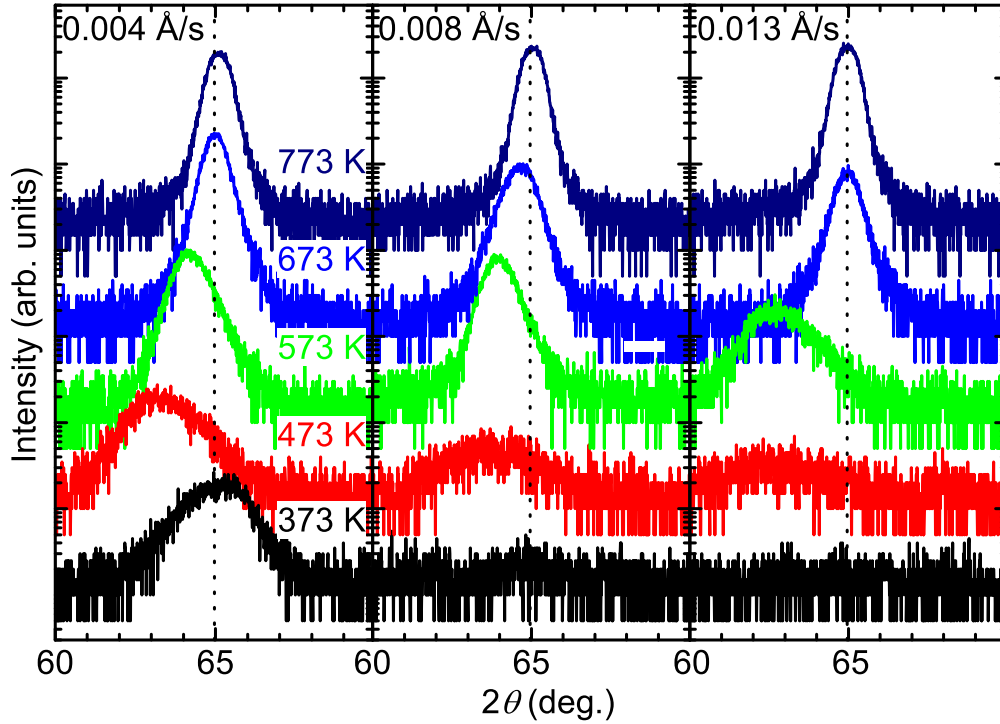


Figure 43: XRD patterns around the original α -Fe (002) reflection for different growth temperatures from 373 up to 773 K with boron rates of 0.004 (left graph), 0.008 (centre graph), and 0.013 $\text{\AA}/\text{s}$ (right graph), the dotted line indicates the position of the α -Fe (002) reflex [202].

7.2 Structural and magnetic properties of interstitial Fe-B

In order to further investigate the effect of interstitial boron, a fine scan of the boron rate from 0.004 to about 0.018 $\text{\AA}/\text{s}$ was performed in steps of about 0.0015 $\text{\AA}/\text{s}$ at the optimized growth temperature of 573 K. The resulting θ - 2θ diffraction patterns are shown in Fig. 45(a) and confirm, in line with the previous observations, a continuous shift of the α -Fe (002) reflex to lower angles in addition to a peak broadening with increasing boron rate. For samples grown at rates above 0.0135 $\text{\AA}/\text{s}$ (the top three patterns in Fig. 45), the peak positions remain constant and the peak intensities decrease, indicating that the maximum solubility is reached. The observed shift of the (002) diffraction peak is qualitatively identical to the change of the c -lattice constant of α' - Fe_8N_x with increasing nitrogen content x . The additional α -Fe (110) reflection that was observed at low boron rates was also observed for iron nitride samples and is further discussed in the appendix. Fig. 45(b) shows the evolution of the extracted a - and c -lattice constants for the interstitial iron boron (filled symbols) as well as α' - Fe_8N_x samples (open symbols). The content of interstitials was extrapolated by X-ray photoelectron spectroscopy (XPS) for the iron boron samples. It can be seen that the out-of-plane lattice monotonously increases with increasing boron and nitrogen content with α' - Fe_8N having a larger c -axis lattice constant of 3.136 \AA compared to the iron boron samples with $c = 2.950 \text{\AA}$. Contrary to the different out-of-plane lattice constants, the in-plane lattice slightly shrinks from $a = b = 2.868 \text{\AA}$ (α -Fe [168]) to $a = b = 2.812 \text{\AA}$ for the Fe-B system and $a = b = 2.811 \text{\AA}$ for Fe-N system, respectively. In accordance to Vegard's law, this linear relationship of the lattice constants as a function of the boron rate proves that boron occupies interstitial positions in the iron lattice [180]. Although the trend for the tetragonal distortion is identical for both the boron and the nitrogen interstitial system, the maximum achieved c/a ratio at the same nominal boron content of

12% was approximately 1.05, i.e. half the tetragonalisation as compared to α' -Fe₈N_x with $c/a = 1.1$ [202].

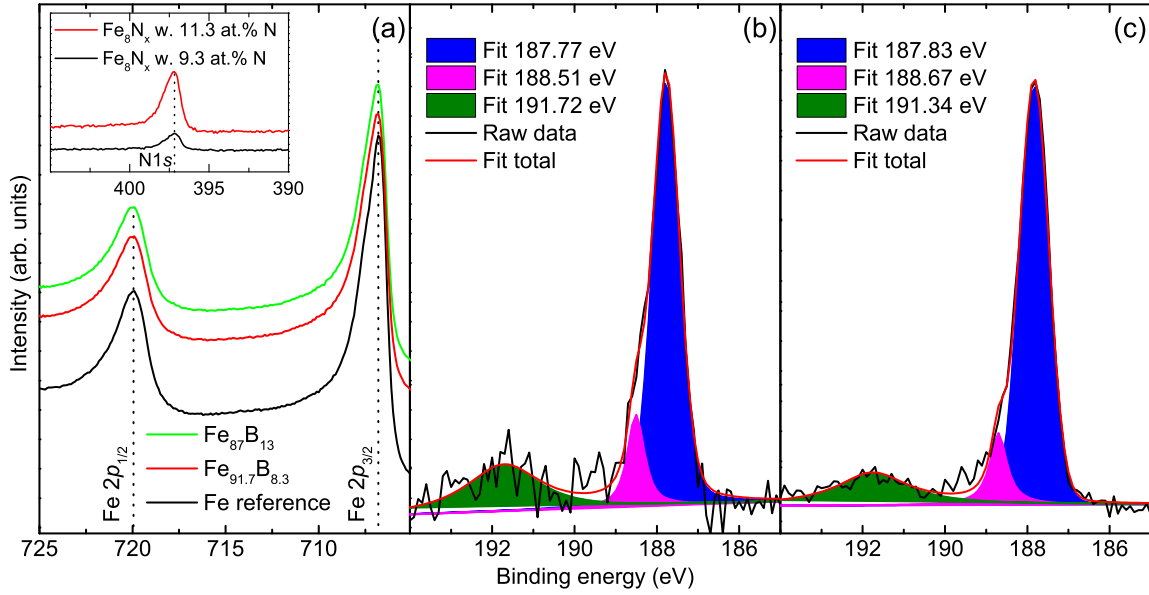


Figure 44: XPS measurements of the iron 2*p* spectra for the samples grown with 0.012 and 0.016 Å/s compared to pure α -Fe as a reference. The inset depicts the boron 1*s* spectrum for the sample grown at 0.016 Å/s.

XPS measurements were performed in order to quantify the ratio of iron to boron in the samples as well as to get an insight in the changes of the electronic structure. Prior to the measurement, the samples were subjected to ion beam etching by Ar ions at 2kV acceleration voltage until residual carbon or oxygen adsorbates completely vanished from the survey spectrum. The iron 2*p* spectra of a pure iron sample and two iron boron samples grown at rates of 0.012 and 0.016 Å/s are shown in Fig. 44(a). When comparing the iron 2*p* lines, no significant chemical shift can be observed. The essentially pure iron spectrum indicates a weak hybridization between iron and boron that mostly influences the peak position of the boron due to the iron to boron ratio of roughly 8 to 1. The relative boron content of the films calculated by the ratio of integrated peak intensity of the boron 1*s* and iron 2*p* spectra was corrected by the relative sensitivity factor and yielded about 8 and 12 at.%, respectively [202].

For the sample with 8 at.% boron shown in Fig. 44(b), a small shoulder peak at 188.5 eV and a broad low-intensity peak around 191.7 eV were detected in addition to the high-intensity B1*s* emission at 188.5 eV. The two weaker peaks are even more pronounced in the boron 1*s* spectrum of the film with the higher boron content as evident from Fig. 44(c). In literature, the segregation of boron into grain boundaries was observed by transmission electron microscopy in iron boron thin films grown at similar conditions [203]. The broad peak at higher binding energies was attributed to grain boundary segregated boron while the shoulder at around 188.5 eV might be attributed to the formation of FeB or Fe₂B, for which a binding energy of 188.1 eV was reported [204]. By comparing the integrated intensity ratios of these peaks and assuming that the highest intensity peak corresponds interstitial boron, the effective interstitial boron content in the iron lattice was estimated. The resulting amounts of interstitial boron are 3.7 and 7.4 at.% boron for the films containing nominally 8 and 12 at.% boron, respectively. While the α' -Fe₈N_x sample with a corresponding nitrogen content of 7 at.% still exhibited a larger c/a of 1.08, the tetragonal distortion caused by the effective interstitial boron is now comparable (see the plot of the c/a ratio against the corrected boron content as shown in the inset of Fig. 45(b)) [202].

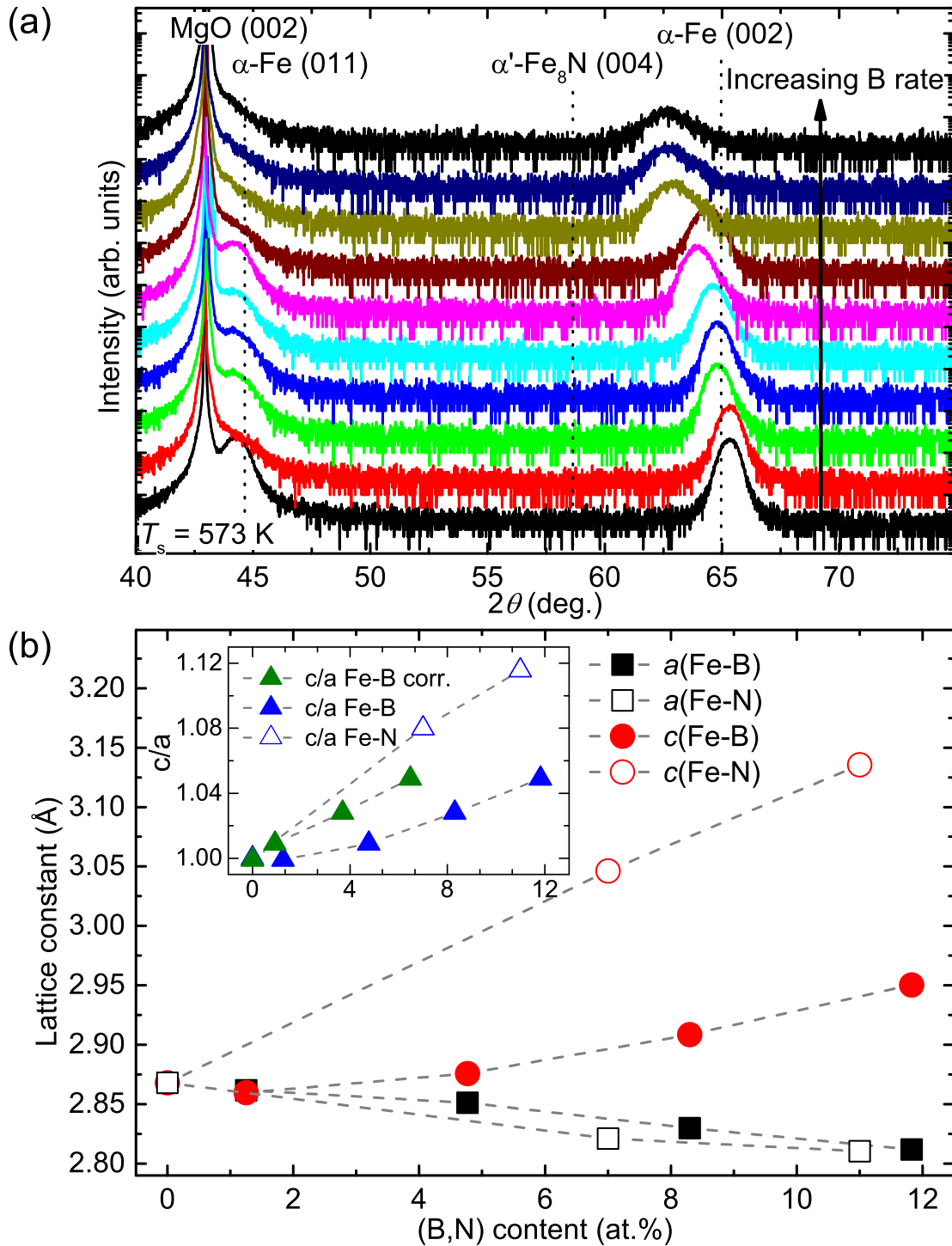


Figure 45: (a) XRD out-of-plane patterns with increasing boron rates (from bottom to top) with an indicator for the α' -Fe₈N (004) reflex, (b) extracted a - (squares), c -lattice constants (circles), and c/a values (inset, triangles) for the iron boron (filled symbols) and the iron nitrogen system (open symbols).

While the shift of the out-of-plane reflex is qualitatively identical to the behaviour the c -lattice constant of α' -Fe₈N_{*x*} exhibits with increasing nitrogen content x , the existence of a tetragonal distortion was validated by additional in-plane XRD measurements. Figure 45(b) depicts the evolution of the a - and c -lattice constants, extracted from the (011) reflex for the interstitial iron boron (filled symbols) as well as the (022) reflex for α' -Fe₈N_{*x*} samples (open symbols). The boron content was extrapolated from the two samples subjected to XPS according to the ratio of the rates used for deposition. It can be seen that while the out-of-plane lattice constant monotonously increases with increasing boron and nitrogen content, the in-plane lattice constants shrink for both systems. In accordance to Vegard's law [180], this linear relationship of the lattice constants as a function of the boron rate proves that boron occupies interstitial positions in the iron lattice. However, while the trend observed for the tetragonal distortion is identical for both the boron and the nitrogen interstitial system and the a -lattice constant behaves essentially the same, the maximum c/a which could be achieved with boron was approximately 1.05, therefore half the tetragonalisation compared to α' -Fe₈N_{*x*} with $c/a = 1.1$. This could be caused by, both, a Boron segregation as well as the formation of other iron boride phases which would reduce the amount of boron incorporated in the lattice compared to the average boron content in the film [202].

The crystallographic orientation of the Fe-B films with respect to the MgO (100) substrate was determined by ϕ -scans of the (011) reflex for α -Fe and Fe-B samples in comparison to the (022) reflex of MgO. It is well known that α -Fe as well as α' -Fe₈N show an in-plane alignment of Fe[110] and α' -Fe₈N[110] || MgO[100] [125, 145]. As can be seen from Fig. 46, iron boron samples grown with boron rates of 0.005 and 0.015 Å/s exhibit the same relative growth orientation with Fe-B[110] || MgO[100]. The evolution of the shrinking in-plane lattice constant corresponds to an increased lattice misfit and tensile strain from -3.68% for α -Fe to -5.57% for Fe-B [202].

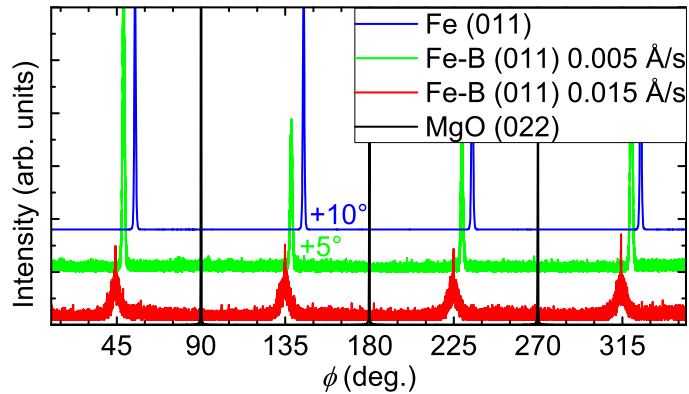


Figure 46: ϕ -scan of MgO (022), Fe-B (011) with the minimum as well as the maximum utilized boron rates, and α -Fe (011) for comparison [202].

The hysteresis behaviour of the iron boron samples is shown in Fig. 47. For all samples, the in-plane hysteresis shows a clear in-plane magnetic anisotropy with a saturation magnetization that is continuously decreasing up to a B content of 12 at.% with an M_s of 1450 kA/m (1450 emu/cm³). The overall reduced M_s compared to the iron nitride is most likely caused by the segregation of paramagnetic boron since linear M - H -contributions to the magnetization are subtracted from each measurement. For the out-of-plane hysteresis, shown in the inset of Fig. 47, only the shape anisotropy can be observed. The anisotropy constant K_1 was determined through torque measurements performed at 300 K for two samples containing approximately 4 and 12 at.% boron. The measurement for the sample containing 4 at.% boron shows cubic as well as tetragonal terms contributing to the MAE when fitting the data to a Fourier series, while the second sample exhibits only tetragonal terms. After subtracting the shape anisotropy, it is found that the magnitude of K_1 increases from -3.0×10^5 to -5.1×10^5 J/m³ (-3.0×10^6 to -5.1×10^6 erg/cm³) [202].

In order to gain insight on the temperature dependent magnetic properties of the interstitial iron boron system, the Curie temperature was extrapolated through the means already described in section 6.1 and according to the equation proposed by Kuz'min [177]. The experimentally measured data as well as the corresponding fits are shown in Fig. 48. Surprisingly, although the low boron rate sample has a similar

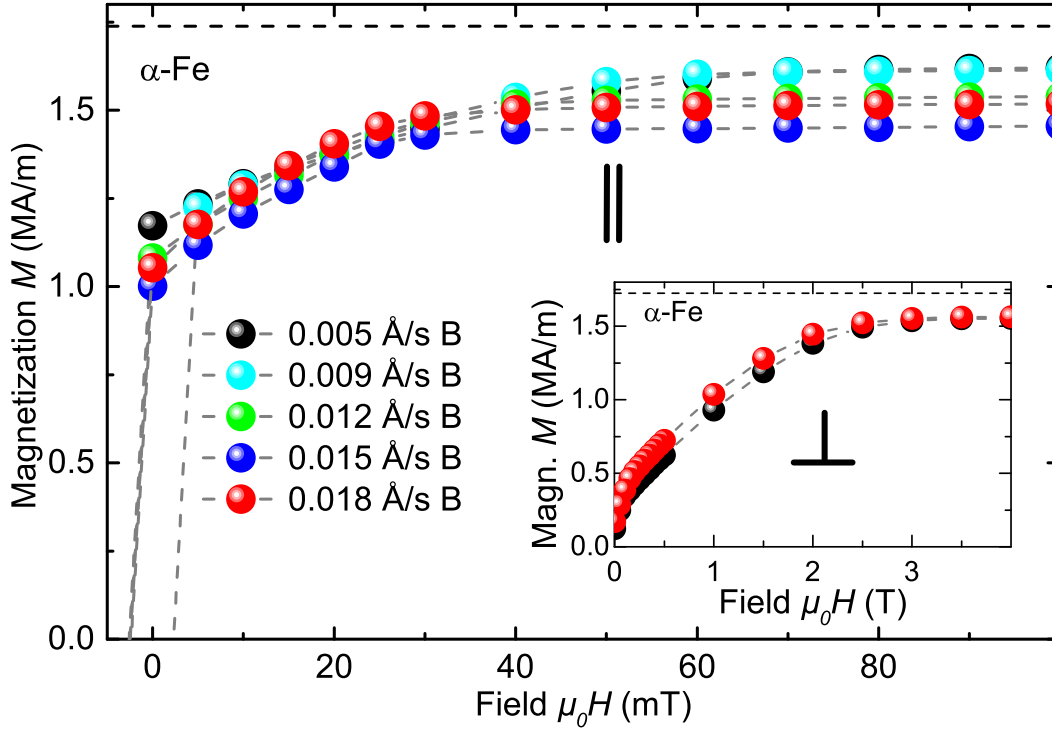


Figure 47: In-plane room temperature M - H half hysteresis for samples grown with different boron rates. The inset shows the out-of-plane hysteresis for samples with the lowest and highest utilized boron rate [202].

curve progression to α -Fe, the higher curvature around 250 K, indicating the presence of a second ferromagnetic contribution with a lower T_C , results in a drastically reduced Curie temperature of (624 ± 23) K with $s = 0.19 \pm 0.01$ and $p = 5.9 \pm 0.4$. When adjusting the fitting range to below 250 K, the Curie temperature amounts to around 950 to 980 K, which lies within the expected range of the T_C . This could be caused by Fe_2B with a Curie temperature of 598 K or amorphous $\text{Fe}_{90}\text{B}_{10}$ with a T_C of 480 K, the formation the latter being a possible reason for the difference between both Fe-B films' Curie temperature. The formation of FeB as well as Fe_3B can be excluded due to their significantly higher T_C of 1015 and 897 K, respectively [205, 206]. The film grown at a boron rate of 0.015 \AA/s exhibits comparable properties to α' - Fe_8N with an extrapolated Curie temperature of (856 ± 67) K, which is significantly higher than (770 ± 73) K, the ordering temperature of the α' -phase. However, the effective boron content in the iron lattice was beforehand shown to be lower than the interstitially dissolved nitrogen in the α' - Fe_8N sample. It stands to reason that the Curie temperature shows a similarly decreasing trend for increased amounts of interstitial boron as is observed in the interstitial iron nitrides, indicating that further boron incorporation up to an iron to boron ratio of 8 : 1 would also decrease the T_C . The s and p parameters that were found for this fit are 0.53 ± 0.05 and 4 ± 0.6 , respectively. According to equation 80, these values correspond to a spin wave stiffness of $(191 \pm 27) \text{meV}\text{\AA}^2$, similar to $(180 \pm 41) \text{meV}\text{\AA}^2$, the value found for α' - Fe_8N .

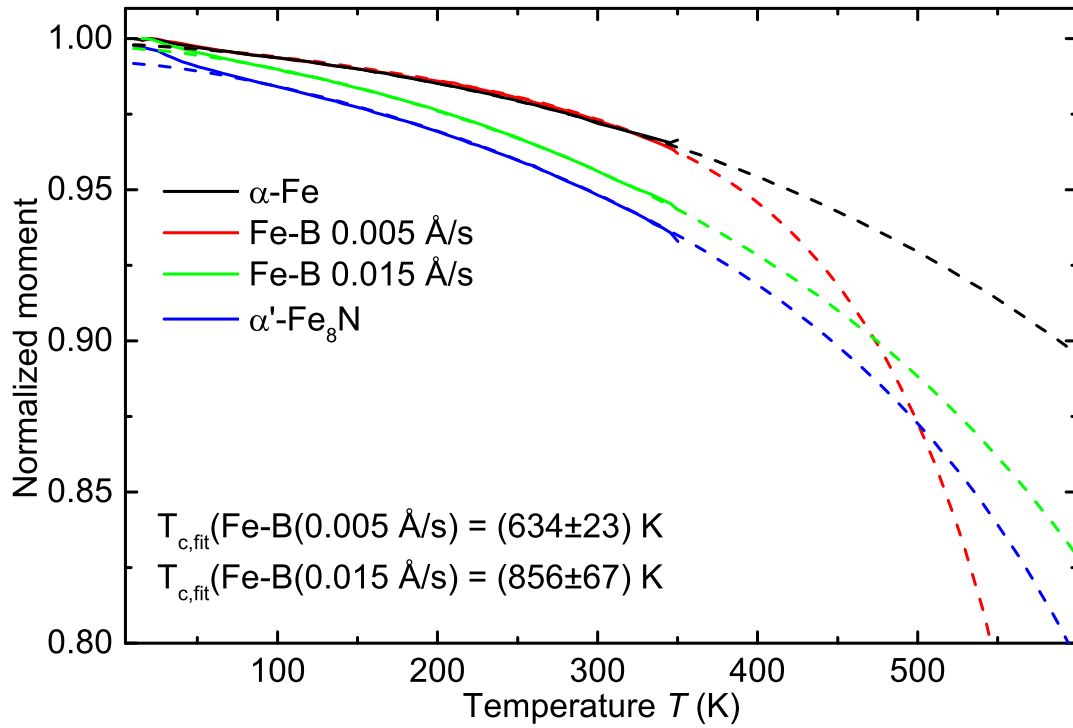


Figure 48: Magnetization versus temperature measurements (solid lines) from 10 to 350 K for samples grown with different boron rates of 0.005 and 0.015 Å/s as well as α -Fe and α' -Fe₈N samples for comparison. The displayed Curie temperatures were extracted by fitting the curves from 100 to 350 K (dashed lines).

7.3 DFT calculations on anisotropy in Fe-B

DFT calculations were performed by Hongbin Zhang from TU Darmstadt in order to clarify the origin of the in-plane easy axis as well as the reason for the reduced anisotropy. Here, a $2 \times 2 \times 2$ α -Fe supercell was created based on the experimental lattice constants and filled with one or two Fe_6B octahedra. For 6 at.% boron in the iron lattice it was found that the MAE is indeed reduced with an easy-axis lying in the film plane. When the boron content is increased to 12 at.%, four different cases of local ordering, shown in Fig. 49, have to be considered. Except for the third arrangement, where the Fe_6B octahedra are separated from each other, configurations (a), (b), and (d) correspond to octahedra connected in the (110) plane, along the [110] direction, and along the [001] direction, respectively. Table 3 shows the calculated values for the total energies, the lattice volume, the MAE, and the change of orbital momentum for these four variations of ordering as well as for the case of 6 at.% boron [202].

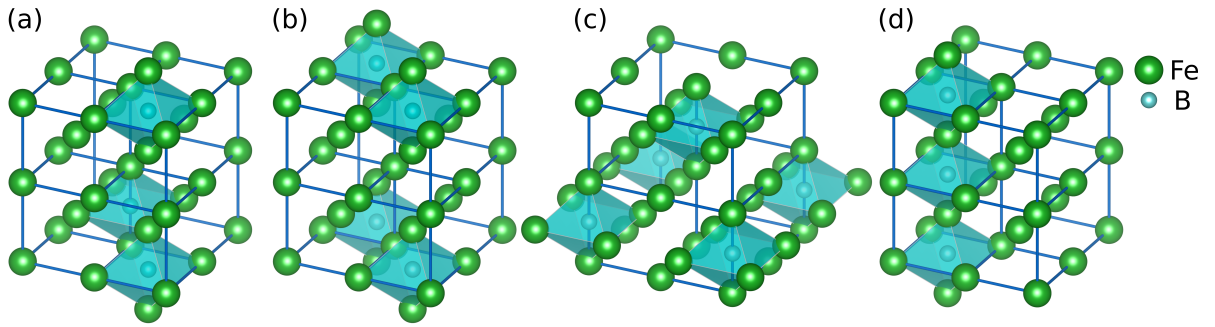


Figure 49: Four possible geometries of Fe_6B within a $2 \times 2 \times 2$ supercell. The Fe_6B octahedra are connected in (a) the (110) plane, (b) along the [110] direction, and (d) along the [001] direction and are (c) separated .

After optimizing the atomic positions, the total energies are found to increase from case (a), the most stable configuration, to case (c) which corresponds to a local ordering that was shown to be favoured by α' - Fe_8N , with an energy difference of 16.86 meV per Fe atom [124]. While the arrangement (a) and (b) are energetically similar, the configuration (d) is significantly unfavoured. Such a trend is still true for full relaxation calculations where the lattice constants are allowed to change from the experimentally determined values. Furthermore, the two more stable cases (a) and (b) exhibit an in-plane magnetic easy-axis, thereby confirming the experimental results. The experimentally determined $K_1 = -5.1 \times 10^5 \text{ J/m}^3$ ($-5.1 \times 10^6 \text{ erg/cm}^3$) is several times larger than the theoretically predicted anisotropy at a boron concentration of approximately 12 at.%. However, this film exhibits an interstitial B concentration of 6.5 at.%, whose MAE agrees well with the calculated value for the case of 6 at.% B. Although the MAE of α' - Fe_8N can be understood based on the variation of orbital moments between two magnetization directions, the Fe-B system behaves differently, implying that the perturbation theory [51] does not apply in this case. These results underline that the change in electronic and magnetic behaviour is not only induced by the structural distortion caused by the interstitial occupancy of nitrogen and boron but is strongly dependent on the influence of the interstitial element on the local electronic structure [202].

Table 3: Calculated values for the relative total energy ΔE , the MAE, and the change of orbital momentum Δm_l for 6 and 12 at.% boron in the lattice. Note that positive MAE values indicate spontaneous out-of-plane magnetization direction [202].

	ΔE /(meV per Fe)	MAE/(MJ/m ³ , (Merg/cm ³))	$\Delta m_l/\mu_B$
6 at.% B	N.A.	-0.3770 (-3.770)	-0.0521
12 at.% B			
Case (a)	0	-0.1180 (-1.180)	-0.0026
Case (b)	6.69	-0.0383 (-0.383)	-0.0672
Case (c)	16.86	0.2921 (2.921)	0.0026
Case (d)	548.29	0.2396 (2.396)	-0.0302

7.4 Viability of interstitial Fe-B

Thin films consisting of tetragonally distorted Fe-B can be reproducibly grown at temperatures up to approximately 573 K, with a decomposition temperature potentially even beyond that. The amount of soluble boron was, as expected from literature, strongly dependent on the temperature. However, while the structural properties are promising and exhibit a behaviour which is qualitatively identical to the iron nitride system albeit with a much higher temperature stability, the maximum solubility of boron in the iron lattice limits the achievable c/a ratio to around 1.05. With 7.4 at.% boron in the iron lattice, as determined by XPS peak fitting, the Curie temperature of the Fe-B film was (856 ± 67) K and therefore higher than the T_C of α' -Fe₈N [202].

Contrary to α' -Fe₈N, a PMA was not achieved through this distortion, a fact which could be confirmed by DFT. The calculations revealed that the local ordering of boron interstitials is different to that of nitrogen in α' -Fe₈N, resulting in an in-plane easy axis, thereby further demonstrating the importance of the local chemical environment on the magnetic properties of interstitially distorted α -Fe. Additionally, the predicted anisotropies match the measured ones reasonably well [202].

While the anisotropy of the Fe-B system is suitable for permanent magnet applications due to the easy-plane configuration, it is conceivable that by choosing the proper alloying element to substitute one or more iron atoms in the lattice as well as by tailoring the in-plane strain, the local ordering could be engineered in order to achieve a desirable high magnetic anisotropy while maintaining a sufficiently high decomposition temperature as observed for Fe-B films. This approach is supported by Reichel et al. who reported that for a high Co content ≥ 50 at.%, a tetragonal distortion with $c/a \approx 1.04$ can be achieved via boron or carbon incorporation and leads to an increased anisotropy of $K_1 = 5 \times 10^5$ J/m³ (5×10^6 erg/cm³) [201, 207].

8 Conclusion

This work was divided into two parts, the first part being the evaluation of the known interstitial iron nitride α' -Fe₈N as a potential permanent magnet candidate. As a first step, the growth conditions for ϵ -Fe_xN and γ' -Fe₄N, both of which lie in close proximity to α' -Fe₈N in the phase diagram, were determined through MBE. It was found that the crystallization of different phases can be influenced by the choice of substrate in addition to the variation of the growth parameters, especially for low temperatures around 373 K. Surprisingly, at 473 K, it was possible to tetragonally distort the γ' -Fe₄N lattice with a maximum c/a of approximately 1.03, a previously unreported development, alongside the formation of other, more nitrogen containing nitrides in an amorphous or nanocrystalline form. An increase of magnetic anisotropy could not be observed through the tetragonalisation of the phase, most likely due to the similarity of γ' -Fe₄N to γ -Fe. Based on the observed phases, an MBE phase diagram of the binary iron nitrogen system was developed for temperatures below 623 K. While it is qualitatively identical to the phase diagrams found in literature, the phase space for γ' -Fe₄N was determined to be larger in terms of stoichiometry as well as temperature.

With these results as a starting point for the growth conditions of α' -Fe₈N, an optimization was performed in order to pinpoint the exact temperature and nitrogen window required for the formation of the phase. It was shown that at an iron growth rate of 0.1 Å/s with a nitrogen flow of 0.07 sccm and an rf power of 145 W, a maximum magnetic anisotropy of $1.19 \times 10^5 \text{ J/m}^3$ ($1.19 \times 10^6 \text{ erg/cm}^3$), which is in good agreement with theoretical prediction as well as experimental reports, was found for the films with an M_s of 1620 to 1630 kA/m (1620 to 1630 emu/cm³). Although the Curie temperature was extrapolated to lie at $(770 \pm 73) \text{ K}$, a slightly lower value than the reported 813 K, the general trend of reduced Curie temperatures at increased nitrogen content for the iron nitrides is still true.

Since MBE grown nitrides are limited in their lowest possible nitrogen content due to the operation limits of the radical source, a full nitrogen scan could not be performed on this unit. Therefore, rf magnetron sputtering was utilized to optimize the growth conditions and then grow a series of films ranging from pure iron up to stoichiometric α' -Fe₈N. The saturation magnetization values found for the α - and the α' -phase were closely matched to the results obtained for MBE grown films while the magnetic anisotropy was larger with $K_1 = 2.05 \times 10^5 \text{ J/m}^3$ ($2.05 \times 10^6 \text{ erg/cm}^3$), most likely due to an improved local ordering in the sputtered samples. The magnetic moments evolved linearly from 2.28 to $2.47 \mu_B/\text{Fe}$ as a function of the lattice expansion, thereby confirming the magnetovolume effect as the origin of the increased moments. The results obtained were supported by XMCD measurements performed by Yu-Chun Chen from MPI IS Stuttgart as well as DFT calculations performed by Hongbin Zhang from TU Darmstadt. A giant magnetic moment exceeding $2.8 \mu_B/\text{Fe}$, reported by several groups for both, α' -Fe₈N as well as α'' -Fe₁₆N₂, was not found in any sample synthesized during this work.

Based on several reports of increased magnetic moments close to the substrate or buffer layer interface, a thickness study with different substrates that exhibit lattice mismatches from -3.95 (MgO) to 0.08 (MAO) up to 3.5% (STO) compared to α' -Fe₈N was performed. It was found that small to negative mismatches are required for the phase to grow crystalline, evident from the lack of α' -Fe₈N reflexes in the XRD patterns for all films grown on STO. In line with this observation, the increase of magnetic anisotropy compared to α -Fe was the largest for the smallest mismatched substrate, MAO. Unfortunately, due to variations in the radical source behaviour, further conclusions could not be made from this study.

Additionally, an annealing study was performed. This step is required, according to literature reports, to form the ordered α'' -phase from α' -Fe₈N. It was shown that the decomposition starts at much lower temperatures than generally assumed in literature. Already annealing over 45 hours at 423 K led to a degradation of the magnetic properties. Results obtained by Yamamoto et al. were confirmed with a second annealing procedure at 353 K where no decomposition could be observed [155]. At the same time, no evidence for an ordered phase could be found during both annealing procedures, emphasizing a well controlled annealing temperature of approximately 373 to 393 K in order to form the α'' -phase.

As a final step during the investigation of α' -Fe₈N, the first attempt to modify the binary iron nitride system was performed by supplying cobalt in addition to iron during the sample growth. It was shown that an increasing iron to cobalt ratio up to 80 : 20 suppresses the formation of α' -Fe₈N, an effect that could not be circumvented by increasing the amount of nitrogen supplied. An increase of the Curie temperature extracted from M versus T fits of these samples was found to be most likely caused by the presence of FeCo phases with a high Curie temperature and not due to an improvement of α' -Fe₈N through Co incorporation, an assumption that is supported by the soft magnetic response of all samples grown for this study.

For the second part, an attempt to tetragonally distort α -Fe via the introduction of boron was performed. While this procedure is not possible at equilibrium conditions, the presence of boron interstitials in iron was confirmed in MBE grown samples. In accordance to literature reports, it was shown that the solubility of boron in interstitial positions of iron is strongly dependent on the (growth) temperature. At 573 K, a temperature significantly higher than the decomposition temperature of α' -Fe₈N, a maximum shift of the out-of-plane lattice constant was observed. In-plane measurements confirmed the qualitative similarity of the Fe-N and Fe-B systems with a lattice parameters shrinking and c lattice parameters growing as a function of boron and nitrogen. However, the maximum tetragonal distortion with a c/a ratio of approximately 1.05 was lower than for interstitial nitrogen with $c/a \approx 1.12$.

This behaviour was further investigated via XPS. Here, the Fe2p spectra measured were identical to those of α -Fe. By fitting the B1s spectra, it was found that only a portion of the boron introduced into the samples was incorporated in the iron lattice. The subsequently corrected evolution of c/a ratios versus boron content are close to the expected tetragonalisation with similar amounts of nitrogen. It was assumed, in accordance with a report of Otake et al., that boron not incorporated in the lattice accumulates at the grain boundaries and therefore does not contribute to the tetragonal distortion [203]. Surprisingly, SQUID measurements revealed an in-plane anisotropy over the whole range of boron contents. Although this lies in contrast to the evolution of a perpendicular magnetic anisotropy observed in α' -Fe₈N, the results were confirmed by DFT calculations performed by Hongbin Zhang from TU Darmstadt, thus emphasizing the importance of local ordering for the magnetic anisotropy in these interstitial iron compounds. Curie temperatures extracted from fits were showing a decreasing T_C as a function of boron content, similar to the nitrogen counterpart. While the Curie temperature of the sample with the highest B concentration was (856 ± 67) K and therefore higher than that of α' -Fe₈N, a further reduction with increased boron content in the iron lattice can be expected.

Summarizing, the magnetic moment and anisotropy of the iron nitride α' -Fe₈N were investigated to clarify the variations reported in literature. Through systematic study it was found, in accordance with several theoretical and experimental reports, that the magnetic moment increases as a function of the unit cell volume. However, due to the increasing cell volume the resulting M_s decreases compared to α -Fe. In addition, although the M_s is independent of the deposition technique used, the magnetic anisotropy is higher for sputtered samples, an effect most likely related to ordering. The novel interstitial Fe-B system behaves structurally similar to the α' -Fe₈N_x system but exhibits undesired in-plane anisotropy in combination with a comparably low magnetic anisotropy. Both systems demonstrate that it could be possible to combine the sufficiently high decomposition temperature of Fe-B with the desired hard magnetic properties by engineering the local ordering of interstitials.

9 Outlook

Although the interstitially distorted iron system offers many potentially interesting properties for permanent magnets, as was demonstrated for both, nitrogen and boron, the impact of ternary elements has so far been of minor interest and was only addressed for a few elements in literature. Systematic studies to investigate the influence of alloying elements on not only the saturation magnetization, which is the major focus in the existing literature on α' -Fe₁₆N₂ (e.g. references [116,127,143,208–210]), but also the Curie temperature, the MAE, and the decomposition temperature for these systems do not exist. This is especially surprising since Tayal et al. and Wang et al. reported an increase of thermal stability of α'' -Fe₁₆N₂ when alloyed with Al, Zr, or Ti, while the addition of Co decreased the stability, as shown by Takahashi et al. [116,164,166]. As already mentioned in section 4.3, these findings agree well with Bain's classification of the influence that alloying elements have on the phase diagram of iron from 1939 [167].

In order to investigate this behaviour in more detail, a Deutsche Forschungsgemeinschaft (DFG) proposal, entitled "Engineering magnetic anisotropy by structural distortion of bcc α -Fe and other cubic alloys", was submitted. By investigating ternary system (Fe_{100-x}Z_x)₈Y with Z being the alloying element and Y being interstitial N, B, or C, the aim is to gain a systematic understanding of the role of alloying elements in this group of materials. Since from the structural point of view, the interstitially distorted iron is close to α -Fe, it stands to reason that the classification offered by Bain also applies. In the ideal case, the formation of the γ' -phase could be fully suppressed by the proper alloying element. This effect would not only increase the thermal stability of the α' -phase but also increase its stoichiometry window, potentially allowing larger tetragonal distortions and consequentially larger magnetic anisotropies [154]. However, in addition to the structural changes induced by these modifications, an altered magnetic behaviour not only through the added element itself but also through the potential modification of the local ordering is to be expected. This becomes clear when considering the DFT calculations performed on nitrogen (see [124]) and boron interstitials (see section 7.3) which illustrate that this local ordering of the iron octahedra with the interstitial at the centre plays a significant role in the evolution of MAE in the phases of interest.

Furthermore, despite Co having a detrimental effect on the properties of α' -Fe₈N and the interstitial iron boron system having a low MAE, the addition of Co in the range of above 50 at.% to the interstitial iron boron and iron carbon system is of interest. Reichel et al. demonstrated by thin films grown at room temperature, that even for small tetragonal distortions up to $c/a \leq 1.04$, a significant increase of K_1 to $5 \times 10^5 \text{ J/m}^3$ ($5 \times 10^6 \text{ erg/cm}^3$) can be realized [201,207]. While the limited incorporation of B and C impeded a further increase of MAE in their studies, the influence of an increased growth temperature or a quaternary element on this system is unexplored until today.

While not included in the proposal, other dopants may be beneficial for the magnetic properties of the interstitial iron nitrides, as demonstrated by DFT calculations performed by Khan and Hong for Li, Be, B, C, and N doping of α'' -Fe₁₆N₂ in a recent publication. These elements were determined to act as impurities that locally distort the lattice, thereby increasing the MAE by 10 – 20% while maintaining the magnetization [211].

Finally, an additional point of interest is the thickness dependent study of the magnetic properties of α' -Fe₈N. As reported, the magnetic moment of α' -Fe₈N grown various substrates is dramatically increased close to the substrate interface or for films less than 20 nm thick [76,119,126,212]. This indicates, that large levels of strain, which can be maintained up to thicknesses at or slightly above the critical thickness, have a large influence on the magnetic moment due to the change of the N to Fe distances of the radial Fe8h as well as the axial Fe4e atoms within the Fe₆N octahedra. However, an iron underlayer was used for most of the reported studies. Since this complicates the precise determination of the magnetization of the iron nitride layer, future studies should be performed with either no or a non ferromagnetic underlayer (see table 2). In addition, Feng et al. found that the activation energy of the nitrogen ordering

is reduced for tensile strained layers, thereby facilitating the formation of the α'' -phase, although its evidence through XRD may be complicated due to the low intensities of the superstructure reflex [212]. Alternatively, by reducing the diffusivity, an increase of the thermal stability of the interstitial iron nitrides is conceivable. Combined with the formation of α'' -Fe₁₆N₂ from α' -Fe₈N through annealing, only briefly addressed in this work, these influences require a thorough analysis in order to be fully understood. Especially the necessary temperature for this annealing step, reported to be significantly higher than the onset of decomposition observed in this work, as elucidated in sections 4.3 and 6.4, need further study.

10 Publications

First author publications:

- Thin film phase diagram of iron nitrides grown by molecular beam epitaxy, D. Gölden, E. Hildebrandt, and L. Alff, *Journal of Magnetism and Magnetic Materials* 422 (2017) 407-411, <http://doi.org/10.1016/j.jmmm.2016.07.074>.
- Evolution of anisotropy in bcc Fe distorted by interstitial boron, D. Gölden, H. Zhang, I. Radulov I. Dirba, P. Komissinskiy, E. Hildebrandt, and L. Alff, *Physical Review B* 97 (2018) 014411, <http://doi.org/10.1103/PhysRevB.97.014411>.

Further publications:

- Magnetic properties of the Laves-type phases $\text{Ti}_2\text{Co}_3\text{Si}$ and $\text{Ti}_2\text{Fe}_3\text{Si}$ and their solid solution, C.M. Hamm, D. Gölden, E. Hildebrandt, J. Weischenberg, H. Zhang, L. Alff, and C.S. Birkel, *Journal of Materials Chemistry C* 4 (2016) 7430-7435, <http://doi.org/10.1039/C6TC02043G>
- Experimental and theoretical study of AC losses in variable asymmetrical magnetic environments, S.T. Ranecky, H. Watanabe, J. Ogawa, T. Oka, D. Gölden, L. Alff, and Y.A. Genenko, *Superconductor Science and Technology* 30 (2017) 085005, <http://doi.org/10.1088/1361-6668/aa73bc>

List of Figures

1	World rare-earth (RE) production in kT per country (left axis) and Chinese contribution to the rare-earth production (right axis). Data adapted from [4].	1
2	Year-end prices for the oxides of Ce, Nd, Dy, and Tb. The inset displays the price evolution for the oxides of Nd and Ce. Data adapted from [4].	2
3	Processes occurring during the thin film growth from the gas phase.	4
4	(a) Frank-van der Merwe growth, (b) Vollmer Weber growth, and (c) Stranski-Krastanov growth.	6
5	MBE instrumentation	9
6	Schematic RHEED patterns (a) for ideally flat surfaces, (b) during step-flow growth, and (c) island growth.	11
7	Sputtering instrumentation	15
8	Geometric relationship between the incident and diffracted X-ray, the plane distance d , and the X-ray path difference $d\sin\theta$	16
9	SQUID measurement of bare MgO and Al ₂ O ₃ substrates at 300 K compared to MgO at 10 K (symbols). The displayed susceptibilities are extracted from a fit of the linear part of the measurements (dashed lines).	23
10	(a) bct unitcell of α'' -Fe ₁₆ N ₂ with $a = 5.72 \text{ \AA}$ and $c = 6.29 \text{ \AA}$, (b) the same structure but displayed with a z-offset. Drawn according to structural data reported by K.H. Jack [65].	33
11	Saturation magnetization as a function of the ordering, estimated by the XRD intensity ratios. Data adapted from refs. [88, 89, 92, 102, 113, 116].	38
12	Temperature stability of α'' -Fe ₁₆ N ₂ as a function of time for different fractions of phase decomposition d . Adapted from Yamamoto et al. [155].	40
13	Fraction of α'' -Fe ₁₆ N ₂ phase decomposition d as a function of time for different annealing times. Several experimental reports with different parameters are indicated in the respective curves [77, 79, 88, 89, 91–93, 102, 104, 109, 113, 115, 117, 118, 120, 125, 127, 159, 160]. Adapted from Yamamoto et al. [155].	41
14	XRD patterns of a series of Fe-N films with increasing iron deposition rate from 0.04 $\text{\AA}/\text{s}$ to 0.1 $\text{\AA}/\text{s}$ at constant nitridation conditions onto (a) MgO (100), (b) Al ₂ O ₃ (0001), and (c) MAO (100) substrates at a growth temperature of 373 K. The star marks a substrate peak of Al ₂ O ₃ as well as MAO.	44
15	XRD patterns of Fe-N thin films with rf powers ranging from 120 to 200 W applied to the nitrogen radical source grown on MgO (100) at 373 K substrate temperature and a growth rate of 0.1 $\text{\AA}/\text{s}$	45
16	XRD patterns of thin films grown on MgO (100) with an increasing (from top to bottom) nitrogen flow through the radical source of 0 sccm, 0.02 to 0.10 sccm in 0.01 sccm steps, and 0.15 to 0.30 sccm in 0.05 sccm steps at a constant rf power of 300 W at 473 K.	46
17	Evolution of the c -axis lattice constant as a function of the nitrogen flow at constant rf power of 300 W at 473 K. In the inset, in-plane (black square) and the respective out-of-plane lattice constants (red circles) as well as the c/a ratio (blue triangles) are shown.	47
18	Saturation magnetization at 300 K and density versus nitrogen flow of samples grown at 473 K. The inset depicts a comparison between the magnetization curves for the lowest (black) and highest flow (red) utilized.	48
19	XRD patterns of γ' -Fe ₄ N thin films grown on MgO (100) at different nitridation conditions at 623 K. In the inset, the c -axis lattice constant (blue) and saturation magnetization M_s (black) are shown.	48

20	MBE thin film phase diagram of the iron nitride system, with the nitrogen being supplied by a nitrogen radical source. The experimental points used for this phase diagram are indicated by the crosses.	49
21	Evolution of $M_s(300\text{ K})$ and RMS roughness in α' -Fe ₈ N samples as a function of growth temperature.	50
22	XRD patterns of Fe-N thin films with constant nitridation conditions grown on MgO (100) at substrate temperatures between 373 and 573 K and a growth rate of 0.1 Å/s.	51
23	ϕ -scan of α' -Fe ₈ N (022) with respect to MgO (022).	51
24	XRD patterns of Fe-N thin films with rf powers ranging from 125 to 150 W applied to the nitrogen radical source grown on MgO (100) at 373 K substrate temperature and a growth rate of 0.1 Å/s [152].	52
25	RHEED patterns of α' -Fe ₈ N grown with a rate of 0.1 Å/s and an rf power of 145 W for increasing film thicknesses. The electron beam is parallel to the (100) orientation of MgO.	53
26	Saturation magnetization $M_s(300\text{ K})$ (squares) and anisotropy constant K_1 (circles) of α' -Fe ₈ N _x as a function of the rf power applied to the nitrogen radical source. The inset shows the M_V - H -curves of the sample grown with 150 W rf power.	54
27	Magnetization versus temperature measurements from 10 to 350 K for α -Fe and α' -Fe ₈ N. The displayed Curie temperatures were extracted by fitting the curves from 100 to 350 K.	55
28	XRD patterns of samples grown on MgO (100) by rf magnetron sputtering with a background pressure of 5 Pa (0.05 mbar), a total flow into the chamber of 4 sccm, 373 K growth temperature, 5.5 cm substrate to target distance, and 100 W rf power.	56
29	Comparison of M_s (squares) and K_1 (circles) at 300 K for sputtered (filled symbols) and MBE grown (open symbols) samples.	57
30	XRR measurements (straight lines) and fitted curves (crosses) for two α' -Fe ₈ N samples; one grown by MBE and one grown by sputtering.	57
31	Density (black) and magnetic moment (blue) of sputter grown α' -Fe ₈ N _x films as a function of the c -axis lattice constant. The inset depicts the evolution of the c -axis as a function of nitrogen flow with a linear fit through the data points.	58
32	Magnetic moment determined by SQUID (black) and XMCD (red) measurements at 300 and 10 K of sputter grown α' -Fe ₈ N _x films, respectively, as well as DFT calculations (blue) as a function of the nitrogen content. The inset shows the evolution of the ratio of orbital to spin moment, m_l/m_s	59
33	Influence of different substrates with -3.95% (MgO, left graph), 0.08% (MAO, centre graph), and 3.58% (STO, right graph) mismatch on the XRD patterns of 30, 50, and 70 nm thick α' -Fe ₈ N films grown at 408 K with 140 W rf power, a nitrogen flow of 0.07 sccm and an iron growth rate of 0.1 Å/s.	60
34	$M_s(300\text{ K})$ of Fig. 35 and plotted against the α' -Fe ₈ N layer thickness for MgO, MAO, and STO.	61
35	Room temperature half hysteresis SQUID measurements of α' -Fe ₈ N films with MgO, MAO, and STO substrates as a function of the thickness.	62
36	Comparison of room temperature SQUID measurements before and after annealing for 45 hours at 423 K. The inset shows the position of the α' -Fe ₈ N (004) reflex as a function of annealing time.	63
37	XRD patterns for (a) 26 to 32° and (b) 55 to 67 to 32° 2θ of an α' -Fe ₈ N sample annealed at 423 K.	63
38	Comparison of room temperature SQUID measurements before and after annealing for 55 hours at 353 K. The inset shows the position of the α' -Fe ₈ N (004) reflex as a function of annealing time.	64
39	XRD patterns for (a) 26 to 32° and (b) 55 to 67 to 32° 2θ of an α' -Fe ₈ N sample annealed at 353 K.	65

40	X-ray measurements of $(\text{Fe}_{100-x}\text{Co}_x)_8\text{N}$ samples grown on MgO (100) with 140 W rf power at 408 K and a total growth rate of 0.1 Å/s.	66
41	Room temperature half hysteresis curves of (a) $(\text{Fe}_{100-x}\text{Co}_x)_8\text{N}$ samples shown in Fig. 40 and (b) $(\text{Fe}_{93.6}\text{Co}_{6.4})_8\text{N}$ samples grown with increasing rf power. The insets depict M_s against the Co content and rf power, respectively.	67
42	Magnetization versus temperature measurements from 10 to 350 K for $(\text{Fe}_{100-x}\text{Co}_x)_8\text{N}$ samples with $x = 6.4, 12.7,$ and 20. The displayed Curie temperatures were extracted by fitting the curves from 100 to 350 K.	68
43	XRD patterns around the original α -Fe (002) reflection for different growth temperatures from 373 up to 773 K with boron rates of 0.004 (left graph), 0.008 (centre graph), and 0.013 Å/s (right graph), the dotted line indicates the position of the α -Fe (002) reflex [202].	71
44	XPS measurements of the iron 2 <i>p</i> spectra for the samples grown with 0.012 and 0.016 Å/s compared to pure α -Fe as a reference. The inset depicts the boron 1 <i>s</i> spectrum for the sample grown at 0.016 Å/s.	72
45	(a) XRD out-of-plane patterns with increasing boron rates (from bottom to top) with an indicator for the α' -Fe ₈ N (004) reflex, (b) extracted <i>a</i> - (squares), <i>c</i> -lattice constants (circles), and <i>c/a</i> values (inset, triangles) for the iron boron (filled symbols) and the iron nitrogen system (open symbols).	73
46	ϕ -scan of MgO (022), Fe-B (011) with the minimum as well as the maximum utilized boron rates, and α -Fe (011) for comparison [202].	74
47	In-plane room temperature <i>M-H</i> half hysteresis for samples grown with different boron rates. The inset shows the out-of-plane hysteresis for samples with the lowest and highest utilized boron rate [202].	75
48	Magnetization versus temperature measurements (solid lines) from 10 to 350 K for samples grown with different boron rates of 0.005 and 0.015 Å/s as well as α -Fe and α' -Fe ₈ N samples for comparison. The displayed Curie temperatures were extracted by fitting the curves from 100 to 350 K (dashed lines).	76
49	Four possible geometries of Fe ₆ B within a 2 × 2 × 2 supercell. The Fe ₆ B octahedra are connected in (a) the (110) plane, (b) along the [110] direction, and (d) along the [001] direction and are (c) separated	77
A.1	Construction design of BN discharge tube.	103
A.2	Construction design of BN aperture with (a) 41 and (b) 65 holes of 0.2 mm.	104
B.3	ϕ -scan of α -Fe(200) with respect to MgO(022).	105
B.4	Intensity of the (011) and (002) reflex as well as M_s plotted against the nitrogen flow, extracted from the measurements shown in Fig.B.6.	105
B.5	RHEED pattern of (a) an α' -Fe ₈ N sample and (b)-(d) samples grown with 0.04 Å/s and varying nitrogen flows; both recorded with the electron beam parallel to the (100) orientation of MgO.	106
B.6	XRD measurements of thin films grown at increasing nitrogen flow without using a plasma at 373 K and a growth rate of 0.04 Å/s.	106
C.7	RHEED patterns of bare MAO and MgO substrates along their (100) direction without, after 5, and after 30 minutes of annealing at 973 K in vacuum prior to deposition.	108
C.8	Flowcharts for samples grown by (a) MBE and (b) sputtering.	109

References

- [1] M. J. Kramer, R. W. McCallum, I. A. Anderson, S. Constantinides, Prospects for Non-Rare Earth Permanent Magnets for Traction Motors and Generators, *Jom* 64 (2012) 752–763. doi:10.1007/s11837-012-0351-z.
- [2] Eclipse Magnetics NdFeB Magnet Datasheet, http://www.eclipsemagnetics.com/media/wysiwyg/datasheets/magnet_materials_and_assemblies/ndfeb_neodymium_iron_boron_standard_ndfeb_range_datasheet_rev1.pdf, accessed 17.08.2017.
- [3] M. Sagawa, S. Fujimura, H. Yamamoto, Y. Matsuura, K. Hiraga, Permanent magnet materials based on the rare earth-iron-boron tetragonal compounds, *IEEE Trans. Magn.* 20 (1984) 1584–1589. doi:10.1109/TMAG.1984.1063214.
- [4] U.S. Geological Survey 2000-2017, https://minerals.usgs.gov/minerals/pubs/commodity/rare_earths/, accessed 30.07.2017.
- [5] K. Löwe, C. Brombacher, M. Katter, O. Gutfleisch, Temperature-dependent Dy diffusion processes in NdFeB permanent magnets, *Acta Mater.* 83 (2015) 248–255. doi:10.1016/j.actamat.2014.09.039.
- [6] K. Löwe, D. Benke, C. Kübel, T. Lienig, K. P. Skokov, O. Gutfleisch, Grain boundary diffusion of different rare earth elements in Nd-Fe-B sintered magnets by experiment and FEM simulation, *Acta Mater.* 124 (2017) 421–429. doi:10.1016/j.actamat.2016.11.034.
- [7] S. Sawatzki, I. Dirba, H. Wendrock, L. Schultz, O. Gutfleisch, Diffusion processes in hot-deformed NdFeB magnets with DyF₃ additions, *J. Magn. Mater.* 358 (2014) 163–169. doi:10.1016/j.jmmm.2014.01.055.
- [8] S. Sawatzki, C. Kübel, S. Ener, O. Gutfleisch, Grain boundary diffusion in nanocrystalline Nd-Fe-B permanent magnets with low-melting eutectics, *Acta Mater.* 115 (2016) 354–363. doi:10.1016/j.actamat.2016.05.048.
- [9] I. Poenaru, A. Lixandru, A. Dirks, J. Gassmann, R. Hord, O. Diehl, S. Sawatzki, A. Buckow, K. Gueth, R. Gauß, O. Gutfleisch, Cerium-substituted Nanocrystalline Melt-Spun Nd-Fe-B alloys for Resource-efficient Permanent Magnets, *REPM Proc. 24th Int. Workshop on RE and Future Permanent Magnets and their Applications*.
- [10] M. D. Kuz'min, K. P. Skokov, I. Radulov, C. A. Schwöbel, S. Foro, W. Donner, M. Werwiski, J. Rusz, E. Delczeg-Czirjak, O. Gutfleisch, Magnetic anisotropy of La₂Co₇, *J. Appl. Phys.* 118 (2015) 053905. doi:10.1063/1.4927849.
- [11] S. Sabet, E. Hildebrandt, F. M. Römer, I. Radulov, H. Zhang, M. Farle, L. Alff, Low-Temperature Phase c-axis Oriented Manganese Bismuth Thin Films With High Anisotropy Grown From an Alloy Mn₅₅Bi₄₅ Target, *IEEE Trans. Magn.* 53 (2017) 1–6. doi:10.1109/TMAG.2016.2636817.
- [12] E. F. Kneller, R. Hawig, The exchange-spring magnet - a new material principle for permanent-magnets, *IEEE Trans. Magn.* 27 (1991) 3588–3600. doi:10.1109/20.102931.
- [13] G. Moulas, A. Lehnert, S. Rusponi, J. Zabloudil, C. Etz, S. Ouazi, M. Etzkorn, P. Bencok, P. Gambardella, P. Weinberger, H. Brune, High magnetic moments and anisotropies for Fe_xCo_{1-x} monolayers on Pt(111), *Phys. Rev. B* 78 (2008) 14. doi:10.1103/PhysRevB.78.214424.
- [14] T. Burkert, L. Nordström, O. Eriksson, O. Heinonen, Giant Magnetic Anisotropy in Tetragonal FeCo Alloys, *Phys. Rev. Lett.* 93 (2004) 027203. doi:10.1103/PhysRevLett.93.027203.

-
- [15] J. M. D. Coey, P. A. I. Smith, Magnetic nitrides, *J. Magn. Magn. Mater.* 200 (1999) 405–424. doi:10.1016/S0304-8853(99)00429-1.
- [16] Z. Y. Zhang, M. G. Lagally, Atomistic processes in the early stages of thin-film growth, *Science* 276 (1997) 377–383. doi:10.1126/science.276.5311.377.
- [17] A. Rockett (Ed.), *Thin Film Growth Processes*, Springer US, Boston, MA, 2008. doi:10.1007/978-0-387-68650-9_10.
- [18] K. M. Krishnan, *Fundamentals and applications of magnetic materials*, first edition. Edition, Oxford University Press, Oxford, 2016.
- [19] A. Y. Cho, J. R. Arthur, Molecular beam epitaxy, *Prog. Solid State Chem.* 10 (1975) 157–191. doi:10.1016/0079-6786(75)90005-9.
- [20] K. Günther, Aufdampfschichten aus halbleitenden III-V-Verbindungen, *Z. Naturforsch.* 13a (1958) 1081–1089. doi:10.1007/BF00603228.
- [21] D. Mattox, *The Foundations of Vacuum Coating Technology*, Noyes / William Andrew Publishing, Norwich, 2003.
- [22] J. R. Arthur, Molecular beam epitaxy, *Surf. Sci.* 500 (2002) 189–217. doi:10.1016/S0039-6028(01)01525-4.
- [23] M. Hermann, H. Sitter, *Molecular Beam Epitaxy, Fundamentals and Current Status*, Springer Verlag Berlin Heidelberg, 1996.
- [24] A. Ichimiya, P. Cohen, *Reflection high-energy electron diffraction*, Cambridge University Press, Cambridge, UK, 2004.
- [25] A. Tempel, B. Schumann, Determination of lattice parameters at thin epitaxial layers by RHEED, *Krist. Tech.* 14 (1979) 571–574. doi:10.1002/crat.19790140510.
- [26] F. Imai, K. Kunimori, H. Nozoye, Performance characteristics of an oxygen radical beam radiofrequency source, *J. Vac. Sci. Technol., A* 13 (1995) 2508–2512. doi:10.1116/1.579495.
- [27] G. Scoles, *Atomic and molecular beam methods*, Vol. 1, Oxford University Press Inc, 1988.
- [28] Oxford Applied Research, *RF Atom Source HD25 Operation and Maintenance*.
- [29] R. Bunshah, *Deposition Technologies for Films and Coatings: Developments and Applications*, Vol. 1, Noyes Publications, 1982.
- [30] H. Wilsch, Remark on Cooling of Atomic Hydrogen Beams, *J. Chem. Phys.* 56 (1972) 1412–1413. doi:10.1063/1.1677379.
- [31] W. Crookes, On Electrical Evaporation, *Proc. R. Soc. London* 50 (1891) 88–105. doi:10.1098/rsp1.1891.0009.
- [32] S. Swann, Magnetron sputtering, *Physics in Technology* 19 (1988) 67.
- [33] K. Seshan (Ed.), *Handbook of Thin-Film Deposition Processes and Techniques*, 2nd Edition, Noyes Publications / William Andrew Publishing, Norwich, 2002.
- [34] F. Penning, Die Glimmentladung bei niedrigem Druck zwischen koaxialen Zylindern in einem axialen Magnetfeld, *Physica* 3 (1936) 873–894. doi:10.1016/S0031-8914(36)80313-9.

-
- [35] W. H. Bragg, W. L. Bragg, The Reflection of X-rays by Crystals, *Proc. Royal Soc. A* 88 (1913) 428–438. doi:10.1098/rspa.1913.0040.
- [36] B. D. Cullity, *Elements of X-Ray Diffraction*, Addison-Wesley Publishing Company, Reading, Massachusetts, 1956.
- [37] A. Snigirev, I. Snigireva, V. Kohn, S. Kuznetsov, I. Schelokov, On the possibilities of xray phase contrast microimaging by coherent highenergy synchrotron radiation, *Rev. Sci. Instrum.* 66 (1995) 5486–5492. doi:10.1063/1.1146073.
- [38] L. G. Parratt, Surface Studies of Solids by Total Reflection of X-Rays, *Phys. Rev.* 95 (1954) 359–369. doi:10.1103/PhysRev.95.359.
- [39] L. Névet, P. Croce, Caractérisation des surfaces par réflexion rasante de rayons X. Application à l'étude du polissage de quelques verres silicates, *Rev. Phys. Appl. (Paris)* 15 (1980) 761–779.
- [40] R. C. Jaklevic, J. Lambe, A. H. Silver, J. E. Mercereau, Quantum Interference Effects in Josephson Tunneling, *Phys. Rev. Lett.* 12 (1964) 159–160. doi:10.1103/PhysRevLett.12.159.
- [41] R. L. Fagaly, Superconducting quantum interference device instruments and applications, *Rev. Sci. Instrum.* 77 (2006) 45. doi:10.1063/1.2354545.
- [42] J. Clarke, B. A.I. (Eds.), *The SQUID Handbook: Fundamentals and Technology of SQUIDs and SQUID Systems*, Vol. 1, Wiley-VCH Verlag GmbH & Co. KGaA, Weinheim, 2006.
- [43] D. Mattis, *The Theory of Magnetism*, Harper& Row, New York, 1965.
- [44] M. Prasad, S. S. Dharmatti, H. V. Amin, Diamagnetic susceptibilities of magnesium and zinc ions, *Proc. Math. Sci* 26 (1947) 312–327.
- [45] J. D. McClelland, J. J. Donoghue, The Effect of Neutron Bombardment Upon the Magnetic Susceptibility of Several Pure Oxides, *J. Appl. Phys.* 24 (1953) 963–963. doi:10.1063/1.1721423.
- [46] E. F. Herroun, E. Wilson, On the Magnetic Susceptibility of Certain Natural and Artificial Oxides, *Proc. Phys. Soc. London* 33 (1920) 196. doi:10.1088/1478-7814/33/1/318.
- [47] P. Weiss, La variation du ferromagnétisme avec la température, *C. R. Hebd. Seances Acad. Sci.* 143 (1906) 1136–1149.
- [48] S. Blundell, *Magnetism in Condensed Matter*, Oxford University Press Inc., New York, 2001.
- [49] J. Crangle, G. M. Goodman, The Magnetization of Pure Iron and Nickel, *Proc. R. Soc. London, Ser. A* 321 (1971) 477–491. doi:10.1103/PhysRevB.69.144402.
- [50] A. J. P. Meyer, P. Taglang, Sur les moments magnétiques et points de curie des variétés hexagonale et cubique du cobalt, *C. R. Hebd. Seances Acad. Sci.* 231 (1950) 612–614.
- [51] P. Bruno, Tight-binding approach to the orbital magnetic moment and magnetocrystalline anisotropy of transition-metal monolayers, *Phys. Rev. B* 39 (1989) 865–868. doi:10.1103/PhysRevB.39.865.
- [52] L. Néel, Anisotropie magnétique superficielle et surstructures d'orientation, *J. Phys. Radium* 15 (1954) 225–239. doi:10.1051/jphysrad:01954001504022500.
- [53] G. M. Williams, A. S. Pavlovic, The Magnetostriction Behavior of Iron Single Crystals, *J. Appl. Phys.* 39 (1968) 571–572. doi:10.1063/1.2163525.

-
- [54] T. Hinomura, S. Nasu, A study of Fe-N alloy systems, *Hyperfine Interact.* 111 (1998) 221–226. doi:10.1023/a:1012614019538.
- [55] L. Rissanen, M. Neubauer, K. P. Lieb, P. Schaaf, The new cubic iron-nitride phase FeN prepared by reactive magnetron sputtering, *J. Alloys Compd.* 274 (1998) 74–82. doi:10.1016/S0925-8388(98)00594-5.
- [56] H. Nakagawa, S. Nasu, H. Fujii, M. Takahashi, F. Kanamaru, ^{57}Fe Mössbauer study of FeN_x ($x = 0.25 \approx 0.91$) alloys, *Hyperfine Interact.* 69 (1992) 455–458. doi:10.1007/bf02401863.
- [57] Y. Yamada, R. Usui, Y. Kobayashi, Mössbauer study of gamma''-iron nitride film, *Hyperfine Interact.* 219 (2013) 13–17. doi:10.1007/s10751-012-0664-x.
- [58] Y. Kong, Electronic structure and magnetism of equiatomic FeN, *J. Phys.: Condens. Matter* 12 (2000) 4161. doi:10.1088/0953-8984/12/18/302.
- [59] J. Theerthagiri, S. B. Dalavi, M. M. Raja, R. N. Panda, Magnetic properties of nanocrystalline $\epsilon\text{-Fe}_3\text{N}$ and Co_4N phases synthesized by newer precursor route, *Mater. Res. Bull.* 48 (2013) 4444–4448. doi:10.1016/j.materresbull.2013.07.043.
- [60] M. Robbins, J. G. White, Magnetic properties of epsilon-iron nitride, *J Phys Chem Solids* 25 (1964) 717–720. doi:10.1016/0022-3697(64)90182-9.
- [61] K. H. Eickel, W. Pitsch, Magnetic Properties of the Hexagonal Iron Nitride $\epsilon\text{-Fe}_{3.2}\text{N}$, *Phys. Status Solidi B* 39 (1970) 121–129. doi:10.1002/pssb.19700390113.
- [62] A. Leineweber, H. Jacobs, F. Hüning, H. Lueken, W. Kockelmann, Nitrogen ordering and ferromagnetic properties of $\epsilon\text{-Fe}_3\text{N}_{1+x}$ ($0.10 \leq x \leq 0.39$) and $\epsilon\text{-Fe}_3(\text{N}_{0.80}\text{C}_{0.20})_{1.38}$, *J. Alloys Compd.* 316 (2001) 21–38. doi:10.1016/S0925-8388(00)01435-3.
- [63] J. L. Costa-Kramer, D. M. Borsa, J. M. Garcia-Martin, M. S. Martin-Gonzalez, D. O. Boerma, F. Briones, Structure and magnetism of single-phase epitaxial $\gamma'\text{-Fe}_4\text{N}$, *Phys. Rev. B* 69 (2004) 8. doi:10.1103/PhysRevB.69.144402.
- [64] C. Guillaud, H. Creveaux, Préparation et propriétés magnétiques du composé défini Fe_4N , *C. R. Hebd. Seances Acad. Sci.* 222 (1946) 1170–1172.
- [65] K. H. Jack, The Occurrence and the Crystal Structure of α'' -Iron Nitride; a New Type of Interstitial Alloy Formed during the Tempering of Nitrogen-Martensite, *Proc. R. Soc. London, Ser. A* 208 (1951) 216–224. doi:10.1098/rspa.1951.0155.
- [66] K. H. Jack, The Iron-Nitrogen System: The Preparation and the Crystal Structures of Nitrogen-Austenite (γ) and Nitrogen-Martensite (α'), *Proc. R. Soc. London, Ser. A* 208 (1951) 200–215. doi:10.1098/rspa.1951.0154.
- [67] E. H. D. Van Voorthuysen, N. C. Chechenin, D. O. Boerma, Low-temperature extension of the Lehrer diagram and the iron-nitrogen phase diagram, *Metall. Mater. Trans. A* 33 (2002) 2593–2598. doi:10.1007/s11661-002-0380-2.
- [68] H. A. Wriedt, N. A. Gokcen, R. H. Nafziger, The Fe-N (Iron-Nitrogen) system, *Bull. Alloy Phase Diagr.* 8 (1987) 355–377. doi:10.1007/bf02869273.
- [69] M. Widenmeyer, L. Shlyk, A. Senyshyn, R. Mönig, R. Niewa, Structural and Magnetic Characterization of Single-phase Sponge-like Bulk $\alpha''\text{-Fe}_{16}\text{N}_2$, *Z. Anorg. Allg. Chem.* 641 (2) (2015) 348–354. doi:10.1002/zaac.201500013.

-
- [70] S. Matar, The magnetic properties of iron nitride: Fe_8N , *Z. Phys. B. Cond. Mat.* 87 (1992) 91–96. doi:10.1007/bf01308262.
- [71] T. Kim, M. Takahashi, New magnetic material having ultrahigh magnetic moment, *Appl. Phys. Lett.* 20 (1972) 492–494. doi:10.1063/1.1654030.
- [72] A. Kano, N. S. Kazama, H. Fujimori, T. Takahashi, Metastable Fe Nitrides with High-Bs prepared by reactive sputtering, *J. Appl. Phys.* 53 (1982) 8332–8334. doi:10.1063/1.330356.
- [73] A. Morisako, K. Takahashi, M. Matsumoto, M. Nace, Iron nitride thin-films prepared by facing targets sputtering, *J. Appl. Phys.* 63 (1988) 3230–3232. doi:10.1063/1.340851.
- [74] K. Umeda, E. Kita, A. Tasaki, Magnetic properties of iron nitride thin films with high corrosion-resistance, *IEEE Trans. Magn.* 22 (1986) 591–593. doi:10.1109/tmag.1986.1064580.
- [75] T. Tanaka, A. Kodama, M. Takahashi, T. Wakiyama, S. Iizuka, R. Hatakeyama, N. Sato, Fe-N by CVD, 14th Conf. Mag. Soc. Jpn. IlaC-10 (1990) –.
- [76] M. Komuro, Y. Kozono, M. Hanazono, Y. Sugita, Epitaxial growth and magnetic properties of Fe_{16}N_2 films with high saturation magnetic flux density, *J. Appl. Phys.* 67 (1990) 5126–5130. doi:10.1063/1.344689.
- [77] Y. Sugita, K. Mitsuoka, M. Komuro, H. Hoshiya, Y. Kozono, M. Hanazono, Giant magnetic moment and other magnetic properties of epitaxially grown Fe_{16}N_2 single-crystal films, *J. Appl. Phys.* 70 (1991) 5977–5982. doi:10.1063/1.350067.
- [78] C. D. G. Jr., Anisotropy Constants of Iron and IronSilicon Alloys at Room Temperature and Below, *J. Appl. Phys.* 30 (1959) S317–S317. doi:10.1063/1.2185952.
- [79] K. Nakajima, S. Okamoto, Large magnetization induced in single crystalline iron films by highdose nitrogen implantation, *Appl. Phys. Lett.* 56 (1990) 92–94. doi:10.1063/1.102614.
- [80] Y. Otani, H. Miyajima, S. Chikazumi, Magnetocrystalline anisotropy in Nd-Fe-B magnet, *J. Appl. Phys.* 61 (1987) 3436–3438. doi:10.1063/1.338745.
- [81] B. T. Shirk, W. R. Buessem, Temperature Dependence of M_s and K_1 of $\text{BaFe}_{12}\text{O}_{19}$ and $\text{SrFe}_{12}\text{O}_{19}$ Single Crystals, *J. Appl. Phys.* 40 (1969) 1294–1296. doi:10.1063/1.1657636.
- [82] A. Sakuma, Self-consistent calculations for the electronic-structures of iron nitrides, Fe_3N , Fe_4N , and Fe_{16}N_2 , *J. Magn. Magn. Mater.* 102 (1991) 127–134. doi:10.1016/0304-8853(91)90277-h.
- [83] B. I. Min, Enhancement of Fe magnetic moments in ferromagnetic Fe_{16}N_2 , *Phys. Rev. B* 46 (1992) 8232–8236. doi:10.1103/PhysRevB.46.8232.
- [84] V. L. Moruzzi, P. M. Marcus, K. Schwarz, P. Mohn, Ferromagnetic phases of bcc and fcc Fe, Co, and Ni, *Phys. Rev. B* 34 (1986) 1784–1791. doi:10.1103/PhysRevB.34.1784.
- [85] Y. F. Chen, Q. G. Song, H. Y. Yan, T. Wei, X. Yang, Volume dependence of electronic structure and magnetic properties of Fe_{16}N_2 , *Physica B* 407 (2012) 519–522. doi:10.1016/j.physb.2011.11.027.
- [86] H. Sims, W. H. Butler, M. Richter, K. Koepernik, E. Sasioglu, C. Friedrich, S. Blugel, Theoretical investigation into the possibility of very large moments in Fe_{16}N_2 , *Phys. Rev. B* 86 (2012) 7. doi:10.1103/PhysRevB.86.174422.

-
- [87] K. Mitsuoka, H. Miyajima, H. Ino, S. Chikazumi, Induced Magnetic Moment in Ferromagnetic Fe Alloys by Tetragonally Elongated Lattice Expansion, *J. Phys. Soc. Jpn.* 53 (1984) 2381–2390. doi:10.1143/jpsj.53.2381.
- [88] M. Takahashi, H. Shoji, H. Takahashi, H. Nashi, T. Wakiyama, M. Matsui, Magnetic moment of α'' -Fe₁₆N₂ films, *J. Appl. Phys.* 76 (1994) 6642–6647. doi:10.1063/1.358431.
- [89] S. Okamoto, O. Kitakami, Y. Shimada, Characterization of epitaxially grown Fe-N films by sputter beam method, *J. Appl. Phys.* 79 (1996) 1678–1683. doi:10.1063/1.361421.
- [90] X. W. Zhang, Y. F. Jiang, M. Y. Yang, L. F. Allard, J. P. Wang, High Ms Fe₁₆N₂ thin film with Ag under layer on GaAs substrate, *AIP Adv.* 6 (2016) 5. doi:10.1063/1.4943236.
- [91] N. Ji, Y. M. Wu, J. P. Wang, Epitaxial high saturation magnetization FeN thin films on Fe(001) seeded GaAs(001) single crystal wafer using facing target sputterings, *J. Appl. Phys.* 109 (2011) 07B767. doi:10.1063/1.3565403.
- [92] N. A. Ji, L. F. Allard, E. Lara-Curzio, J. P. Wang, N site ordering effect on partially ordered Fe₁₆N₂, *Appl. Phys. Lett.* 98 (2011) 092506. doi:10.1063/1.3560051.
- [93] J. P. Wang, N. Ji, X. Q. Liu, Y. H. Xu, C. Sanchez-Hanke, Y. M. Wu, F. M. F. de Groot, L. F. Allard, E. Lara-Curzio, Fabrication of Fe₁₆N₂ Films by Sputtering Process and Experimental Investigation of Origin of Giant Saturation Magnetization in Fe₁₆N₂, *IEEE Trans. Magn.* 48 (2012) 1710–1717. doi:10.1109/tmag.2011.2170156.
- [94] X. W. Zhang, N. A. Ji, V. Lauter, H. Ambaye, J. P. Wang, Strain effect of multilayer FeN structure on GaAs substrate, *J. Appl. Phys.* 113 (2013) 17E149. doi:10.1063/1.4800086.
- [95] N. Ji, V. Lauter, C.-J. Sun, L. F. Allard, H. Ambaye, S. M. Heald, E. Lara-Curzio, X. Liu, Y. Xu, X. Li, Direct Observation of Giant Saturation Magnetization in Fe₁₆N₂, arXiv preprint arXiv:1211.0553.
- [96] H. Jiang, K. Tao, H. Li, The thermostability of the Fe₁₆N₂ phase deposited on a GaAs substrate by ion-beam-assisted deposition, *J. Phys.: Condens. Matter* 6 (1994) L279. doi:10.1088/0953-8984/6/18/004.
- [97] S. Higashikozono, K. Ito, F. Takata, T. Gushi, K. Toko, T. Suemasu, Highly oriented epitaxial ($\alpha'' + \alpha'$)-Fe₁₆N₂ films on α -Fe(001) buffered MgAl₂O₄(001) substrates and their magnetization, *J. Cryst. Growth* 468 (2017) 691–695. doi:10.1016/j.jcrysgro.2016.11.048.
- [98] M. Komuro, Y. Kozono, M. Hanazono, Y. Sugita, Structures and Saturation Magnetic Flux Density of Epitaxially Grown Fe and Fe-N Films on GaAs (100), *J. Magn. Soc. Jpn.* 13 (1989) 301–306. doi:10.3379/jmsjmag.13.301.
- [99] Y. Sugita, H. Takahashi, M. Komuro, M. Igarashi, R. Imura, T. Kambe, Magnetic and electrical properties of single-phase, single-crystal Fe₁₆N₂ films epitaxially grown by molecular beam epitaxy (invited), *J. Appl. Phys.* 79 (1996) 5576–5581. doi:10.1063/1.362246.
- [100] O. Kohmoto, S. Okamoto, O. Kitakami, Y. Shimada, T. Tsuda, Ferromagnetic resonance in epitaxial α' -martensite Fe-N films, *Jpn. J. Appl. Phys.* 1 36 (1997) 4305–4306. doi:10.1143/jjap.36.4305.
- [101] S. Okamoto, O. Kitakami, Y. Shimada, α'' -Fe₁₆N₂ phase epitaxially grown by sputter beam method, *J. Appl. Phys.* 79 (1996) 5250–5252. doi:10.1063/1.361301.

-
- [102] S. Okamoto, O. Kitakami, Y. Shimada, Effect of lattice distortion on magnetic and electronic state of Fe_{16}N_2 , *J. Appl. Phys.* 85 (1999) 4952–4954. doi:10.1063/1.370056.
- [103] S. Okamoto, O. Kitakami, Y. Shimada, Crystal distortion and the magnetic moment of epitaxially grown $\alpha''\text{-Fe}_{16}\text{N}_2$, *J. Magn. Magn. Mater.* 208 (2000) 102–114. doi:10.1016/s0304-8853(99)00556-9.
- [104] X. Z. Ding, F. M. Zhang, J. S. Yan, H. L. Shen, X. Wang, X. H. Liu, D. F. Shen, Synthesis and magnetic properties of iron nitride films deposited on Ge (100) by reactive ion beam sputtering, *J. Appl. Phys.* 82 (1997) 5154–5158. doi:10.1063/1.366319.
- [105] X. Z. Ding, F. M. Zhang, Y. L. Sun, Z. Y. Zhou, X. Wang, X. H. Liu, D. F. Shen, Thermal stability studies on ion beam sputter deposited substoichiometric iron nitride thin films, *Surf. Coat. Technol.* 91 (1997) 215–219. doi:10.1016/s0257-8972(97)00001-7.
- [106] S. Iwatsubo, M. Naoe, Magnetic characteristics of Fe-N films prepared by reactive ion beam sputtering with a nitrogen bombardment process, *J. Appl. Phys.* 87 (2000) 5245–5247. doi:10.1063/1.373309.
- [107] Y. Utsushikawa, K. Niizuma, The saturation magnetization of Fe-N films prepared by nitriding treatment in N_2 plasma, *J. Alloys Compd.* 222 (1995) 188–192. doi:10.1016/0925-8388(94)04915-7.
- [108] X. Wang, W. T. Zheng, H. W. Tian, S. S. Yu, W. Xu, S. H. Meng, X. D. He, J. C. Han, C. Q. Sun, B. K. Tay, Growth, structural, and magnetic properties of iron nitride thin films deposited by dc magnetron sputtering, *Appl. Surf. Sci.* 220 (2003) 30–39. doi:10.1016/s0169-4332(03)00752-9.
- [109] C. Gao, W. Doyle, M. Shamsuzzoha, Quantitative correlation of phase structure with the magnetic moment in rf sputtered Fe-N films, *J. Appl. Phys.* 73 (1993) 6579–6581. doi:10.1063/1.352570.
- [110] H. Takahashi, K. Mitsuoka, M. Komuro, Y. Sugita, Ferromagnetic-resonance studies of Fe_{16}N_2 films with a giant magnetic-moment, *J. Appl. Phys.* 73 (1993) 6060–6062. doi:10.1063/1.353469.
- [111] H. Takahashi, M. Igarashi, A. Kaneko, H. Miyajima, Y. Sugita, Perpendicular uniaxial magnetic anisotropy of $\text{Fe}_{16}\text{N}_2(001)$ single crystal films grown by molecular beam epitaxy, *IEEE Trans. Magn.* 35 (1999) 2982–2984. doi:10.1109/20.801054.
- [112] H. Takahashi, M. Igarashi, A. Sakuma, Y. Sugita, Chemical shift of the nitrogen electrons in $\text{Fe}_{16}\text{N}_2(001)$ single crystal films epitaxially grown by molecular beam epitaxy, *IEEE Trans. Magn.* 36 (2000) 2921–2923. doi:10.1109/20.908628.
- [113] Y. Sugita, H. Takahashi, M. Komuro, K. Mitsuoka, A. Sakuma, Magnetic and Mössbauer studies of single-crystal Fe_{16}N_2 and Fe-N martensite films epitaxially grown by molecular beam epitaxy (invited), *J. Appl. Phys.* 76 (1994) 6637–6641. doi:10.1063/1.358157.
- [114] Y. Takahashi, M. Katou, H. Shoji, M. Takahashi, Effect of oxygen on the formation of Fe_{16}N_2 sputtered films, *J. Magn. Magn. Mater.* 232 (2001) 18–26. doi:10.1016/s0304-8853(01)00204-9.
- [115] H. Shoji, H. Nashi, K. Eguchi, M. Takahashi, An experimental trial for the synthesis of $\alpha''\text{-}(\text{Fe}_{100-x}\text{Co}_x)_{16}\text{N}_2$ ($x=0\text{-}30$) martensite films by reactive sputtering, *J. Magn. Magn. Mater.* 162 (1996) 202–210. doi:10.1016/s0304-8853(96)00276-4.
- [116] M. Takahashi, H. Takahashi, H. Nashi, H. Shoji, T. Wakiyama, M. Kuwabara, Structure and magnetic moment of Fe_{16}N_2 compound films: Effect of Co and H on phase formation (invited), *J. Appl. Phys.* 79 (1996) 5564–5569. doi:10.1063/1.362244.

-
- [117] H. Takahashi, H. Shoji, M. Takahashi, Structure and magnetic moment of Fe₁₆N₂ sputtered film, *J. Magn. Magn. Mater.* 174 (1997) 57–69. doi:10.1016/s0304-8853(97)00213-8.
- [118] M. Yang, L. F. Allard, N. Ji, X. Zhang, G. H. Yu, J. P. Wang, The effect of strain induced by Ag underlayer on saturation magnetization of partially ordered Fe₁₆N₂ thin films, *Appl. Phys. Lett.* 103 (2013) 242412. doi:10.1063/1.4847315.
- [119] N. Ji, V. Lauter, X. W. Zhang, H. Ambaye, J. P. Wang, Strain induced giant magnetism in epitaxial Fe₁₆N₂ thin film, *Appl. Phys. Lett.* 102 (2013) 072411. doi:10.1063/1.4792706.
- [120] H. Shinno, M. Uehara, K. Saito, Synthesis of α'' -Fe₁₆N₂ iron nitride by means of nitrogen-ion implantation into iron thin films, *Journal of materials science* 32 (1997) 2255–2261. doi:10.1023/A:1018568015538.
- [121] J. L. Menendez, G. Armelles, A. Cebollada, F. Briones, F. Peiro, F. Guell, A. Cornet, M. L. F. Gubieda, J. Gutierrez, C. Meyer, Nitrogen incorporation effects in Fe(001) thin films, *J. Appl. Phys.* 89 (2001) 6314–6319. doi:10.1063/1.1368398.
- [122] Z. W. Li, A. H. Morrish, C. Ortiz, Mössbauer studies of α'' -Fe₁₆N₂ and α' -Fe₈N films, *J. Mater. Sci.* 36 (2001) 5835–5838. doi:10.1023/a:1012912323318.
- [123] I. Dirba, P. Komissinskiy, O. Gutfleisch, L. Alff, Increased magnetic moment induced by lattice expansion from α -Fe to α' -Fe₈N, *J. Appl. Phys.* 117 (2015) 5. doi:10.1063/1.4919601.
- [124] H. Zhang, I. Dirba, T. Helbig, L. Alff, O. Gutfleisch, Engineering perpendicular magnetic anisotropy in Fe via interstitial nitrogenation: N choose K, *APL Mater.* 4 (2016) 6. doi:10.1063/1.4967285.
- [125] C. Ortiz, G. Dumpich, A. H. Morrish, Epitaxial Fe₁₆N₂ films grown by sputtering, *Appl. Phys. Lett.* 65 (1994) 2737–2739. doi:10.1063/1.112552.
- [126] D. C. Sun, E. Y. Jiang, M. B. Tian, C. Lin, X. X. Zhang, Epitaxial single crystal Fe₁₆N₂ films grown by facing targets sputtering, *J. Appl. Phys.* 79 (1996) 5440–5442. doi:10.1063/1.361843.
- [127] S. Atiq, H. S. Ko, S. A. Siddiqi, S. C. Shin, Preparation and the influence of Co, Pt and Cr additions on the saturation magnetization of α'' -Fe₁₆N₂ thin films, *J. Alloys Compd.* 479 (2009) 755–758. doi:10.1016/j.jallcom.2009.01.041.
- [128] H. M. Du, P. Wu, E. Y. Jiang, Z. Q. Li, C. Zhao, H. L. Bai, The influence of experimental procedures on the structural and magnetic properties of RF sputtered Fe-N thin films, *J. Magn. Magn. Mater.* 292 (2005) 227–233. doi:10.1016/j.jmmm.2004.10.115.
- [129] X. Liu, Y.-H. Xu, C. Sanchez-Hanke, J.-P. Wang, Discovery of localized states of Fe 3d electrons in Fe₁₆N₂ and Fe₈N films: an evidence of the existence of giant saturation magnetization, arXiv preprint arXiv:0909.4478.
- [130] Y. F. Jiang, J. M. Liu, P. K. Suri, G. Kennedy, N. N. Thadhani, D. J. Flannigan, J. P. Wang, Preparation of an α'' -Fe₁₆N₂ Magnet via a Ball Milling and Shock Compaction Approach, *Adv. Eng. Mater.* 18 (2016) 1009–1016. doi:10.1002/adem.201500455.
- [131] Y. F. Jiang, V. Dabade, M. P. Brady, O. Rios, R. D. James, J. P. Wang, 9 T high magnetic field annealing effects on FeN bulk sample, *J. Appl. Phys.* 115 (2014) 17A758. doi:10.1063/1.4868493.
- [132] Y. F. Jiang, M. Al Mehedi, E. G. Fu, Y. Q. Wang, J. P. Wang, FeN foils by nitrogen ion-implantation, *J. Appl. Phys.* 115 (2014) 3. doi:10.1063/1.4868492.

-
- [133] Y. F. Jiang, M. Al Mehedi, E. G. Fu, Y. Q. Wang, L. F. Allard, J. P. Wang, Synthesis of Fe_{16}N_2 compound Free-Standing Foils with 20 MGOe Magnetic Energy Product by Nitrogen Ion-Implantation, *Sci. Rep.* 6 (2016) 7. doi:10.1038/srep25436.
- [134] K. Takagi, M. Akada, K. Ozaki, N. Kobayashi, T. Ogawa, Y. Ogata, M. Takahashi, High-pressure sintering behavior of $\alpha''\text{-Fe}_{16}\text{N}_2$ nanopowder, *J. Appl. Phys.* 115 (2014) 5. doi:10.1063/1.4868295.
- [135] D. Nagai, Y. Kinemuchi, K. Suzuki, A. Towata, M. Yasuoka, Highly dispersive $\alpha''\text{-Fe}_{16}\text{N}_2$ particle synthesis using hydroxyapatite coating, *J. Solid State Chem.* 225 (2015) 455–458. doi:10.1016/j.jssc.2015.01.024.
- [136] K. Yamanaka, Y. Onuma, S. Yamashita, Y. Masubuchi, T. Takeda, S. Kikkawa, Humidity effects in Fe_{16}N_2 fine powder preparation by low-temperature nitridation, *J. Solid State Chem.* 183 (2010) 2236–2241. doi:10.1016/j.jssc.2010.07.045.
- [137] J. Li, W. Yuan, X. L. Peng, Y. T. Yang, J. C. Xu, X. Q. Wang, B. Hong, H. X. Jin, D. F. Jin, H. L. Ge, Synthesis of fine $\alpha''\text{-Fe}_{16}\text{N}_2$ powders by low-temperature nitridation of alpha-Fe from magnetite nanoparticles, *AIP Adv.* 6 (2016) 5. doi:10.1063/1.4967950.
- [138] I. Dirba, C. A. Schwöbel, L. V. B. Diop, M. Duerrschabel, L. Molina-Luna, K. Hofmann, P. Komissinskiy, H. J. Kleebe, O. Gutfleisch, Synthesis, morphology, thermal stability and magnetic properties of $\alpha''\text{-Fe}_{16}\text{N}_2$ nanoparticles obtained by hydrogen reduction of $\gamma\text{-Fe}_2\text{O}_3$ and subsequent nitrogenation, *Acta Mater.* 123 (2017) 214–222. doi:10.1016/j.actamat.2016.10.061.
- [139] C. A. Bridges, O. Rios, L. F. Allard, H. M. Meyer, A. Huq, Y. Jiang, J. P. Wang, M. P. Brady, The impact of carbon coating on the synthesis and properties of $\alpha''\text{-Fe}_{16}\text{N}_2$ powders, *Phys. Chem. Chem. Phys.* 18 (2016) 13010–13017. doi:10.1039/c6cp00737f.
- [140] T. Ogawa, Y. Ogata, R. Gallage, N. Kobayashi, N. Hayashi, Y. Kusano, S. Yamamoto, K. Kohara, M. Doi, M. Takano, M. Takahashi, Challenge to the Synthesis of $\alpha''\text{-Fe}_{16}\text{N}_2$ Compound Nanoparticle with High Saturation Magnetization for Rare Earth Free New Permanent Magnetic Material, *Appl. Phys. Express* 6 (2013) 3. doi:10.7567/apex.6.073007.
- [141] E. Kita, K. Shibata, Y. Sasaki, M. Kishimoto, H. Yanagihara, Magnetic anisotropy in spherical Fe_{16}N_2 core-shell nanoparticles determined by torque measurements, *AIP Adv.* 7 (2017) 056212. doi:10.1063/1.4974276.
- [142] R. Zuhijah, A. B. D. Nandiyanto, T. Ogi, T. Iwaki, K. Nakamura, K. Okuyama, Effect of oxidation on $\alpha''\text{-Fe}_{16}\text{N}_2$ phase formation from plasma-synthesized spherical core-shell $\alpha\text{-Fe}/\text{Al}_2\text{O}_3$ nanoparticles, *J. Magn. Magn. Mater.* 381 (2015) 89–98. doi:10.1016/j.jmmm.2014.12.015.
- [143] W. E. Wallace, M. Q. Huang, Enhanced Fe Moment in Nitrogen Martensite and Fe_{16}N_2 (Invited), *J. Appl. Phys.* 76 (1994) 6648–6652. doi:10.1063/1.358158.
- [144] Y. F. Jiang, V. Dabade, L. F. Allard, E. Lara-Curzio, R. James, J. P. Wang, Synthesis of $\alpha''\text{-Fe}_{16}\text{N}_2$ Compound Anisotropic Magnet by the Strained-Wire Method, *Phys. Rev. Appl.* 6 (2016) 10. doi:10.1103/PhysRevApplied.6.024013.
- [145] I. Dirba, M. BaghaieYazdi, A. Radetinac, P. Komissinskiy, S. Flege, O. Gutfleisch, L. Alff, Growth, structure, and magnetic properties of $\gamma'\text{-Fe}_4\text{N}$ thin films, *J. Magn. Magn. Mater.* 379 (2015) 151–155. doi:10.1016/j.jmmm.2014.12.033.
- [146] R. Coehoorn, G. H. O. Daalderop, H. J. F. Jansen, Full-potential calculations of the magnetization of Fe_{16}N_2 and Fe_4N , *Phys. Rev. B* 48 (1993) 3830–3834. doi:10.1103/PhysRevB.48.3830.

-
- [147] B. C. Frazer, Magnetic Structure of Fe₄N, Phys. Rev. 112 (1958) 751–754. doi:10.1103/PhysRev.112.751.
- [148] W. Y. Lai, Q. Q. Zheng, W. Y. Hu, The giant magnetic-moment and electronic correlation effect in ferromagnetic nitride Fe₁₆N₂, J. Phys.-Condes. Matter 6 (1994) L259–L264. doi:10.1088/0953-8984/6/18/001.
- [149] K. Umino, H. Nakajima, K. Shiki, Self-interaction correction for band structure calculation based on local density approximation of iron nitrides, J. Magn. Magn. Mater. 153 (1996) 323–328. doi:10.1016/0304-8853(95)00547-1.
- [150] N. Ji, X. Liu, J. P. Wang, Theory of giant saturation magnetization in α'' -Fe₁₆N₂: role of partial localization in ferromagnetism of 3d transition metals, New J. Phys. 12 (2010) 063032. doi:10.1088/1367-2630/12/6/063032.
- [151] T. Sourmail, Near equiatomic FeCo alloys: Constitution, mechanical and magnetic properties, Prog. Mater. Sci. 50 (2005) 816–880. doi:10.1016/j.pmatsci.2005.04.001.
- [152] D. Gölden, E. Hildebrandt, L. Alff, Thin film phase diagram of iron nitrides grown by molecular beam epitaxy, J. Magn. Magn. Mater. 422 (2017) 407–411. doi:10.1016/j.jmmm.2016.07.074.
- [153] T. Burkert, O. Eriksson, P. James, S. I. Simak, B. Johansson, L. Nordström, Calculation of uniaxial magnetic anisotropy energy of tetragonal and trigonal Fe, Co, and Ni, Phys. Rev. B 69 (2004) 104426. doi:10.1103/PhysRevB.69.104426.
- [154] L. Q. Ke, K. D. Belashchenko, M. van Schilfgaarde, T. Kotani, V. P. Antropov, Effects of alloying and strain on the magnetic properties of Fe₁₆N₂, Phys. Rev. B 88 (2013) 9. doi:10.1103/PhysRevB.88.024404.
- [155] S. Yamamoto, R. Gallage, Y. Ogata, Y. Kusano, N. Kobayashi, T. Ogawa, N. Hayashi, K. Kohara, M. Takahashi, M. Takano, Quantitative understanding of thermal stability of α'' -Fe₁₆N₂, Chem. Commun. 49 (2013) 7708–7710. doi:10.1039/c3cc43590c.
- [156] K. H. Jack, The synthesis, structure, and characterization of α'' -Fe₁₆N₂ (invited), J. Appl. Phys. 76 (1994) 6620–6625. doi:10.1063/1.358482.
- [157] M. Widenmeyer, T. C. Hansen, R. Niewa, Formation and Decomposition of Metastable α'' -Fe₁₆N₂ from in situ Powder Neutron Diffraction and Thermal Analysis, Z. Anorg. Allg. Chem. 639 (2013) 2851–2859. doi:10.1002/zaac.201300379.
- [158] S. Hirosawa, M. Nishino, S. Miyashita, Perspectives for high-performance permanent magnets: applications, coercivity, and new materials, Adv. Nat. Sci: Nanosci. Nanotechnol. 8 (2017) 013002. doi:10.1088/2043-6254/aa597c.
- [159] M. A. Abdellateef, C. Heiden, H. Lemke, F. M. El-Hossary, K. Baerner, Magnetic properties and structure of the α'' -Fe₁₆N₂ films, J. Magn. Magn. Mater. 256 (2003) 214–220. doi:10.1016/S0304-8853(02)00479-1.
- [160] M. A. Brewer, C. J. Echer, K. M. Krishnan, T. Kobayashi, A. Nakanishi, Magnetic and physical microstructure of FeN films grown epitaxially on Si (001), J. Appl. Phys. 81 (1997) 4128. doi:10.1063/1.365102.
- [161] M. Hillert, The kinetics of the first stage of tempering, Acta Metall. 7 (1959) 653–658. doi:10.1016/0001-6160(59)90141-5.

-
- [162] F. S. Buffington, K. Hirano, M. Cohen, Self diffusion in iron, *Acta Metall.* 9 (1961) 434–439. doi:10.1016/0001-6160(61)90137-7.
- [163] R. Gupta, A. Gupta, W. Leitenberger, R. Ruffer, Mechanism of stress relaxation in nanocrystalline Fe-N thin films, *Phys. Rev. B* 85 (2012) 7. doi:10.1103/PhysRevB.85.075401.
- [164] A. Tayal, M. Gupta, D. Kumar, V. R. Reddy, A. Gupta, S. M. Amir, P. Korelis, J. Stahn, Correlation between iron self-diffusion and thermal stability in doped iron nitride thin films, *J. Appl. Phys.* 116 (2014) 8. doi:10.1063/1.4902962.
- [165] J. Huang, W. H. Xie, X. H. Li, The stability, magnetism and electronic structure of $\text{Fe}_{15}\text{TMN}_2$ and $\text{Fe}_{14}\text{TM}_2\text{N}_2$ (TM=Cr, Mn, Co, and Ni), *J. Magn. Magn. Mater.* 364 (2014) 1–4. doi:10.1016/j.jmmm.2014.03.078.
- [166] H. Y. Wang, E. Y. Jiang, Enhancement of the thermal stability of Fe_{16}N_2 by Ti addition, *J. Phys.-Condes. Matter* 9 (1997) 2739–2743. doi:10.1088/0953-8984/9/13/011.
- [167] E. Bain, *Functions of the Alloying elements in steel*, ASM Cleveland, Ohio, 1939.
- [168] M. Reibold, A. A. Levin, D. C. Meyer, P. Paufler, W. Kochmann, Microstructure of a Damascene sabre after annealing, *Int. J. Mater. Res.* 97 (2006) 1172–1182. doi:10.3139/146.101355.
- [169] H. Jacobs, D. Rechenbach, U. Zachwieja, Structure determination of γ' - Fe_4N and ϵ - Fe_3N , *J. Alloys Compd.* 227 (1995) 10–17. doi:10.1016/0925-8388(95)01610-4.
- [170] M. Tsunoda, R. Chiba, K. Kabara, Fabrication of MgAl_2O_4 tunnel barrier by radio frequency-sputtering method and magnetoresistance effect through it with Fe or Fe_4N ferromagnetic electrode, *J. Appl. Phys.* 117 (17) (2015) 17D703. doi:10.1063/1.4906762.
- [171] J. G. Wright, Ferromagnetism in epitaxial F.C.C. iron films, *Philos. Mag.* 24 (1971) 217–223. doi:10.1080/14786437108227381.
- [172] S. Atiq, H. S. Ko, S. A. Siddiqi, S. C. Shin, Effect of epitaxy and lattice mismatch on saturation magnetization of γ' - Fe_4N thin films, *Appl. Phys. Lett.* 92 (2008) 3. doi:10.1063/1.2940599.
- [173] H. Xiang, F. Y. Shi, M. S. Rzechowski, P. M. Voyles, Y. A. Chang, Epitaxial growth and thermal stability of Fe_4N film on TiN buffered Si(001) substrate, *J. Appl. Phys.* 109 (2011) 3. doi:10.1063/1.3556919.
- [174] J. Evertsson, F. Bertram, F. Zhang, L. Rullik, L. R. Merte, M. Shipilin, M. Soldemo, S. Ahmadi, N. Vinogradov, F. Carlà, J. Weissenrieder, M. Göthelid, J. Pan, A. Mikkelsen, J. O. Nilsson, E. Lundgren, The thickness of native oxides on aluminum alloys and single crystals, *Appl. Surf. Sci.* 349 (2015) 826–832. doi:10.1016/j.apsusc.2015.05.043.
- [175] F. E. Hoare, J. C. Walling, An Absolute Measurement of the Susceptibility of Tantalum and other Metals, *Proc. Phys. Soc., B* 64 (1951) 337. doi:10.1088/0370-1301/64/4/306.
- [176] D. Ricci, C. Di Valentin, G. Pacchioni, P. V. Sushko, A. L. Shluger, E. Giamello, Paramagnetic defect centers at the MgO surface. An alternative model to oxygen vacancies, *J. Am. Chem. Soc.* 125 (2003) 738–47. doi:10.1021/ja0282240.
- [177] M. D. Kuzmin, Shape of Temperature Dependence of Spontaneous Magnetization of Ferromagnets: Quantitative Analysis, *Phys. Rev. Lett.* 94 (2005) 107204. doi:10.1103/PhysRevLett.94.107204.
- [178] C. Loong, J. M. Carpenter, J. W. Lynn, R. A. Robinson, H. A. Mook, Neutron scattering study of the magnetic excitations in ferromagnetic iron at high energy transfers, *J. Appl. Phys.* 55 (1984) 1895–1897. doi:10.1063/1.333511.

-
- [179] C. Guillaud, Variation thermique de l'aimantation spontanée, C. R. Hebd. Seances Acad. Sci. 223 (1946) 1110–1112.
- [180] L. Vegard, Die Konstitution der Mischkristalle und die Raumfüllung der Atome, Zeitschrift für Physik 5 (1921) 17–26. doi:10.1007/bf01349680.
- [181] C. T. Chen, Y. U. Idzerda, H. J. Lin, N. V. Smith, G. Meigs, E. Chaban, G. H. Ho, E. Pellegrin, F. Sette, Experimental Confirmation of the X-Ray Magnetic Circular Dichroism Sum Rules for Iron and Cobalt, Phys. Rev. Lett. 75 (1995) 152–155. doi:10.1103/PhysRevLett.75.152.
- [182] J. Lau, A. Föhlich, R. Nietubyè, M. Reif, W. Wurth, Size-Dependent Magnetism of Deposited Small Iron Clusters Studied by X-Ray Magnetic Circular Dichroism, Phys. Rev. Lett. 89 (2002) 057201. doi:10.1103/PhysRevLett.89.057201.
- [183] H. Swanson, N. B. of Standards(U.S.), Standard x-ray diffraction powder patterns, U.S. Dept. of Commerce, National Bureau of Standards, U.S. G.P.O., Washington, DC, 1953.
- [184] H. Sawada, A. Nogami, T. Matsumiya, T. Oguchi, Structural, electronic, and magnetic properties of Fe₁₆N₂, Phys. Rev. B 50 (1994) 10004–10008. doi:10.1103/PhysRevB.50.10004.
- [185] J. Zhou, H. Wang, The physical meanings of 5 basic parameters for an X-ray diffraction peak and their application, Chin. J. Geochem. 22 (2003) 38–44. doi:10.1007/BF02831544.
- [186] L. Zwell, G. R. Speich, W. C. Leslie, Effects of Co, Cr, Ir, Pt, Re, Rh, and Ru on the lattice parameter and density of alpha iron, Metall. Trans. 4 (1973) 1990–1992. doi:10.1007/BF02665429.
- [187] N. Ridley, H. Stuart, Lattice parameter anomalies at the Curie point of pure iron, J. Phys. D: Appl. Phys. 1 (1968) 1291. doi:10.1088/0022-3727/1/10/308.
- [188] G. Suresh, D. Rajan Babu, A simple wet-chemical approach to synthesize shape controlled high magnetic moment Fe₇₁Co₂₉ nanocrystals, J. Alloys Compd. 509 (2011) 10145–10149. doi:10.1016/j.jallcom.2011.08.064.
- [189] H. S. Jung, W. D. Doyle, S. Matsunuma, Influence of underlayers on the soft properties of high magnetization FeCo films, J. Appl. Phys. 93 (2003) 6462–6464. doi:10.1063/1.1557653.
- [190] J. W. Shih, Magnetic Properties of Iron-Cobalt Single Crystals, Phys. Rev. 46 (1934) 139–142. doi:10.1103/PhysRev.46.139.
- [191] X. Zhao, C. Z. Wang, Y. X. Yao, K. M. Ho, Large magnetic anisotropy predicted for rare-earth-free Fe_{16-x}Co_xN₂ alloys, Phys. Rev. B 94 (2016) 5. doi:10.1103/PhysRevB.94.224424.
- [192] K. Oda, T. Yoshio, K. Oda, Preparation of Co-N films by rf-sputtering, J. Mater. Sci. 22 (1987) 2729–2733. doi:10.1007/bf01086464.
- [193] H. Ohtsuka, V. A. Dinh, T. Ohno, K. Tsuzaki, K. Tsuchiya, R. Sahara, H. Kitazawa, T. Nakamura, First-principles Calculation of Effects of Carbon on Tetragonality and Magnetic Moment in Fe-C System, ISIJ Int. 55 (2015) 2483–2491. doi:10.2355/isijinternational.ISIJINT-2015-276.
- [194] T. Van Rompaey, K. C. H. Kumar, P. Wollants, Thermodynamic optimization of the B-Fe system, J. Alloys Compd. 334 (2002) 173–181. doi:10.1016/s0925-8388(01)01777-7.
- [195] D. H. R. Fors, G. Wahnström, Nature of boron solution and diffusion in α -iron, Phys. Rev. B 77 (2008) 4. doi:10.1103/PhysRevB.77.132102.
- [196] S. S. Baik, B. I. Min, S. K. Kwon, Y. M. Koo, Boron solution and distribution in α -Fe: Application to boron steel, Phys. Rev. B 81 (2010) 7. doi:10.1103/PhysRevB.81.144101.

-
- [197] W. R. Thomas, G. M. Leak, Condition of Boron in Alpha Iron, *Nature* 176 (1955) 29–31. doi:10.1038/176029b0.
- [198] T. B. Cameron, J. E. Morral, The solubility of boron in iron, *Metall. Trans. A* 17 (1986) 1481–1483. doi:10.1007/bf02650132.
- [199] P. M. Strocchi, B. A. Melandri, A. Tamba, On the nature of boron solid solution in α -iron, II *Nuovo Cimento B* (1965-1970) 51 (1967) 1–11. doi:10.1007/bf02712316.
- [200] N. J. Calos, E. Graham, D. R. Cousens, P. Christodoulou, C. H. L. Kennard, L. K. Bekessy, S. F. Parker, Mode of boron solubility in ferrous alloys, *Mater. Trans.* 42 (2001) 496–501. doi:10.2320/matertrans.42.496.
- [201] L. Reichel, L. Schultz, D. Pohl, S. Oswald, S. Fähler, M. Werwinski, A. Edström, E. K. Delczeg-Czirjak, J. Ruzs, From soft to hard magnetic Fe-Co-B by spontaneous strain: a combined first principles and thin film study, *J. Phys.-Condes. Matter* 27 (2015) 13. doi:10.1088/0953-8984/27/47/476002.
- [202] D. Gölden, H. Zhang, I. Radulov, I. Dirba, P. Komissinskiy, E. Hildebrandt, L. Alff, Evolution of anisotropy in bcc Fe distorted by interstitial boron, *Phys. Rev. B* 97 (2018) 014411. doi:10.1103/PhysRevB.97.014411.
- [203] M. Ohtake, T. Kawai, Y. Asai, M. Futamoto, N. Inaba, Influences of B/Fe Composition and Substrate Temperature on the Structure of Fe-B Alloy Film Formed on MgO(001) Substrate, *J. Magn. Soc. Jpn.* 39 (2015) 196–204. doi:10.3379/msjmag.1508R006.
- [204] D. J. Joyner, O. Johnson, D. M. Hercules, A study of the iron borides. 1. Electron spectroscopy, *J. Am. Chem. Soc.* 102 (1980) 1910–1917. doi:10.1021/ja00526a025.
- [205] M. Cadeville, A. J. P. Meyer, Points de Curie et moment des borures ferromagnétiques du groupe du fer de type M_2B , MB , $(M_1, M_2)_2B$ et $(M_1, M_2)B$, *C. R. Hebd. Seances Acad. Sci.* 255 (1962) 3391–3393.
- [206] T. Nakajima, E. Kita, H. Ino, Crystallization process and magnetic properties of $Fe_{100x}B_x$ ($10 \leq x \leq 35$) amorphous alloys and supersaturated state of boron in α -Fe, *J. Mater. Sci.* 23 (1988) 1279–1288. doi:10.1007/bf01154591.
- [207] L. Reichel, G. Giannopoulos, S. Kauffmann-Weiss, M. Hoffmann, D. Pohl, A. Edström, S. Oswald, D. Niarchos, J. Ruzs, L. Schultz, S. Fähler, Increased magnetocrystalline anisotropy in epitaxial Fe-Co-C thin films with spontaneous strain, *J. Appl. Phys.* 116 (2014) 213901. doi:10.1063/1.4901595.
- [208] D. Benea, O. Isnard, V. Pop, Electronic structure and magnetic properties of the $Fe_{16}N_2$ doped with Ti, *J. Magn. Magn. Mater.* 420 (2016) 75–80. doi:10.1016/j.jmmm.2016.06.083.
- [209] Y. Masubuchi, H. Sato, T. Motohashi, S. Kikkawa, Magnetic softening of Co doped α'' - $Fe_{16}N_2$ containing residual Fe-Co alloy prepared in low temperature nitridation, *J. Ceram. Soc. Jpn.* 122 (2014) 288–291. doi:10.2109/jcersj2.122.288.
- [210] M. Kopcewicz, J. Jagielski, G. Gawlik, A. Grabias, Role of alloying elements in the stability of nitrides in nitrogen-implanted α -Fe, *J. Appl. Phys.* 78 (1995) 1312–1321. doi:10.1063/1.360373.
- [211] I. Khan, J. Hong, Tuning magnetocrystalline anisotropy of α'' - $Fe_{16}N_2$ by interstitial impurity doping: A first principles study, *J. Magn. Magn. Mater.* 433 (2017) 17–23. doi:10.1016/j.jmmm.2017.02.041.

-
- [212] C. Feng, J. Yin, J. Niu, Q. Zhang, L. Gu, F. Yang, X. Tang, L. Xu, K. Gong, Y. Cao, M. Yang, X. Cui, S. Ogata, W. Geng, G. Yu, Construction of FeN alloy films with ultra-strong magnetism and tunable magnetic anisotropy for spintronic application, *J. Alloys Compd.* 725 (2017) 32–40. doi:10.1016/j.jallcom.2017.07.127.
- [213] N. Schwartz, E. D. Feit, Impurity Effects in the Nucleation of Alpha (bcc)Tantalum or BetaTantalum Films, *J. Electrochem. Soc.* 124 (1977) 123–131. doi:10.1149/1.2133224.
- [214] W. R. Morcom, W. L. Worrell, H. G. Sell, H. I. Kaplan, The preparation and characterization of beta-tungsten, a metastable tungsten phase, *Met. Trans.* 5 (1974) 155–161. doi:10.1007/BF02642939.
- [215] A. B. Papandrew, M. S. Lucas, R. Stevens, I. Halevy, B. Fultz, M. Y. Hu, P. Chow, R. E. Cohen, M. Somayazulu, Absence of Magnetism in Hcp Iron-Nickel at 11 K, *Phys. Rev. Lett* 97 (2006) 087202. doi:10.1103/PhysRevLett.97.087202.
- [216] A. Monza, A. Meffre, F. Baudelet, J. P. Rueff, M. dAstuto, P. Munsch, S. Huotari, S. Lachaize, B. Chaudret, A. Shukla, Iron Under Pressure: "Kohn Tweezers" and Remnant Magnetism, *Phys. Rev. Lett.* 106 (2011) 247201. doi:10.1103/PhysRevLett.106.247201.

Acknowledgements

First and foremost I would like to thank my supervisor, Prof. Dr. Lambert Alff, for believing in me and giving me the opportunity to perform research in his group. Especially (but not only) during the last months of this work, your tremendous support and guidance allowed me to go on and finally finish this thesis.

I am also very grateful to Dr. Erwin Hildebrandt, since without your continuous assistance, be it for technical, topical or simply general problems, I would not have been able to conclude this work and I will always look back fondly to our discussions. The ones accompanied with beer as well as the ones without!

I would like to thank Imants Dirba, my fellow iron nitrider, for all the discussions on the iron nitrides and the challenges we faced together. For me, the proverb 'a burden shared is a burden halved' was rarely as fitting as in our case.

Special thanks go to my friends and family for always encouraging me to go on and cheering me up when things were looking grim. I could not have done this without you!

Thanks go also to my fellow doctoral students, from ATFT or other groups, who were always there to discuss thoughts as well as ideas and give feedback. Special thanks go to Sharath Ulhas, Stefan Vogel, and Shalini Sharma, my fellow MBE users, for sharing the burden of keeping our unit up and (mostly) running. Special gratitude also goes to Tim Helbig, Simon Sawatzki, Thorsten Gröb and Sandra Schäfer for the great time I had during all of our meetings and seminars in RESPONSE.

I would also like to thank Prof. Dr. Donner, Prof. Dr. Ensinger, my colleagues from ATFT (former as well as present), the group of functional materials, and our skilled technicians in the workshop of the materials science institute for all the help and support you have given me.

Last but not least, I thank the German federal state of Hessen through its excellence program LOEWE RESPONSE for financial support which funded my research.

Curriculum vitae

Dominik Gölden, born on 20th of September 1984 in Viersen, Germany.

School education:

1990 – 1991 Primary school, Ecole publique mixte de Roquefort-les-Pins, France

1991 – 1994 Primary school, Katholische Grundschule Mönchengladbach Venn, Germany

1994 – 2003 Secondary school, Bischöfliche Marienschule Mönchengladbach, Germany, general qualification for university entrance

University education:

04/2004 – 09/2008 Rheinisch-Westfälisch Technische Hochschule Aachen, Germany
-Physics

10/2008 – 08/2011 Bachelor of Engineering, FH Aachen University of Applied Sciences, campus Jülich, Germany
-Physical Engineering

10/2011 – 09/2013 Master of Science, RheinMain University of Applied Sciences, campus Rüsselsheim, Germany
-Applied physics

01/2014 – 12/2017 Doctoral Studies, Technische Universität Darmstadt, Institute of Materials Science, Advanced Thin Film Technology, Darmstadt, Germany
-Supervisor: Prof. Dr. Lambert Alff
-Thesis: Magnetocrystalline anisotropy of iron thin films with interstitial nitrogen and boron

A BN low-flow aperture and discharge tube designs

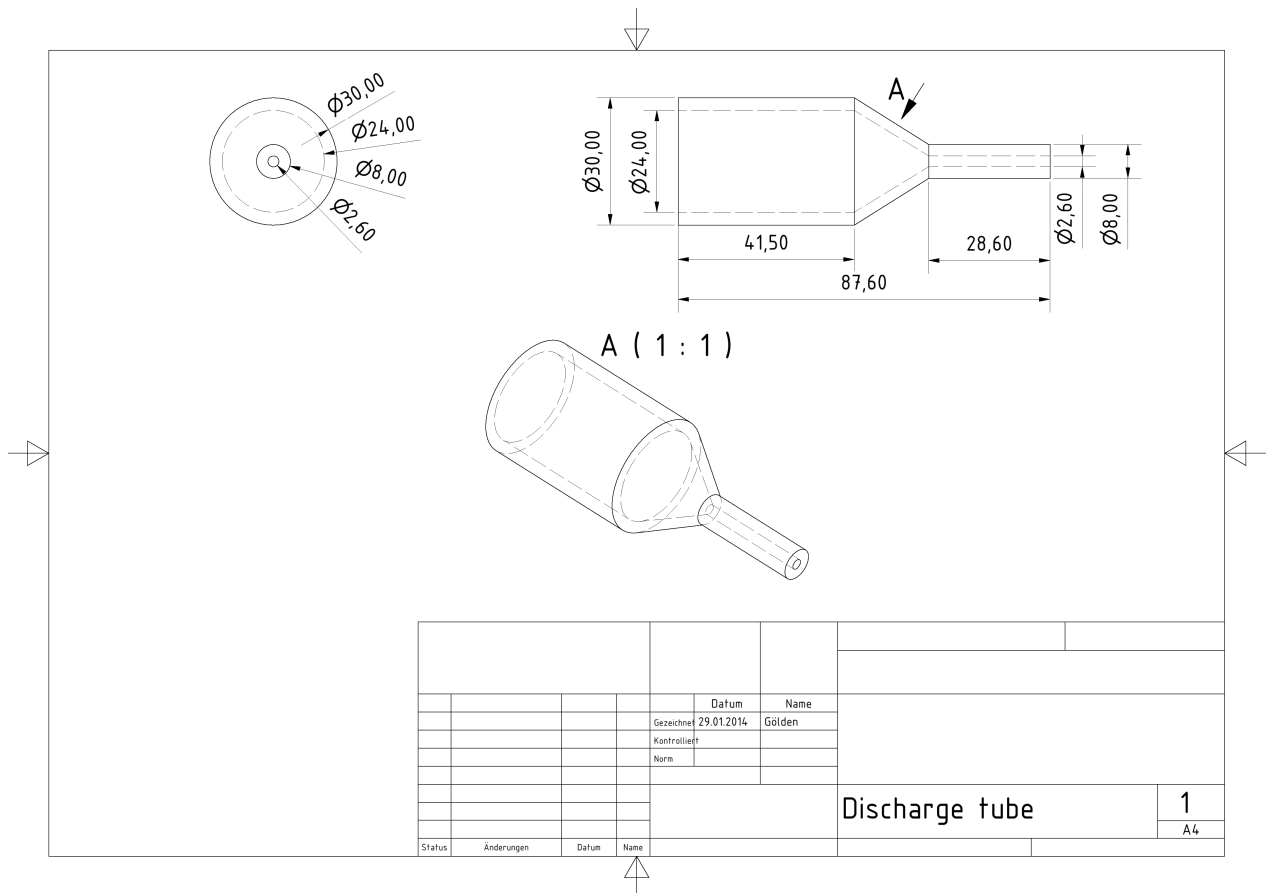
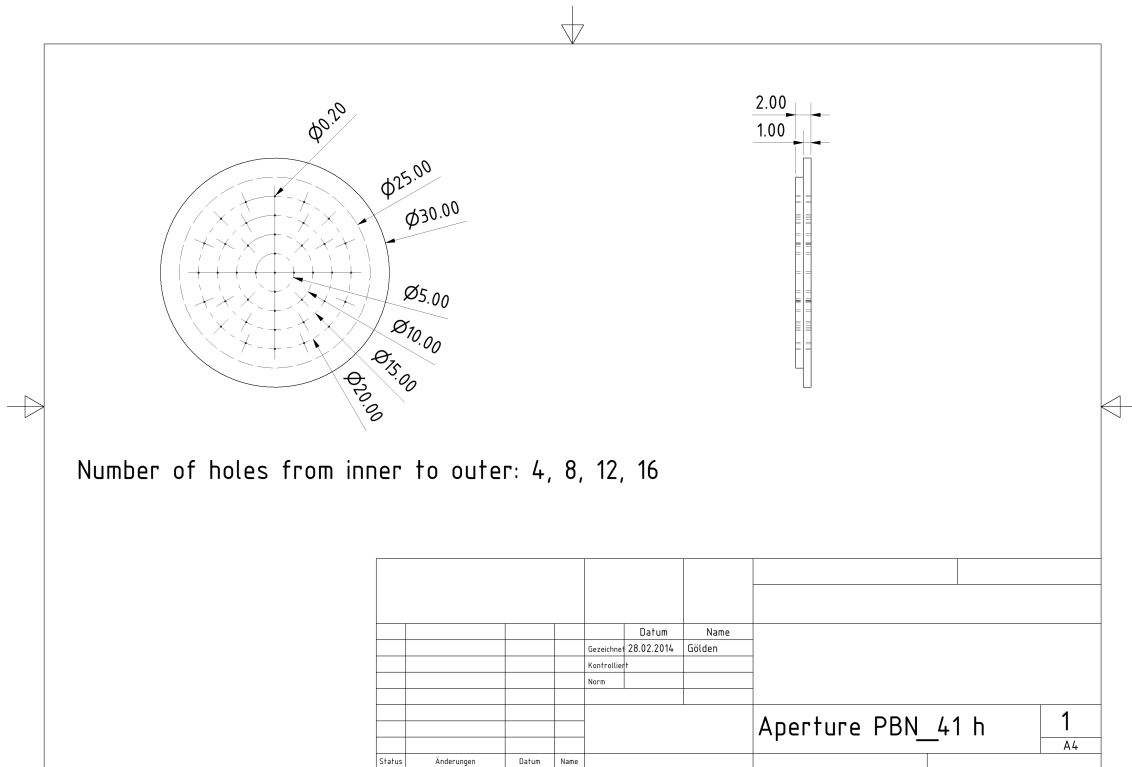
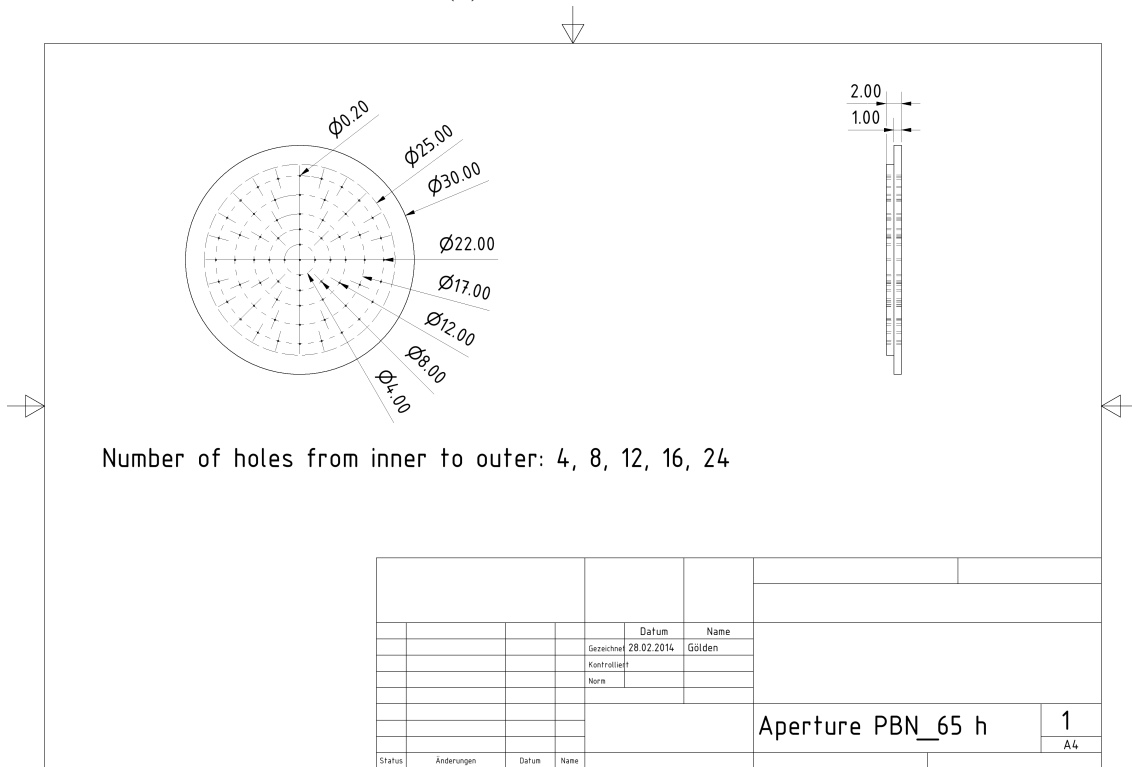


Figure A.1: Construction design of BN discharge tube.



(a) 41 holes aperture.



(b) 65 holes aperture.

Figure A.2: Construction design of BN aperture with (a) 41 and (b) 65 holes of 0.2 mm.

B Formation of (002) and (011) oriented α -Fe

During the growth of iron nitride samples, an additional RHEED pattern (see Fig. B.5(a)) was observed without secondary XRD reflexes present (see section 6.1). During a series of samples which were grown without using the radical source, an additional XRD reflex at the position of α -Fe (011) was observed, displayed in Fig. B.6. The iron growth rate was set to 0.04 \AA/s at a substrate temperature of 373 K and a molecular nitrogen flow which was varied from 0.045 to 0.075 sccm . The resulting RHEED pattern was identical to the previously observed and is shown exemplary for three samples in Fig. B.5(b) to (d).

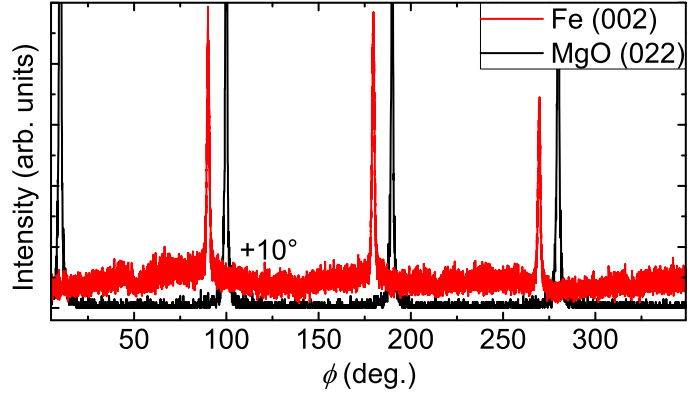


Figure B.3: ϕ -scan of α -Fe(200) with respect to MgO(022).

Interestingly, the α -Fe (011) reflex appears for low additions of both, nitrogen and boron, with a tendency to vanish for higher concentrations, mirrored by the different peak intensities plotted as a function of the nitrogen flow in Fig. B.4. This effect, so far unreported in literature, seems to be similar of nature to the formation of β -Ta and β -W which can be promoted by small amounts of nitrogen or oxygen impurities [213, 214]. However, SQUID measurements revealed a saturation magnetization of around 1580 kA/m (1580 emu/cm^3), close to that of α -Fe, the formation of allotropes

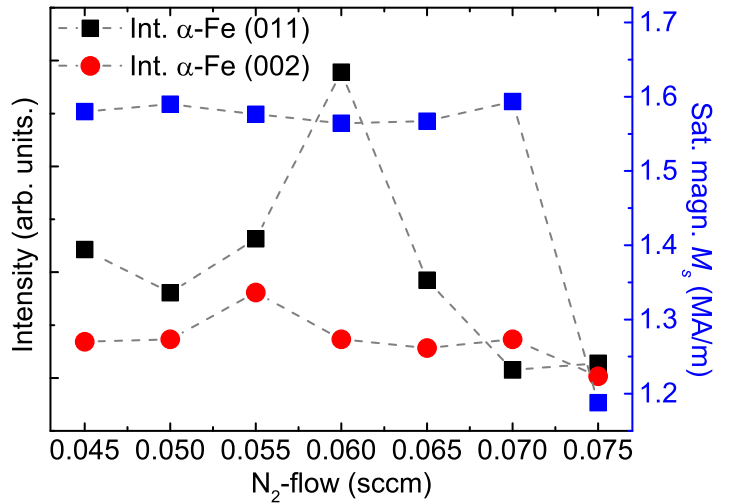
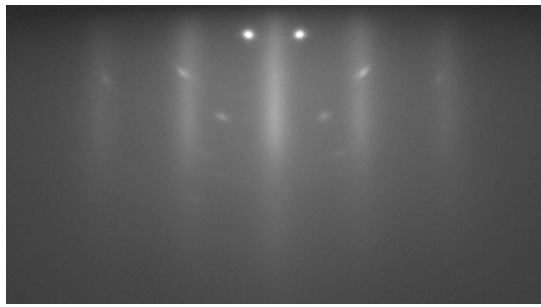
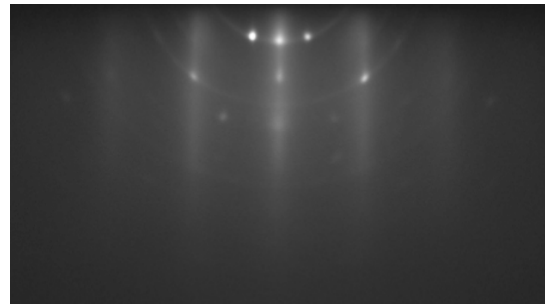


Figure B.4: Intensity of the (011) and (002) reflex as well as M_s plotted against the nitrogen flow, extracted from the measurements shown in Fig. B.6.

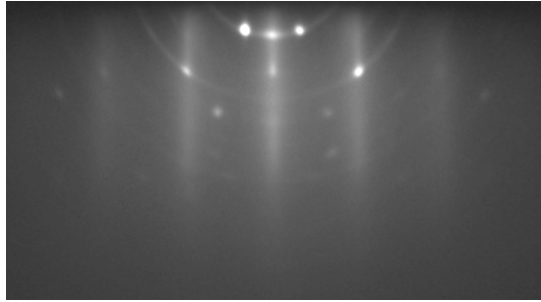
of iron like the paramagnetic γ -Fe and the antiferromagnetic ϵ -Fe can be excluded [215, 216]. A ϕ -scan at the expected reflection of (200) oriented α -Fe (Fig. B.3) revealed a fourfold symmetry, thus further supporting the assumption that low concentrations of small impurities like N or B result in a crystal growth with α -Fe(011) || MgO(001) and α -Fe[002] || MgO[100], a rotation of 45° in- and out-of-plane compared to the expected growth orientation of α -Fe on MgO (100) substrates.



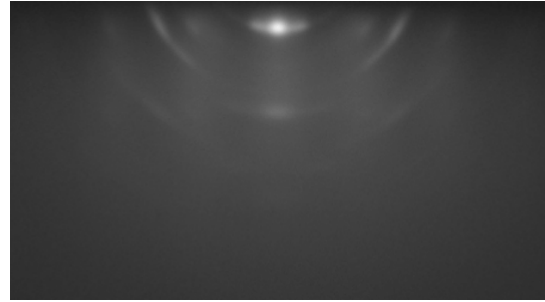
(a) Final RHEED pattern with 0.1 \AA/s and 145 W .



(b) Final RHEED pattern with 0.055 sccm .



(c) Final RHEED pattern with 0.06 sccm .



(d) Final RHEED pattern with 0.075 sccm .

Figure B.5: RHEED pattern of (a) an α' - Fe_8N sample and (b)-(d) samples grown with 0.04 \AA/s and varying nitrogen flows; both recorded with the electron beam parallel to the (100) orientation of MgO.

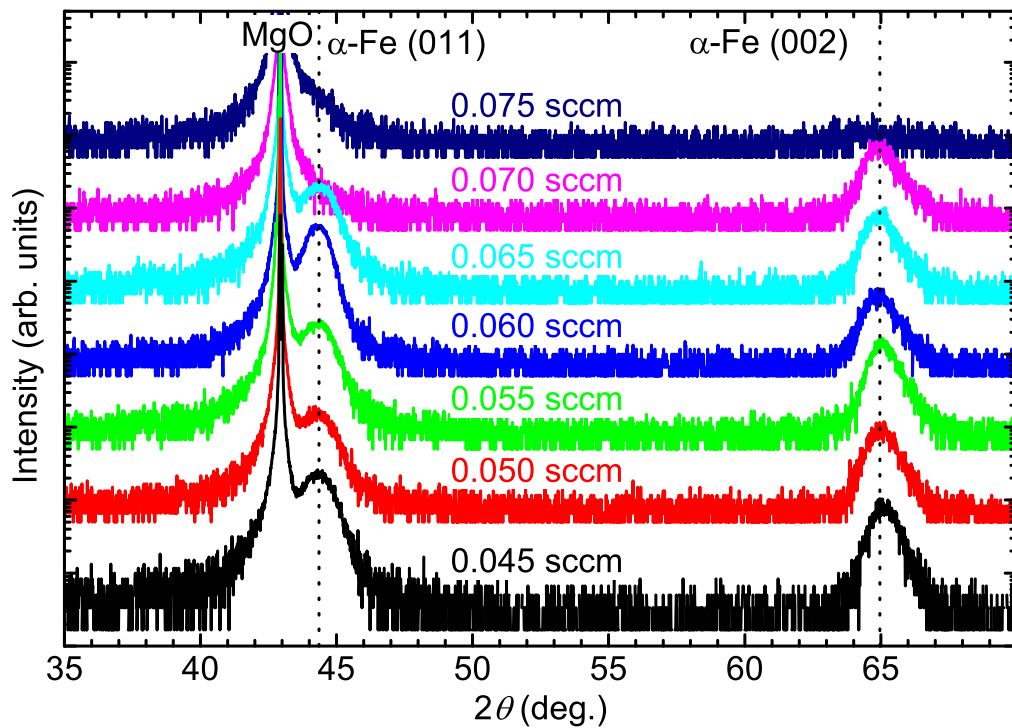
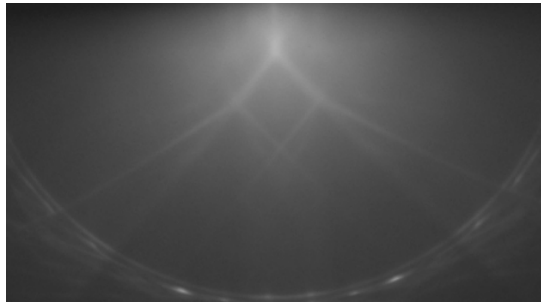
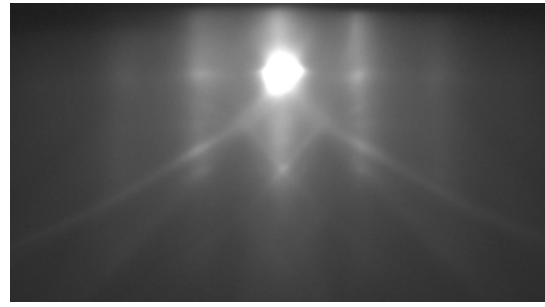


Figure B.6: XRD measurements of thin films grown at increasing nitrogen flow without using a plasma at 373 K and a growth rate of 0.04 \AA/s .

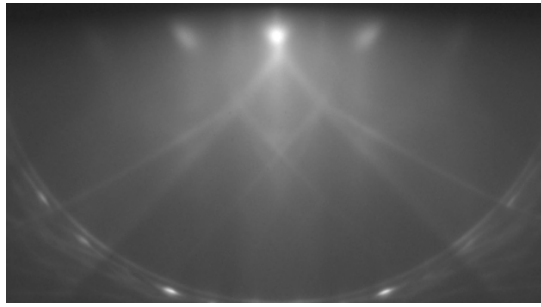
An important point of this work was to establish a procedure allowing the reproducible synthesis of samples with comparable properties when using identical growth parameters. The general procedure utilized for MBE grown samples is summarized in a flowchart (Fig. C.8(a)). Before starting the deposition, the substrates were subjected to a heat treatment of 973 K for 30 minutes in vacuum. This step was found to be necessary to remove the majority of adsorbates from the surface, thereby achieving a clean and atomically flat substrate surface as can be seen from the clear and sharp streaks in the RHEED pictures of bare MgO and MAO substrates before, during, and after the heat treatment displayed in Fig. C.7(a) to C.7(f). This resulted in an overall improved crystal quality of the samples, particularly for the first monolayers. The main challenge however, was found to be a stable (i.e. not strongly drifting) temperature for the growth of α' -Fe₈N, which, as reported in literature (see section 4.3) and experimentally demonstrated (section 6.1), is susceptible to different growth temperatures and, as shown in section 6.4, has a lower decomposition temperature than generally assumed. Letting the temperature stabilize for approximately 30 minutes resulted in suitably stable conditions. However, once the sample shutter was opened, the operated sources introduced a thermal drift, an issue that could not be avoided or even minimized during this work. A possible solution to this challenge could be the utilization of a heatsink, ideally actively cooled, connected to the sample stage. Prior to the last step of sample synthesis, the deposition of a capping layer, the sample was given time to cool down below approximately 353 K.



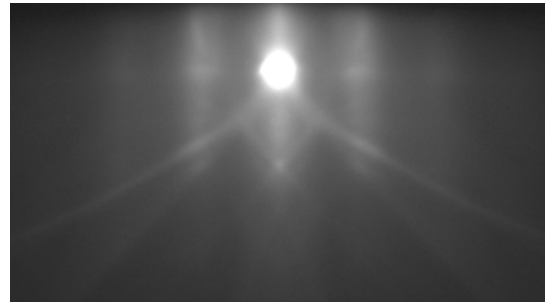
(a) MAO RHEED without annealing.



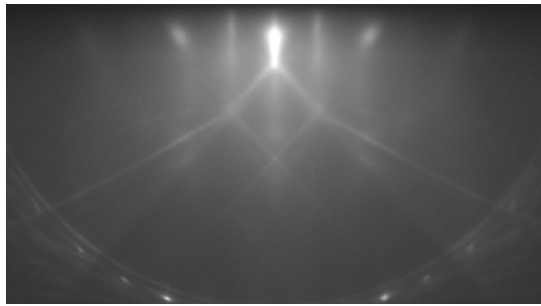
(b) MgO RHEED without annealing.



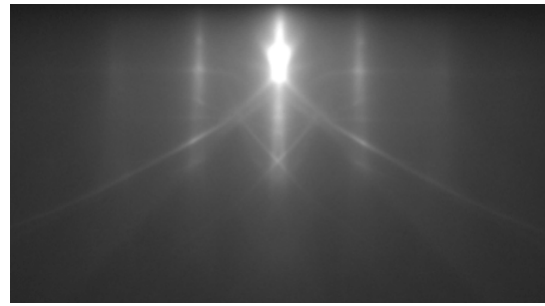
(c) MAO RHEED pattern after 5 minutes anneal.



(d) MgO RHEED pattern after 5 minutes anneal.



(e) MAO RHEED pattern after 30 minutes anneal.



(f) MgO RHEED pattern after 30 minutes anneal.

Figure C.7: RHEED patterns of bare MAO and MgO substrates along their (100) direction without, after 5, and after 30 minutes of annealing at 973 K in vacuum prior to deposition.

Although the process for sputtered samples was essentially identical to the MBE growth described earlier, a poor reproducibility was observed. Particularly for samples that were grown after an idle period of 8 hours or longer, no XRD peaks could be found and the films exhibited a high roughness as well as poor density. However, when the same conditions were used to consecutively synthesize further samples directly after this first deposition, the resulting films were of good crystal quality with smooth surfaces. This effect was found to be most likely caused by the sample manipulator that, when subjected to the plasma during the initial sample, would outgas and therefore cause a high local partial pressure of contaminants. To circumvent this issue, a pre-sputtering process was established prior to the deposition. Initially, a blank sample holder was mounted on the manipulator to protect the heater from being coated. Then, the desired source was started to expose the manipulator to the plasma and coat it for approximately 15 to 20 minutes after which the chamber was pumped down again. Subsequently, the holder was removed and pasted with a substrate in order to carry out the deposition. This process, summarized by Fig. C.8(b), resulted in an overall good reproducibility.

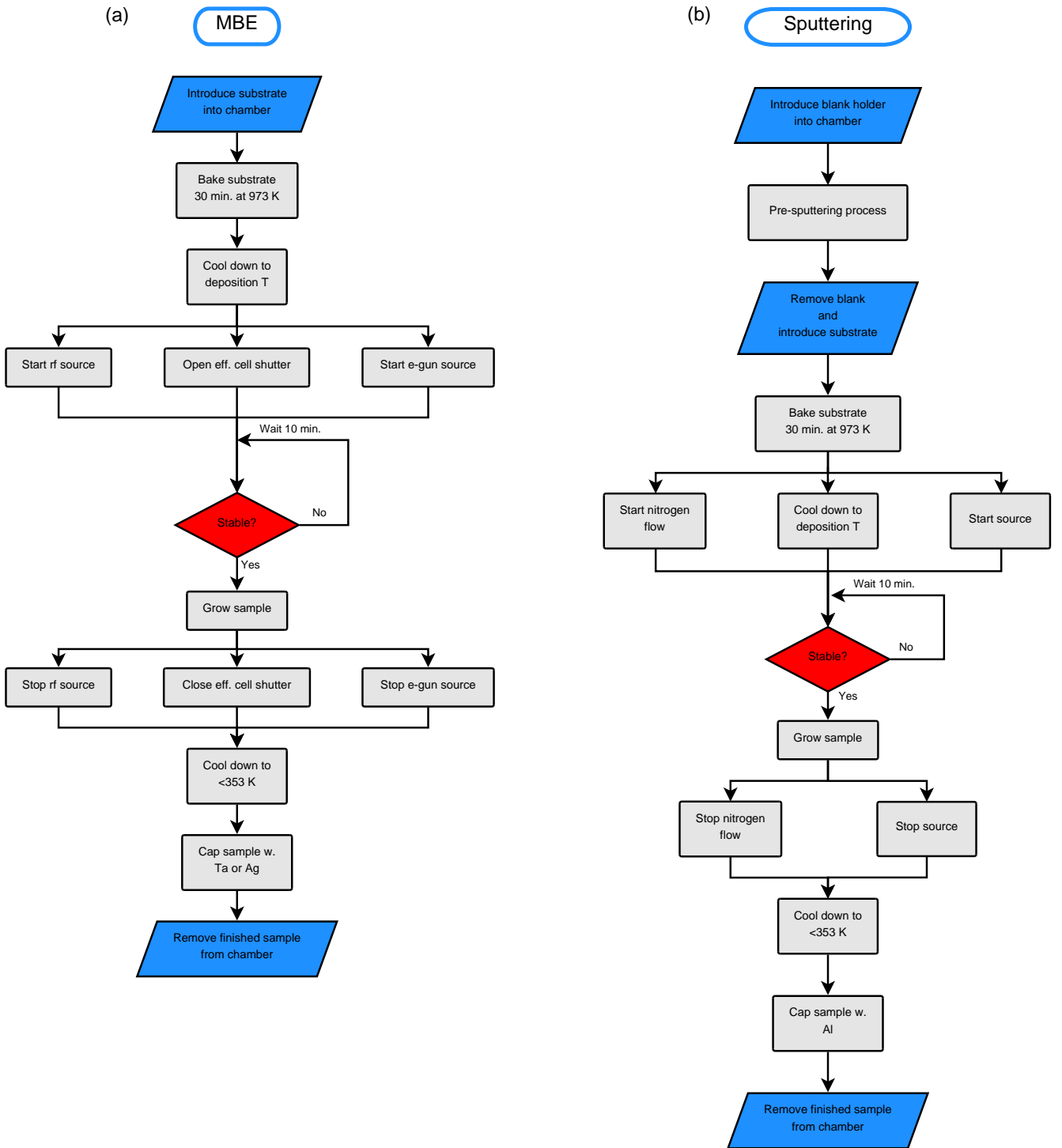


Figure C.8: Flowcharts for samples grown by (a) MBE and (b) sputtering.